Design, construction and commissioning of an automated optical fibre catalyst coating process for use in photocatalytic reactor systems

Prepared by:

Naomi Harrisankar

BSc Chemical Engineering, University of Cape Town, South Africa

Thesis presented to the University of Cape Town

in fulfilment of the requirements

for the degree of

Master of Science in Chemical Engineering

Department of Chemical Engineering

Faculty of Engineering and the Built Environment

University of Cape Town

South Africa

Declaration

I understand the definition of plagiarism and I declare that all the work in this dissertation, save for those which has been properly acknowledge, is my own. This thesis has been submitted to an originality checking software and I can confirm that my supervisors have seen and approved my dissertation for submission.

Signature: Signed by candidate

Acknowledgements

This dissertation is a result of the accumulation of work that I could not have completed without the help and support from countless different people. First and foremost, I would like to thank my Lord and saviour, Jesus Christ, for his love and unmerited favour in my life, for without him I would not have what I do, and be who I am.

I would like to thank the National Research Foundation for funding my research. I would also like to thank my supervisors, Professor Eric van Steen and Associate Professor Pieter Levecque for their constant support and guidance as mentors and supervisors. I would especially like to thank Prof Eric van Steen for firstly , giving me this amazing opportunity and for allowing me to have freedom in my research and for understanding the type of engineer that I am and want to be. His open-door policy, encouragement, and belief in me was a key reason that I achieved everything I did.

I would like to thank the technical staff in the Catalysis institute and electronic workshop at the Department of Chemical Engineering ,UCT, for always being available and happy to help even when my requests seemed unusual and, especially, for giving me the best lab-space ever.

A special thanks to several colleagues who have assisted me throughout my project. Mr. Joachim Macke, who not only provided timely mechanical assistance but also believed in me and supported all my ideas. Future Dr. Sampath Jalayath, for always being one call away whenever I needed any kind of assistance and for giving me many hours of his own time . Dr. Nasibe Nosrati Ghods for joining my one-woman photocatalysis team. I would also like to thank Miranda Waldron for being so kind and patient with me and for the many hours she spent helping and teaching me.

I would not have made it through the two years of masters without the support from all of my friends. Thank you all for always being available whenever I needed both academic and personal support. A special thank you to Nasseela Hytoolakhan Lal Mahomed , Ruane Govender and Jonathan Gertzen whose contributions were vital throughout my masters.

Last but not least , I want to thank God for giving me parents who have loved me and supported me throughout my academic career. I would like to thank my parents for the sacrifices they made so that I could have this privilege. I would like to thank my mom for always praying for me even though she had and still has no clue what I do on campus. I would like to thank my dad for being my engineering role model and for his significant technical contributions to my project.

Synopsis

Climate change is one of the greatest challenges facing humanity. Fossil fuels are the primary source of energy on Earth. Since the global economic growth is closely linked to the global energy demand, fossil fuel usage remains the largest contributor to the steadily increasing atmospheric carbon dioxide concentration (CO_2). CO_2 mitigation through carbon capture and conversion are of great interest. Capturing CO_2 from point source emitters is possible by absorption in a basic, sodium hydroxide (NaOH) containing solution, which is then converted into sodium bicarbonate ($NaHCO_3$). Conversion of CO_2 is thermodynamically demanding as it will require a large amount of energy, which renders currently used technologies infeasible. A promising alternative is the conversion of captured $NaHCO_3$ into useful hydrocarbons at moderate operating conditions using solar energy, by a process called photocatalysis. Photocatalysis is the acceleration of a photo-induced reaction in the presence of a catalyst.

Photocatalytic reactors have not yet been commercialised due to suboptimal catalyst and reactor designs. The typically low catalyst activity has to be countered by efficiently loading a large amount of catalyst in the reactor. This results in a problem regarding the photon transfer limitations to the catalytically active site, which limits illumination of the catalyst in the reactor. This can be overcome by using optical fibre to guide photons, which are coated with the photocatalyst. However, it is estimated that a reactor containing ca. 1 g of catalyst will require ca. 1.8 km of identically coated optical fibre.

The aim of the project is to design, construct and commission an automated controllable process to increase the production volume of catalyst coated optical fibre using either a sol-gel suspension or a slurry containing P25 (TiO_2). A multi-step optical fibre coating process was developed to achieve the desired coated optical fibre as a product. It consists of 6 major units that process raw (polymer-coated) optical fibre into catalyst coated optical fibre. The steps include the 4 essential steps required for optical fibre preparation by-hand, these steps are stripping, washing, coating and heat treatment.

This automated optical fibre catalyst coating process (AOFCCP) can make the coating of optical fibres time-efficient and controllable. The latter can be achieved by controlling the effect various process parameters affecting the coating thickness and homogeneity of the coating, such as pH, heat treatment, catalyst slurry concentration as well as pulling speed.

The AOFCCP produced coating thicknesses ranging from 0.47 µm - 0.59 µm and 0.37 µm - 0.46 µm for the P25 slurry and sol-gel coating methods respectively. The pH of the P25 slurry was found to have a negligible effect on both the coating thickness and surface morphology, therefore is no longer regarded as a process variable in the AOFCCP. The thickness of the

coating increased with an increase in P25 slurry concentration with a maximum achievable coating thickness of 0.87 µm using a slurry concentration of 20 wt.-%. The temperature of heat treatment which was tested showed different relationships between the coating methods. For the sol-gel coating method, the increase in temperature resulted in a decrease in coating thickness possibly due to the decrease in porosity whereas for the P25 slurry method the increase in temperature showed an increase in coating thickness possibly due to the higher evaporation rates. An increase in the pulling speed in the AOFCCP resulted in an increase in coating thickness on the optical fibre independent of the coating method; coating thicknesses ranging from 0.41 µm - 0.71 µm and 0.23 µm - 2.14 µm were obtained using the P25 slurry and sol-gel coating methods, respectively, by varying the pulling speed.

The critical cracking thickness is defined as the thickness of the film, produced by the sol-gel method, at which coating deformations become observable which was found to be 0.37 µm at 600 °C, and 0.77 µm at a pulling speed of 2.30 $mm \cdot s^{-1}$.

The results obtained from the commissioning experiments showed that the AOFCCP can produce coated optical fibre with controllable thickness. The controllability was discovered to be in the adjustment of the process variables investigated which showed a significant effect on the coating thickness, except for pH. Based on the statistical analysis that was performed, it was confirmed that the results obtained from the system were repeatable and that the coating was uniform for all process variables that were investigated except for sol-gel coating at high speeds of 2.88 $mm \cdot s^{-1}$ – 3.46 $mm \cdot s^{-1}$. The system was able to produce fibre with coating thickness's between 0.4 – 1.1 µm.

It is recommended that a combination of the process variables be used in order to achieve better controllability in the process and to achieve thicker coating layers. Furthermore, the operating ranges of the process variables should be increased in order to determine the extent of the relationship between the process variable and the coating thickness and surface morphology.

Table of Contents

List of Figures

List of Tables

1. Introduction

To date, fossil fuels are being used as the primary source of energy on Earth. As the global economy grows, the consumption of fossil fuels has been observed to increase, resulting in the steady increase of the atmospheric concentration of carbon dioxide, CO_2 [1]. An increase in the concentration of CO_2 accelerates of the warming of the earth's atmosphere since it is a greenhouse gas. Therefore, it is important to establish a sustainable, resource-efficient and low carbon economy. For this reason, a great amount of research has been put into CO_2 mitigation via either zero CO_2 emission processes or capture and conversion of CO_2. The capture of CO_2 is possible by contacting the CO_2-containing gas with a sodium hydroxide (NaOH) solution resulting in the formation of sodium bicarbonate. This technology can be applied to point sources which are emitters which produce large quantities of CO_2 such as the steel manufacturing or petrochemical industries. Sodium bicarbonate can then be converted photocatalytically into carbon monoxide or organic product compounds such as methane, methanol, formic acid and formaldehyde.

Photocatalysis is the acceleration of a photo-induced reaction in the presence of a catalyst, typically a semiconductor [1]. TiO_2 is most commonly used as a photocatalyst since it is inexpensive, photo corrosion-resistant, non-toxic and has exceptional optical and electronic properties [2]. However, TiO_2 has a large bandgap energy which allows it to be activated only by light in the UV range, which comprised only ca. by 5% of the solar spectrum. The use of photocatalysis as a method to reduce CO_2 thus require efficient usage of the available solar radiation.

One of the most common photoreactors that is studied is the slurry reactor. However, these photoreactors are rarely operational in industry due to their low productivity and sub-optimal photoreactor design. One major development in photoreactor design is the introduction of optical fibres to improve illumination efficiency and uniformity. The optical fibre is used to guide the light to the catalyst, e.g. by having an optical fibre coated with a photocatalyst. The thickness of the coating is here a key factor as it determines the amount of light that is refracted and scattered [2].

This coating of an optical fibre typically comprises of 4 steps, namely, cladding stripping, bare-fibre washing, dip-coating of catalyst onto the optical fibre and lastly heat treatment of coated optical fibre. This process is typically performed manually, which has been sufficient to date since optical fibre photoreactors typically used up to 50 - 200 coated optical fibres. However, this results in very low catalyst loading, inefficient use of reactor volume as well as a low surface to volume ratio. A reactor packed with coated optical fibre would utilize the reactor

volume more efficiently by increasing the catalyst mass and surface area and thus, the catalytically active sites to achieve the photocatalytic reduction of CO_2 [3]. Furthermore, this may result in an improved contact pattern of the fluid containing CO_2 with the photocatalyst.

However, for a catalyst loading of 1 g and a coating thickness of 0.7 μm, the required length of the optical fibre, which needs to be coated, is 1.8 km. Since coating these quantities by hand will require excessive time and manpower, it is necessary to develop an automated system which can combine the 4 processes of fibre preparation to reduce the manpower and time required. The system should be designed to produce controllable catalyst coating thicknesses on the optical fibre. The process should be repeatable. This is done by investigating various process variables, such as temperature, pulling speed, pH and concentration, which is believed to have a direct effect on the coating thickness [1- 5].

2. Literature review

2.1. The energy crisis and climate change

At present, climate change is one of the greatest challenges facing humanity. To date, fossil fuels such as coal, oil and gas are the primary sources of energy on Earth. These carbon-rich fuel resources remain the largest contributors to the steadily increasing atmospheric carbon dioxide (CO_2) concentrations (see Figure 2-1) [7, 8]. Global economic growth will result in an increase in the global energy demand and consequently an accelerated consumption of fossil fuels from limited reserves [9]. Increasing atmospheric greenhouse gas (GHG) levels alter the Earth's energy balance resulting in an overall warming effect of the Earth. This has a major impact on the weather patterns, global mean sea levels, biodiversity as well as anthropological health and society for both the present and future generations [10].

Greenhouse gas emissions in the year 2017 were 55% higher than that in 1990 and 40% higher than in 2000 demonstrating the rapid increase with time. Carbon dioxide is a major contributor to the total GHG emissions in 2017 and held 73% share. According to the UN Climate change report in 2017, the atmospheric carbon dioxide levels are at the highest level it has ever been [9]. Therefore, it is important for humanity to switch to a more sustainable, resource-efficient and low carbon economy [11]. This will ease concerns related to energy security, cost of energy as well as issues of sustainability [12]. To achieve this, a great amount of research has been put into mitigating CO_2 emissions, e.g. by CO_2 capture and conversion or by completely avoiding the formation of CO_2. An ideal solution would be the efficient utilization of carbon sources.

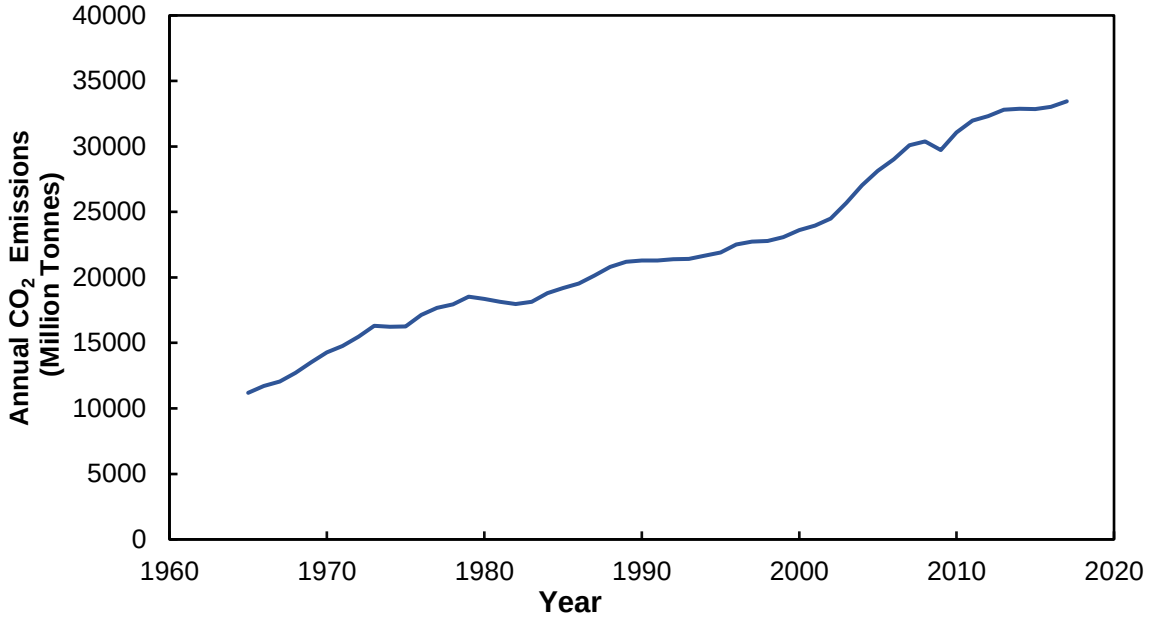

Figure 2-1: Annual carbon dioxide emissions (reproduced from [2])

Since the conversion of CO_2, by chemical methods, require an extensive amount of thermal energy, methods such as electro-catalysis, bio-catalysis and photocatalysis have been extensively researched in recent years [13]. Even though both electro-catalysis and bio-catalysis routes seem promising, issues such as process complexity, high energy requirements and cost inputs need to be overcome [13]. The photocatalytic conversion of CO_2 into useful hydrocarbons can be achieved using solar energy. This is a promising alternative since the Sun is the ultimate source of energy, making solar energy abundant. Moreover, it may be used at ambient conditions and without any further emission of CO_2 [7, 14]. It is possible to capture CO_2 (e.g. by absorption in a NaOH solution resulting in the formation of $NaHCO_3$). In particular, capture from large point sources may be economically feasible. However, there is much work needed to improve the productivity achieved by photocatalytic systems.

2.2. Overview of photocatalysis

Photocatalysis is the acceleration of a photo-induced reaction by the presence of a catalyst, which can be used to convert CO_2 in a similar way that photosynthesis occurs in plants [15, 16]. It is possible to reduce CO_2 by photocatalysis into compounds such as CO, CH_4, CH_3OH, formaldehyde as well as formic acid [14]. For CO_2 reduction, heterogeneous photocatalysis is considered, because of the ease of separation of the catalyst from the product stream (in contrast to homogenous catalysis, whereby the catalyst is dissolved in the reaction medium) [16].

Various semiconductor materials have been investigated as heterogeneous photocatalysts. A semiconductor is characterised by an electronic band structure [17] which consists of two bands, the highest occupied band called the valance band (VB) and the lowest empty band called the conduction band (CB). These bands are separated by a bandgap. Hence, a photon can be absorbed by the semiconductor, if it has an energy which is equal to or higher than the bandgap of the semiconductor (see Figure 2-2). Figure 2-3 illustrate the pathways that describe the processes that occur within a photocatalyst. The absorption process causes an electron (e^-) to move from the valance band to the conduction band, simultaneously creating a highly oxidising quasi-particle, commonly referred to as a hole (h^+) in the valance band (pathway 1). The electron-hole pair represents an activated state in photocatalysis, which is responsible for initiating the reaction [2, 16, 17]. The bandgap dictates the portion of the electromagnetic spectrum that the photocatalyst can absorb [11, 18] and is thus an important parameter in the choice of the semiconductor as a photocatalyst.

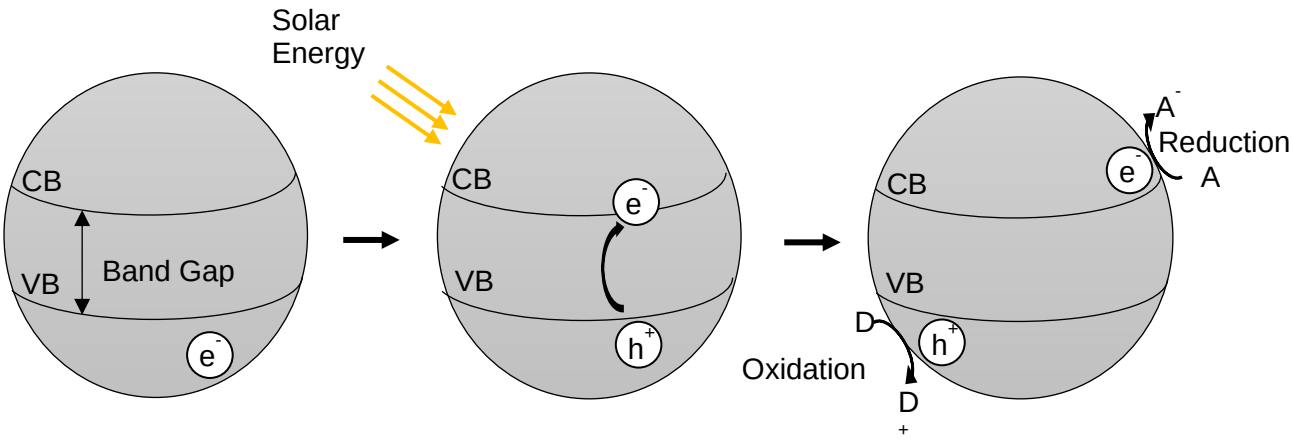

Figure 2-2: Activation process of a semiconductor photocatalyst

Figure 2-3 illustrates the processes which may occur within a photocatalyst once it has been activated by photons according to Pathway 1. The electrons may migrate to the surface of the catalyst where it may be used in reduction reactions with an acceptor (A) (pathway 2). The hole which is left behind may be used in oxidation reactions with a donor (D) (pathway 3). This is the mechanism by which the desired redox photoreaction can be induced. The electrons may also fall-back to the valance band and recombine with the hole, dissipating the absorbed energy as heat. This process is called electron-hole recombination and may occur either on the surface of the catalyst (pathway 4) or in the bulk of the catalyst (pathway 5). The latter is referred to as volume recombination [19]. The efficiency of the photocatalytic reaction is thus highly dependent on the rate of recombination in the semiconductor. Factors such as mobility and charge trapping, are being investigated in order to reduce recombination rates [19 – 21].

The energy level at the bottom of the conduction band is the reduction potential of photo-electrons and the energy level at the top of the valance band determines the oxidizing potential of the photo-holes [2]. These promote redox reactions. Flat-band energy is described as the fixed energy difference between the two charge carriers and is determined by the nature of the material. Thermodynamically, if adsorbed species have a redox potential which is more positive than that of the flat-band potential, then they can be reduced by the electrons in the conduction band [11, 18]. Similarly, if the species have a redox potential which is more negative than the flat-band, then it can be oxidised by the valance band holes [2].

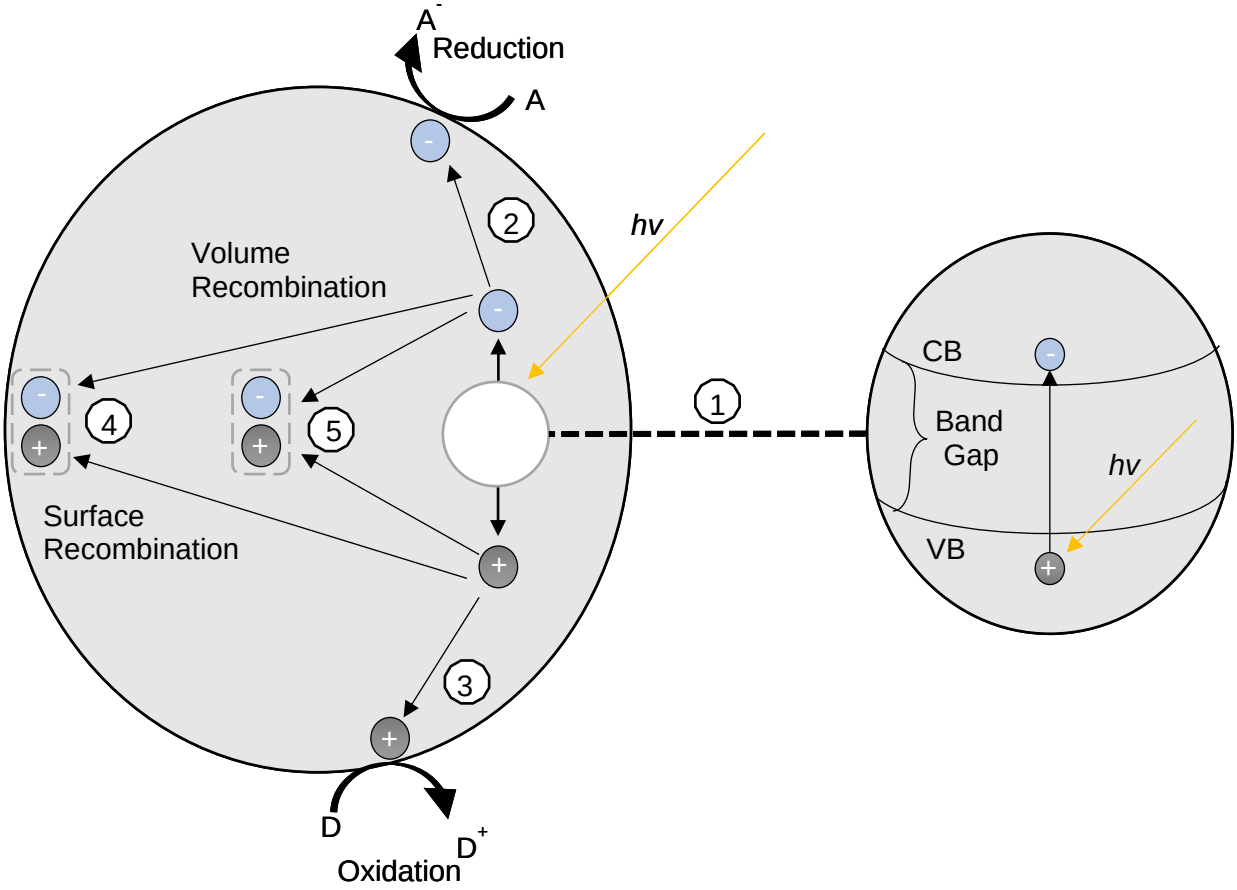

Figure 2-3: Processes occurring in a photocatalyst

2.3. Photocatalytic materials

For efficient utilization of solar energy, it is required that the semiconductor have a small bandgap as this allows it to be activated by part of the visible spectrum. Typical semiconductors that have been employed in photocatalysis are e.g. titanium dioxide (TiO_2), zinc oxide (ZnO), tungsten trioxide WO_3, tin oxide (SnO_2), ferric oxide (Fe_2O_3) and cadmium sulfide (CdS). Tungsten trioxide is useful in the visible light range [17], however, it is not as catalytically active as TiO_2. Zinc oxide has been shown to be unstable in illuminated aqueous mediums, particularly at low pH values [2]. TiO_2, as a semiconductor photocatalyst, is very common and most widely researched due to its low cost, non-toxicity and exceptional optical and electronic properties [2, 22]. Furthermore, the band structure of TiO_2 allows for the simultaneous oxidation and reduction of water. TiO_2 has becomea benchmark catalyst in photocatalysis and has been used in the photocatalytic water splitting, dye bleaching, pollutant degradation, water cleaning and CO_2 reduction [19].

TiO_2 exists in four different crystallographic phases, i.e. anatase (tetragonal), rutile (tetragonal), brookite (orthorhombic) and akaogiite (monoclinic). However, only anatase and

rutile have been used as a photocatalyst. Anatase and rutile are characterised by chains of TiO_6 octahedra, where each is comprised of Ti^{4+} ions surrounded by six O^{2-} ions. The differences in the unit cell of these crystal structures result in slightly different bandgap energies for these semiconductors (anatase 3.23 eV and rutile 3.02 eV) [19]. Anatase has been reported to have a higher photocatalytic activity than rutile, displaying recombination rates which are up to ten times lower than that of rutile [19]. It has been reported that a mixture of these anatase and rutile displays enhanced photon efficiencies that cannot be seen in either one separately. It has been proposed that using a combination of these phases provides charge separation or trapping properties, which reduces recombination due to the offset of 0.2 eV in bandgap energy [19]. It is also reported that anatase has trap sites located 0.8 eV below the edge of the conduction band, which promotes charge separation from anatase to rutile [19]. For this reason, P25 which is commercially sold TiO_2 powder and contains 80% anatase and 20% rutile, is often used as a photocatalyst.

The large bandgap energy, as well as fast recombination rate in TiO_2, result in a reduction in the efficiency of titania as the catalyst. There are various modifications that have been investigated in order to improve the productivity of photocatalytic systems [14, 18, 23]. Surface modification of TiO_2 may result in a larger specific surface area as well as increasing the number of active surface sites, improving CO_2 adsorption. Bandgap energy reduction may allow TiO_2 to be activated by visible light, which makes up 45% of incident sunlight energy [1, 2, 7, 11, 18, 23]. For instance, the incorporation of metal (Nb) or non-metal (B) ions in the lattice structure of TiO_2 creates an additional band between the valence band and the conduction band, which is vacant. This will thus result in a reduced bandgap energy allowing the absorption of photons with lower energy, i.e. a larger part of the solar spectrum and thus possibly increasing the photocatalytic activity [11, 18, 24]. However, the incorporation of these elements within the structure may result in defects which may induce alternative reactivities. The addition of carbon-based nanomaterial to TiO_2 has been studied since it has high electron conductivity, large specific area and adjustable surface properties. Carbon loaded TiO_2 was reported to improve spatial separation of electron-holes and electron concentration on the TiO_2 surface but reduce the amount of light absorbed by the TiO_2 [10, 18, 11]. Another method to reduce the bandgap energy of TiO_2 is by heterojunction construction, which is done by constructing the semiconductor heterojunction with TiO_2 depending on the charge carrier separation; conventional type-II, p-n junction, direct Z-scheme and surface heterojunction. This method improves the spatial separation of the electron-hole pairs as well as the reduction and oxidation sites [24]. Moreover, the modification of TiO_2 by the addition of alkali sorbents enhances CO_2 adsorption since CO_2 is an acidic oxide molecule, however, it has been reported to decrease the light absorption of the photocatalyst [11, 24].

2.4. Photocatalytic reduction of HCO_3^-

Carbon dioxide can be captured from major point source emitters by absorption in a sodium hydroxide solution. This chemical absorption process will result in the formation of bicarbonate form as shown in Equation (1)

$$NaOH(aq) + CO_2(g) \rightarrow NaHCO_3(aq) \quad (1)$$

, which can be converted in a photocatalytic process.

The mechanism for the photocatalytic reduction of CO_2 is complex and is not yet fully understood [25]. The reaction mechanism shown below has been adapted from Yuan and Xu [23], which provides the CO_2 to methanol electrochemical reaction occurring at a potential of - 0.38 eV. This is a multi-step process involving the adsorption of HCO_3^- onto the surface of the TiO_2 catalyst. This is followed by the activation of the TiO_2 photocatalyst and the transfer of photo-generated electrons and holes as shown by Equation (2). The holes produced are used to oxidise the water present in the reactor yielding oxygen and protons (see Equation (3)). The electrons are used to reduce of HCO_3^- to methanol (see Equation (4)). The overall reaction is shown by Equation (5). In order to produce one mole of methanol, seven photons are required. Therefore, it is imperative for the photocatalyst to have enough illumination to be activated and create the electron-hole pairs required to initiate the reaction. For this reason, photoreactor design development should promote close contact catalyst-light pathways to prevent light loss or delayed activation.

$$n - TiO_2 + 7hv \rightarrow 7\, e_{cb}^- + 7\, h_{vb}^+ \quad (2)$$

$$\frac{7}{2}H_2O + 7h_{vb}^+ \rightarrow \frac{7}{4}O_2 + 7H^+ \quad (3)$$

$$HCO_3^- + 7H^+ + 7\, e_{cb}^- \rightarrow CH_3OH + 2H_2O \quad (4)$$

$$HCO_3^- + \frac{3}{2}H_2O + 7hv \rightarrow CH_3OH + \frac{7}{4}O_2 \quad (5)$$

It should be noted that the proposed reaction pathway is only one of many since it has not yet been established. There is potential for branching pathways which may result in different products at the same time. This has initiated research into controlling selectivity by investigating factors such as CO_2 activation, adsorption reactants and desorption of products [23 – 26].

2.5. Photocatalytic reactor systems

Photocatalysis is a relatively new field which has gained increased interest in recent years. Photocatalytic reactors are very rarely operational in industry. Since the increase in research

into lab-scale photoreactor designs, there have been many discrepancies with regards to the measuring and reporting of the results obtained from these reactors, which ultimately inhibit the progress of research into photocatalysis [27 – 29]. The ultimate aim of this project is to utilise solar energy for the conversion of CO_2 and thus no electrical power would be required.

2.5.1. Photo-reactor design

Industrial implementation of photoreactors is limited due to problems in scaling up of the reactors, as well as the suboptimal designs that exist due to the lack of research [29]. According to van Gerven *et al.* [16], photoreactor systems have only recorded reactivities for the conversion of CO_2 to methanol between 0.05 – 0.1 mol/m^3·s, which is extremely low making these reactors not feasible for commercialisation. There are currently two key issues regarding photocatalytic reactor designs in terms of engineering limitations that need to be addressed in order for these reactors to be integrated into the industry, i.e. mass transfer limitations and photon transfer limitations [12, 16, 30].

2.5.1.1. Photon transfer limitations

The first step in the photocatalysis process is the transportation of light through the reactor to the catalyst surface. A parameter that needs to be investigated is the ratio of illuminated surface per unit reaction liquid volume inside the reactor in order to achieve sufficient illumination of the catalyst. This will improve the illumination efficiency and hence the overall productivity of the photoreactor system. This term is denoted by kappa (κ). This parameter, however, does not consider the average power efficiency and the uniformity of light incidence [16, 31].

Average power efficiency, which is the ratio of the average incident/emitted light power, is dependent on the light intensity and light absorption. The light intensity decreases inversely with square distance from the light source. This indicates for optimal illumination the catalyst should be as close as possible to the light source. Average light radiance is calculated by Equation (6), where P_{lamp} is the emitted radiant power of lamp (W) and l is the distance from the lamp to the catalyst surface.

$$H_c = \frac{P_{lamp}}{l^2} \tag{6}$$

Light absorption follows Lambert-Beer's law (see Equation (7)),

$$log_{10}\frac{P_0}{P} = \varepsilon l c \tag{7}$$

where P_0 is the radiant power before absorption (W), P is the radiant power after absorption (W), ε is the molar absorptivity of absorbing species ($mol^{-1} \cdot m^{-1}$), l denotes the light path length (m), and C denotes the concentration of absorbing species.

Uniformity of light is important since the activation of the catalyst requires a minimum amount of energy. Current photoreactors have not achieved uniform illumination within the reactor [16, 32].

There has been one major development in improving illumination efficiency and uniformity. This was done by the introduction of optical fibres [12, 16, 27, 30, 31]. The concept behind using optical fibres is that it will allow light to travel uniformly through the fibre length similar to signal transmission in telecommunications. These fibres can be incorporated into the reactor (see Figure 2-6 and Figure 2-7).

2.5.1.2. Mass transfer limitations

Photo-reactors, like conventional reactors, may operate under mass transfer limitations. There has been a great amount of research done to improve mass transfer in reactors, which has led to several reactor design improvements.

Once the catalyst is activated by light, there should be maximum contact between the reaction liquid and the catalyst. The most common photoreactor is an annular, slurry reactor, which typically consists of a single lamp immersed in a slurry which contains both catalyst and target liquid (see Figure 2-4) [12, 30]. The catalyst particle size in these types of slurry reactors is small, thus resulting in minimal internal mass transfer limitations.

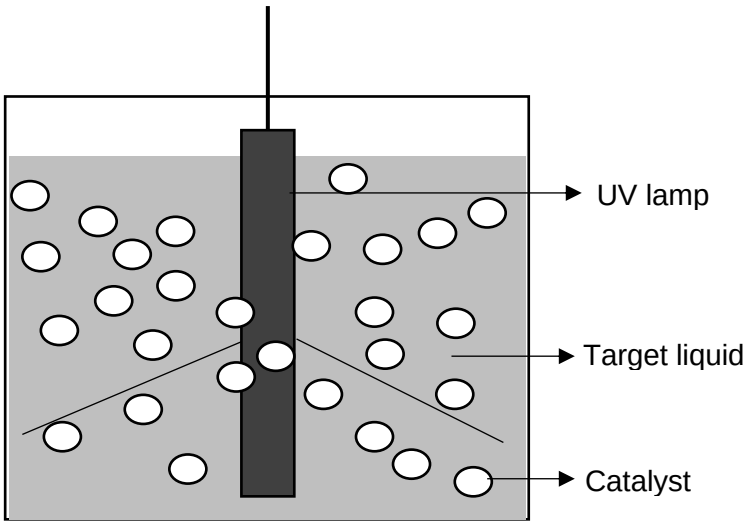

Figure 2-4: Rough sketch of a slurry photo-reactor adapted from van Gerven *et al.* [16]

The small catalyst particles used in slurry reactors require a costly catalyst separation process in the reactor set-up, which leads to the design of immobilised catalyst photoreactors, such as the spinning disc reactor (see Figure 2-5), monolith reactor (see Figure 2-6) and optical fibre

reactor (see Figure 2-7). Spinning disc reactors (SDR) consists of a disc on to which the slurry is pumped creating a thin film layer on the disc, which is then illuminated as the disc spins. Spinning disc reactors (SDR) have improved mass transfer due to the combination of both the thin film and turbulent flow. This will thus result in a higher mass transfer coefficient and thus a higher conversion [12, 16, 30].

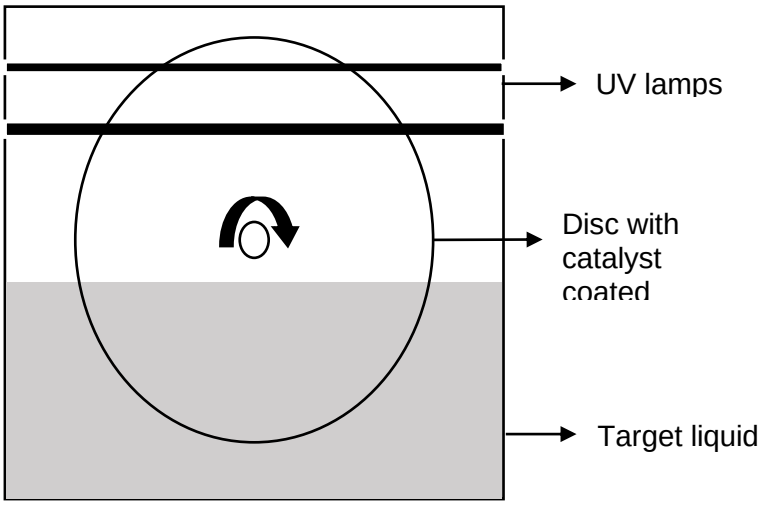

Figure 2-5: Rough sketch of a spinning disc photo-reactor adapted from van Gerven *et al.* [16]

In the monolith reactor (see Figure 2-6), the catalyst is immobilised on the wall of a monolith. Light is being guided to the catalyst in the reactor using optical fibres. In this set-up, the flow pattern of the reaction medium in the channels of the monolith and the thickness of the catalyst layer on the channel walls may become an important factor determining the overall conversion if mass transfer is limiting. Furthermore, the volumetric productivity of this set-up may remain low, realizing that the amount of photocatalyst which can be illuminated and which can be incorporated in this reactor set-up is limited.

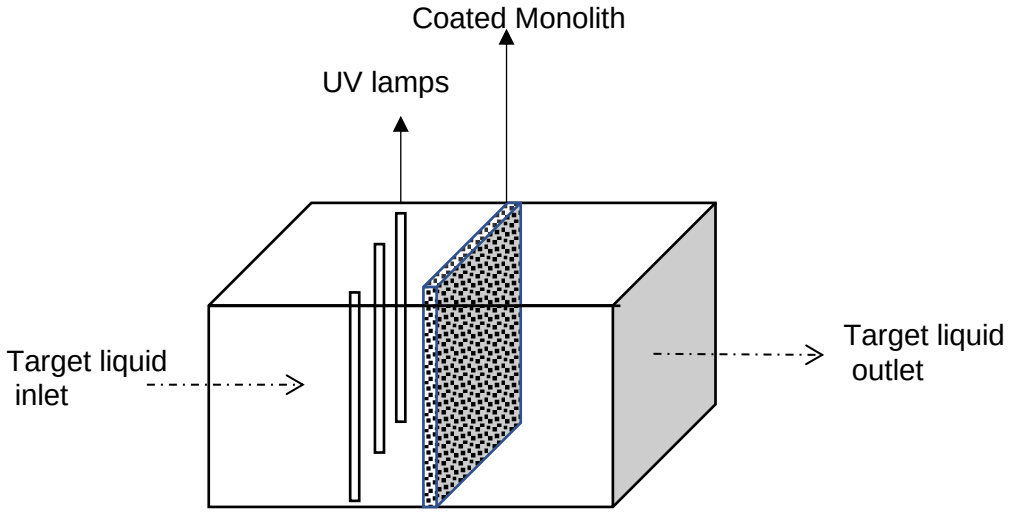

Figure 2-6: Rough sketch of a monolith photo-reactor adapted from van Gerven *et al.* [16]

Alternatively, the catalyst can be immobilized on the optical fibre itself (see Figure 2-7). The optical fibre reactors are meant to increase the surface area/volume ratios by coating the catalyst on the fibre, thus, decreasing the mass transfer limitations [12, 30]. Furthermore, there is an increase in the amount of catalyst in the optical fibre photo-reactor per unit reactor volume in comparison to the monolith photo-reactor.

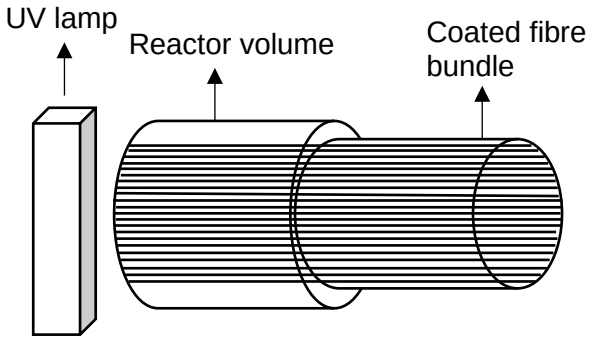

Figure 2-7: Rough sketch of an optical fibre photo-reactor adapted from van Gerven *et al.*]16]

In general, mass transfer limitations are well-known in chemical reactors, which can be reduced by increasing turbulence within the reactor system, thus increasing the contact between catalyst and reagents. Since mass transfer limitations are a problem in all reactors, it is not seen as critical as photon transfer limitations [17, 29].

2.5.2. Reporting results in heterogeneous photocatalysis

Efficiency is typically described as the ratio of energy used to the energy supplied. In photocatalytic studies, there is a diverse range of terms used to report efficiencies (see Table 2-1). This is because in different fields within the study of photocatalysis and photo-reactors, different terms are used to report the same efficiency. This makes it difficult to make comparisons between photo-reactor systems [28, 29]. Due to these inconsistencies, there is a need for a benchmark by which photocatalytic systems should be measured. There are currently two efficiency terms that are commonly used in literature. First, the apparent first-order reactor rate constant, k, which shows conversion rate (min^{-1}) can be used to compare different reactors. However, since this rate constant is volume-dependent, it does not give any indication of the reactor throughput [29]. Furthermore, it is also dependent on light intensity and catalyst loading. The second term, most commonly used in photocatalytic studies, is photonic efficiency which is very similar to quantum yield. This is representative of the light utilization within the reactor. However, even by recording the illumination efficiency or the rate constant there is no indication of the reactor productivity [27, 28].

A solution to this problem is by using the ratio of the space-time yield (STY) to the standardised lamp power output for comparisons between photoreactor systems [29]. Space-time yield can be calculated by taking the inverse of passage time and should be standardised to 1 m^3

volume. Standardised lamp power can be calculated by taking the ratio of the lamp power consumed (kW) to the volume of the reactor (m^3) [31]. Therefore, the photocatalytic space time yield (PSTY) is the ratio of both STY and lamp power (PL). This benchmark is successful for comparing productivities between different reactor systems which are not the same in terms of variables such as reactor configuration and light sources [17]. Moreover, this benchmark allows for research within this field to be furthered without discrepancies in efficiency terms used for reactor comparisons.

Table 2-1: Efficiency terms used in photocatalysis and photoreactor systems adapted from [31]

Term	Description	Equation
Efficiency	Ratio of energy used to the energy supplied	$\text{efficiency}\ (\%) = \frac{\text{Energy output}}{\text{Energy input}} \times 100$
Quantum efficiency, QE	Ratio of given photochemical reaction rate over total absorbed photon flux	$\text{QE} = \frac{\text{rate of reactant consumed or product formed}}{\text{Photon flux}}$ $\text{Photon flux}, q_p = \frac{dN_p}{dt}$, where N_p is the number of photons
Quantum yield, $\phi(\lambda)$	Ratio of the number of defined events per photon absorbed	$\phi(\lambda) = \frac{\text{amount of reactant consumed or reactant formed}}{\text{amount of photons absorbed}}$
Photonic efficiency, $\xi(\lambda)$	Ratio of the rate of photo-chemical reaction to the incident photons at initial conditions $(I_{(0)})$ within a specific time interval	$\xi(\lambda) = \frac{\text{rate of photochemical reaction}}{I_{(0)}(\lambda)}$
Photonic yield, $\xi(\lambda)$	Ratio of the rate of photo-reaction to the rate of an incident photon of monochromatic light $(q^0_{p,\lambda})$ that enters the reactor window at initial conditions within a specific time interval.	$\xi(\lambda) = \frac{\text{rate of photochemical reaction}}{q^0_{p,\lambda}}$
Standardised space time yield, STY	Inverse of passage time standardised for a volume of 1 m^3	$STY_r = \frac{V_r}{\tau}$ $\text{Where}, V_r, \text{is standardized to } 1m^3$
Standardised Lamp power, LP	Ratio of power (kW) of the experiment to the inverse of the volume (m^3) used in the experiment.	$LP = P \times \frac{1m^3}{V}$ Where LP is light source dependent
Photocatalytic space-time yield, PSTY	Ratio of standardised Space time yields to the standardized lamp power.	$PSTY = \frac{STY}{LP}$

2.5.3. Experimental parameters affecting a photocatalytic reactor system

There are several reaction parameters that affect photocatalytic reactions, and these should be adjusted to achieve the best performance. These include but are not limited to type of photocatalyst, reactor configuration, catalyst particle size or catalyst layer thickness, reactor configuration, temperature, pressure, polarity of the solvent, as well as light source and light intensity. Since the photocatalytic reduction of CO_2 is a new research field, there are very limited resources available for comparison. Table 2-2, compares the performance of five different reactor systems for the photo-reduction of CO_2. It can be seen that for there was a great difference between productivities in the systems studied. The highest productivity of methanol (519 $\mu mol \cdot g_{cat}^{-1} \cdot hr^{-1}$) was obtained with a Cu-C/TiO_2 catalyst in a slurry reactor using UV-light (λ = 365 nm). The performance of optical fibre photo-reactors is much less although the difference in the catalyst may be a contributing factor [1, 6].

Temperature affects all reactor systems including photocatalytic reactors. According to Lais *et al.* [34], the temperature has a large effect on the photocatalytic reduction of CO_2 to methanol. They postulated that an increase in temperature increases the reaction rate, in particular, improving the product desorption from the catalyst surface. A lower reaction temperature improves the adsorption of the reactant onto the surface as well as improves CO_2 solubility [33, 34].

Light intensity plays a major role in photocatalytic systems directly affecting the conversion [5, 36]. However, an increase in light intensity also results in an increase in the recombination rate of charge carriers, which ultimately leads to a decrease in quantum efficiency [16, 35]. The recombination rate of the excited electron-hole pairs can be reduced by adding hole scavengers to the reaction medium. These may react with the hole so that the electron can be used in the reduction reaction [36]. In the CO_2-reduction from a bicarbonate solution, the bicarbonate itself may act as a hole scavenger. Hence, bicarbonate may also act as a sacrificial agent reacting with the holes to produce protons [16].

The use of coated optical fibres introduces new variables that may affect the light intensity which reaches the catalyst, such as the optical fibre length, fibre diameter, as well as the thickness of the coating on the fibre (i.e. the amount of TiO_2 that is coated onto the fibre) [6, 35, 36].

Table 2-2: Comparison of photocatalytic reactor systems for CO_2-reduction

Photocatalyst investigated	Operating conditions		Reactor Type	Maximum productivity achieved in the study			Reference
	Temperature	*Light source*		*Product*	*Photocatalyst*	*Productivity ($\mu mol/g_{cat} \cdot h$)*	
Cu-C/TiO_2 [1]	Ambient	UV lamp - 365 nm	Stirred annular reactor	CH_3OH	3 wt.-% Cu -C/TiO_2	519	[18]
-C/ TiO_2[1]							
-NiO- TiO_2/ACF[1]	80 °C	UV lamp - 395 nm	Stirred reactor	CH_3OH	NiO-TiO_2/ACF	378	[21]
-ACF/ TiO_2							
-P-25	Ambient	Hg lamp - 365 nm, 236 nm, 546 nm, 578 nm	Slurry reactor	CH_3OH	GO-TiO_2	47	[10]
-GO							
-GOT							
-Cu/ TiO_2[1]							
-Cu/GOT							
-Cu/ TiO_2	75 °C	Hg lamp - 365 nm	OFPR[3]	CH_3OH	1.2 wt.-% Cu/TiO_2	0.45	[6]
-P-25	75 °C	Hg lamp - UVA (320-500nm) UVC (250-450nm)	OFPR[3]	CH_4	1 wt.-% Cu/TiO_2	0.24	[1]
-Cu/TiO_2[1]							

[1]: P25; [2]: activated carbon fibre ACF; [3]: Optical fibre photo-reactor

2.6. Optical fibre photocatalytic reactors (OFPR)

The optical fibre photoreactor (see Figure 2-7) has been studied for use in photocatalysis, since the use of a catalyst coated optical fibre is a promising route to overcoming photon transfer limitations.

Optical fibres can be treated as elementary waveguides, where the light enters in the form of a plane wave [15]. These light waves propagate through the fibre core, from the refractive index of n_1 onto the outer medium with a refractive index, n_2 , where it can either be refracted or reflected. Currently, optical fibre is used to transmit signals over large distances without loss of signal strength and is largely used in telecommunications where it works on the principal of *total internal reflection*. This occurs when the light waves travel from a denser medium (silica fibre) to a less dense medium (coating) ($n_1 > n_2$) (see Figure 2-8). According to Snell's law, the ratio of the sine of the incident angle (θ_1) of the wave to the sine of refracted angle (θ_2) of the waves is constant – this ratio is always equal to the waves velocities in their respective mediums and the inverse ratio of their refractive indices [4, 14, 36].

$$n_1 \, sin\,(\theta_1) = n_2 \, sin\,(\theta_2) \tag{8}$$

At an angle less than the critical angle (θ_C) the incident light wave (θ_1) it will be completely refracted back into the core. The critical angle can be determined by setting the angle of the refracted wave perpendicular to the normal of the interface (θ_2= 90°, $\sin(\theta_C) = {}^{n_1}/_{n_2}$) . Figure 2-8 summarises the various behaviours of light. The refractive indices differ for different materials as it is a function of the molecular mass of that material, M, the molar refractivity, R, and the density of the material, ρ [33]:

$$n = \sqrt{\frac{M + 2R \cdot \rho}{M - 2R \cdot \rho}} \tag{9}$$

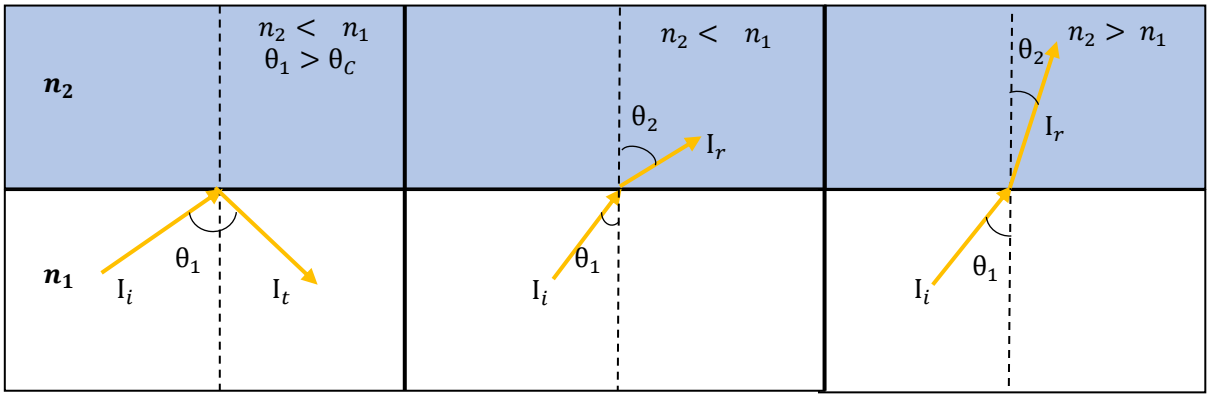

Figure 2-8: Conditions for reflection and refraction of light adapted from Peatross and Ware, (2010)

Figure 2-9, below, demonstrates the various light pathways in a single piece of optical fibre; with polymer coating, without polymer coating (bare fibre) and with a catalyst layer. Depending on the refractive index of the fibre and the catalyst, a portion of the light will be refracted (2), activates the catalyst (3) or scattered (4). The rest of the light will be reflected into the fibre core (5) and is transmitted with a similar process along the fibre length. The refractive indices of the optical fibre, TiO_2 layer and air are 1.46, 25.5 and 1.00 respectively [4] implying that the critical angle for the fibre-air system is 43.2º, whereas the critical angle for the system fibre-TiO_2 is only 3.3º. However, the latter can be manipulated by changing the density of the catalyst layer [39].

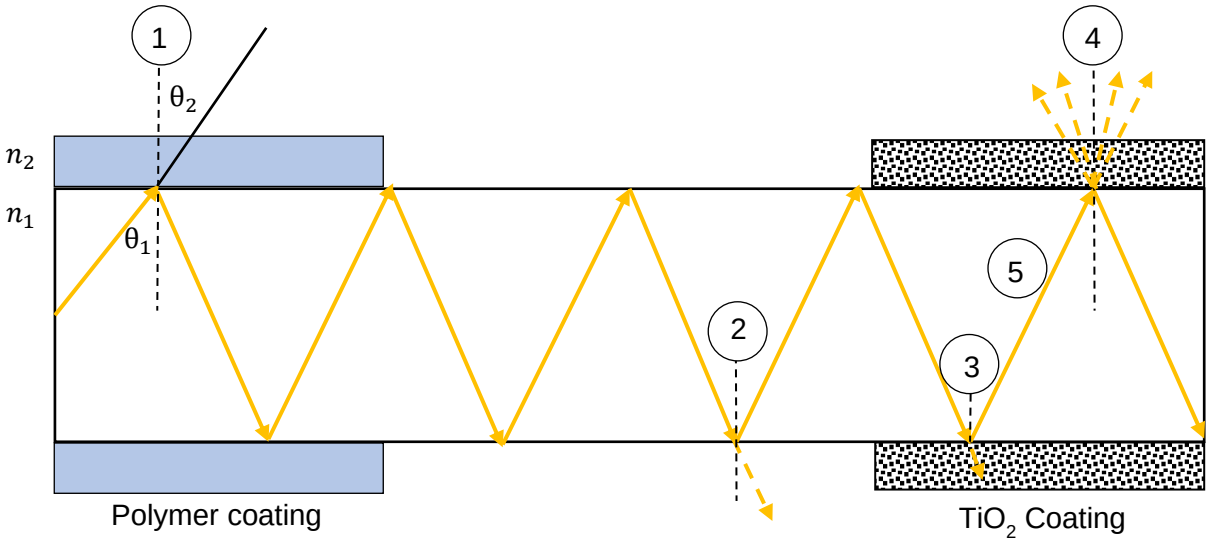

Figure 2-9: Various light pathways in an optical fibre

Wang and Ku. [38], developed a light transmission model for coated optical fibre. This model is based on a total energy balance of light flux through the optical fibre and takes cognizance

of findings of Peill and Hoffmann. [14], that the light absorption in the fibre and the thickness of the catalyst coating is related via Lambert-Beer's Law, Equation (10):

$$I_{abs}/I_{input} = 1 - e^{-\varepsilon\delta} \tag{10}$$

where $\boldsymbol{\delta}$ and $\boldsymbol{\varepsilon}$ are the thickness of the TiO_2 layer and extinction coefficient, respectively. Hence, the fraction of light absorbed is directly proportional to the thickness of the coating thickness. The limited penetration of the refracted light is determined by the extinction coefficient and is reported to be less than or equal to 0.006 nm^{-1} for TiO_2 [14, 38]. This implies that a catalyst coating with a thickness of ca. 0.75 µm will absorb 99% of the refracted light coming into the titania layer.

The light transmission over the whole fibre can be obtained from a light intensity balance across the optical fibre:

$$I_{input} = I_{abs} + I_{trans} \tag{11}$$

where I_{input} is the light intensity that enters the optical fibre from the source, I_{abs} is the light intensity that is absorbed by the TiO_2 photocatalyst coating and I_{trans} is the light intensity that is transmitted through the fibre [41].

The light intensity distribution of light travelling through a coated optical fibre illustrates a decay in light intensity along the axial direction of the optical fibre [38, 40],

$$I_{f(x)}/I_{input} = e^{-\alpha x} \tag{12}$$

where $I_{f(x)}$ is the light intensity at any position x along the fibre and α is the attenuation coefficient of the TiO_2 layer.

The incident angle of the light wave entering the fibre determines both the reflection and transmission distance between each reflection for a given a core-diameter. According to Fresnel and Snell's laws, the ratio of the light intensities of the refracted and reflected light waves of each reflection depends on the incident angle and refractive indices. Equations (13) and (14) describe the ratios for the transverse electric polarisation of light waves (∥) and transverse magnetic polarization (⊥), respectively. The contribution of both is expressed as $R(\theta_i)$, which is the average Fresnel reflection coefficient (Equation (15)).

$$R_{\parallel} = \frac{\tan(\theta_i - \theta_t)}{\tan(\theta_i + \theta_t)} \tag{13}$$

$$R_{\perp} = \frac{\sin(\theta_i - \theta_t)}{\sin(\theta_i + \theta_t)} \tag{14}$$

$$R(\theta_i) = \frac{1}{2}({R_{\parallel}}^2 + {R_{\perp}}^2) \tag{15}$$

It was proposed that refraction or reflection takes place between both the quartz-air and quartz-TiO_2 interfaces simultaneously due to the inhomogeneous coverage of TiO_2 on the surface [40]. However, the quartz-TiO_2 interface has shown some degree of refraction into the TiO_2 layer.

Hence, the light intensity distribution along the axial direction of the fibre with the incorporation of the Fresnel reflection contribution on the TiO_2 layer as well as UV absorption by the optical fibre [40] can be described as:

$$I_{f(x)} = I_{input} \times R(\theta_i)^m \, e^{-\alpha_f x} \tag{16}$$

where m is the number of reflections in the optical fibre.

The coating thickness affected the partitions of TiO_2-quartz and air-quartz; therefore, it is important to determine the average effective coverage of TiO_2 particles on the fibre surface (X_T). The remaining area which is not covered by TiO_2 particles are regarded as the air stream (X_A). The total coverage of the fibre can then be expressed by the following Equation (17):

$$X_T + X_A = 1 \tag{17}$$

Combining Equations (15), (16) and (17) results in an expression that quantifies the light intensity distribution along the fibre length by incorporating the cumulative sum of both the Fresnel reflections (R) between the TiO_2-quartz and air-quartz interfaces as well as the attenuation absorption of the optical fibre:

$$\frac{I_{f(x)}}{I_{input}} = X_T R(\theta_i)^m \, e^{-\alpha_f x} + X_A \, e^{-\alpha_f x} \tag{18}$$

Therefore, by varying the parameters, the light intensity can be modelled according to Equation (19), below, which is a combination of Equations (16), (17) and (18). This creates a relationship between coating thickness and average effective coverage of the surface. The loss of UV light by the fibre material is compensated for in the equation, by x, which also represents the fibre length. Furthermore, it improves the accuracy of the model.

$$X_T = \frac{1 - e^{-\varepsilon\delta + \alpha_f x}}{1 - R(\theta_i)^m} \tag{19}$$

It can be seen that the light intensity decays along the fibre length, x (this is also known as light attenuation). The light intensity decreases exponentially along the axial direction of the catalyst coated optical fibre [4, 16, 38]. According to Wang and Ku [38], there is 99% refraction of light after 10 cm of coated fibre and only a 60% refraction of light on uncoated stripped fibre for the same length. These results vary as a function of coating thickness and incident angle (see Equation 19). More light is refracted on a thicker coating ultimately causing less light to travel through the fibre. A thicker catalyst layer will result in a higher recombination rate for excited electron and hole pairs thus reducing the photon efficiency [4, 37]. This is because there is a higher likelihood for the electron to recombine before it can be consumed at the catalyst surface [36]. Furthermore, a thick catalyst coating is not desired as this may introduce internal mass transfer limitations, since the distance that the reagents have to diffuse through the catalyst layer to reach the active sites increases [41]. Thus, there is a clear trade-off between the thickness and having sufficient catalyst in the reactor. The optimum thickness is thought to be between 0.4 – 1.1 μm [16, 39].

Another important parameter is the fibre diameter, whereby a larger diameter yields fewer reflections and fewer refractions. Therefore, the fibre diameter has a direct effect on light propagation, which ultimately affects light attenuation [16, 35]. The number of reflections can be adjusted by varying the angle, at which the light is introduced into the reactor.

The third problem with the currently used optical fibre photo-reactors is their low catalyst loading. They typically contain 50 - 200 pieces of fibre or rods, thus leaving a large portion of the reactor volume unutilised [6, 37]. Therefore, assuming that coating layers range between 0.4 -1.1 μm, there is a low catalyst mass and surface area in the reactor. It is proposed that a reactor packed with coated optical fibres would utilise the reactor volume more efficiently by increasing the catalyst mass and surface area. However, an increase in optical fibre in the reactor decreases the fluid flow, which could result in an increase in the pressure drop across the reactor [14, 16, 35, 38].

It has been reported that at high light intensities there is a high recombination rate, therefore, it can be said that the light intensity is inversely proportional to the quantum efficiency [17]. This problem can be overcome in an optical fibre reactor by decreasing the intensity but increasing the number of fibres within the reactor.

2.7. Preparation of TiO_2 coated the optical fibre

2.7.1. Fibre optic strength

Optical fibres are made of a quartz core and a polymeric outer layer. There are different types of optical fibre which vary in core sizes [42]. In the fibre-drawing process, a primary polymer coating is applied onto the bare fibre immediately after it is drawn, since bare optical fibre is extremely brittle. Therefore, this coating is responsible for the mechanical integrity of the fibre as it inhibits damage to the fibre surface as well as water diffusion through the cladding layer. The presence of water on silica coupled with mechanical stress (σ) and strain (ε_a) have been reported to cause stress activated corrosion also known as stress corrosions, since water molecules react with strained bonds in fused silica [43]. Stress corrosion gives rise to slow crack growth, which has a detrimental effect on the strength of fused silica fibres [43]. The strength of materials such as silica fused fibres is determined by stress concentrators such as flaws, cracks or distortions that occur on the surface or in the bulk [42]. In order to determine the lifetime of the fibres, it is important to study the strength and stress-ageing mechanics as well as its mechanical limitations [42, 43, 44].

Stress corrosion can be studied by performing fatigue tests. There are two types of fatigue tests i.e. static and dynamic fatigue. Static fatigue investigates the lifetime of the fibre when constant stress is applied. Dynamic fatigue test investigates the failure stress of the fibre when a constant stress rate is applied [42]. The two-point bending test (bending fracture test) investigates the failure strain of the fibre [41, 44–46]. It can be used to determine the strain, ε_a, where R is the radius of the curvature. The radius of the curvature is directly proportional to the distance L of the fibre axes according to equation (20). Where C_b = 1.1985. Substituting equation (20) into equation (21), the local strain is then given by equation (22). The failure stress can be determined from the failure strain by using the linear relation between and the Youngs modulus for the optical fibre of 72 GPa [41, 45]. These are important values to know for fibre handling during the coating process in order to reduce the chance of breakages.

$$R = \frac{L}{2C_b} \tag{20}$$

$$\varepsilon_a = \frac{d}{2R} \tag{21}$$

$$\varepsilon_a = \frac{C_b d}{L} \tag{22}$$

2.7.2. Coating mechanism

It has been established that to construct an optical fibre reactor a catalyst layer needs to be immobilised on to the optical fibre. There are various methods for the preparation of TiO_2 as well as several coating mechanisms that have been utilised. Methods of coating or nanoparticle deposition that are typically used are dip-coating, spin-coating, solvent evaporation and chemical vapour deposition [48]. However, due to the brittle nature of the optical fibre, the dip-coating processes seems to be suited. It is a simple and easy technique that can be waste-free, low cost and low energy [49]. Figure 2-10 below describes the process, through all 3 stages. Firstly, the substrate is immersed in a solution at a controlled speed (a). It can be immersed for a period of time before it can be pulled up (b). The substrate is then withdrawn either vertically or at an inclination angle at a controlled speed to avoid irregularities in the film. The excess liquid that has not converted into the film is drained off using gravitational forces (c). Lastly, the solvent is evaporated which forms a film onto the substrate [47 – 49]. It should be realised that evaporation already begins during the deposition and drainage stages. As the substrate is withdrawn several phenomena may occur resulting in the coating deposition, such as fluid draining by gravity, layer drying by solvent evaporations well as film-curing by chemical and physical reactions. Figure 2-11, demonstrates the withdrawing stage of the process in more detail [47 – 49]. Furthermore, it demonstrates the competing forces in the dip-coating process – the solution is pulled up with the substrate exposed to a drag force. At the liquid-gas interface, a force opposing the drag force is created by the surface tension. After evaporation of the solvent, the remaining undried solvent which has not formed a coating layer flows down the substrate back into the pool of solution due to the force of gravity.

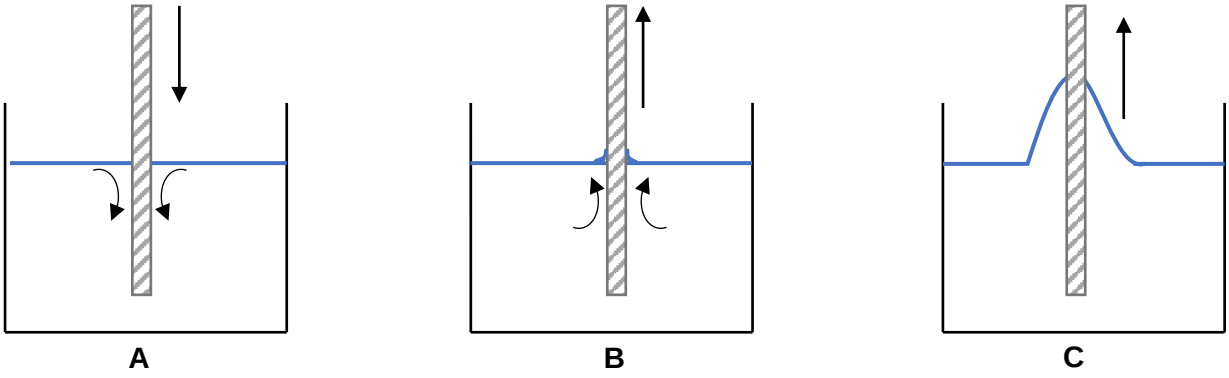

Figure 2-10: Overview of the dip-coating process

It is reported that this simple process for the deposition of a thin film has multiple variables. Film thickness and film morphology are determined by parameters such as immersion time,

withdrawal speed, coating cycles, viscosity and density of coating solution, as well as substrate surface area [52]. The thickness (h) (μm) of the coating layer can be expressed by the Landau-Levich equation for a Newtonian fluid,

$$h = 0.946 \times \frac{(\eta \upsilon)^x}{\gamma^{\frac{1}{6}} \sqrt{\rho g}} \tag{23}$$

where g is the gravitational force, ρ is the density of the liquid, υ is the withdrawal speed (mm.min^{-1}), η is the liquid viscosity, γ is surface tension and x is a constant. The value of x depends on the geometry of the surface. The position at which the measurement is taken is relative to the drying line where $x = 0$ [53, 54].

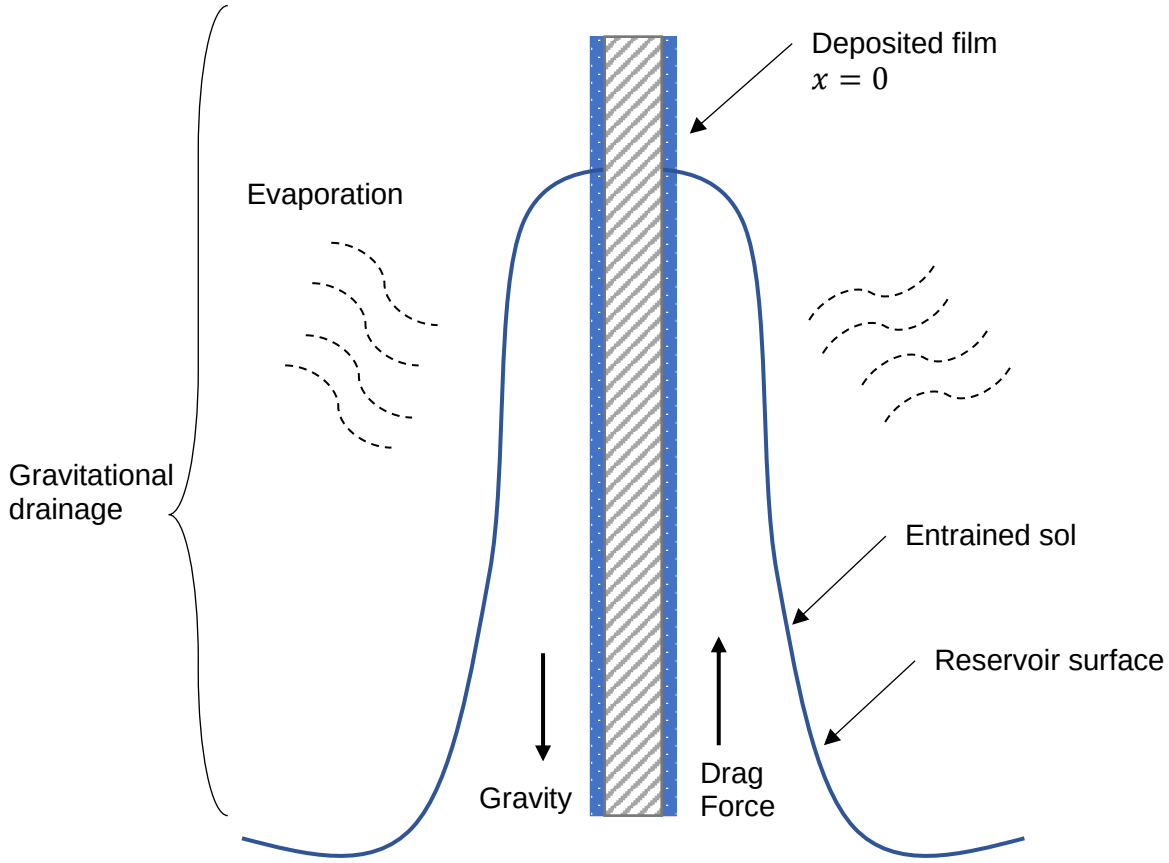

Figure 2-11: Dip coating mechanism

Using the dip-coating method, there are various ways to deposit TiO_2 photocatalyst onto the fibre. This layer needs to be homogenous and have a consistent thickness. To date, there have been two methods of coating optical fibres with catalyst, namely the sol-gel technique and slurry technique.

2.7.2.1. Sol-gel based dip coating

Sol-gel technique uses inorganic or metallo-organic precursors. Figure 2-12 illustrates the sol-gel process. These precursors can either be hydrolysed or condensed at a low temperature in aqueous or organic solvents resulting in the formation of a sol, a stable suspension of colloidal particles in a liquid. In the gel phase, a colloidal suspension containing a solid skeleton within a liquid phase is formed by the creation of covalent bonds from polycondensation reactions. The period required for the transition from sol to gel is known as the "gelation time". Xerogel is the gel after evaporation, under normal conditions, which is further treated by heat to produce the desired catalyst.

Hydrolysis (acid catalysed) and condensation may occur simultaneously, as shown in reactions below:

$$Hydrolysis \quad M - OR + H_2O \rightarrow M - OH + ROH \tag{24}$$

$$Condensation \quad M - OR + XO \rightarrow M - O - M + XOH \tag{25}$$

where R represents an alkyl group and X represents either hydrogen or an alkyl group.

The rates of the reactions can be controlled by varying parameters such a temperature, pH, water addition as well as the addition of a precursor. Condensation is favoured under alkaline conditions to produce a highly branched gel network, whereas hydrolysis is favoured under acidic conditions to produce a slightly branched gel network.

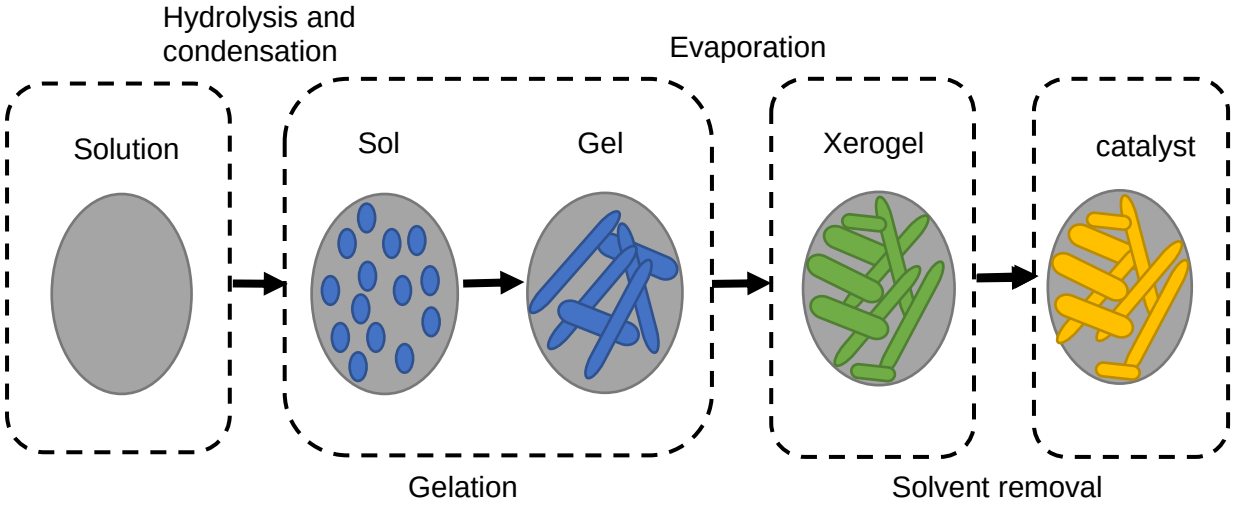

Figure 2-12: Overview of sol-gel process

2.7.2.2. Slurry based dip-coating

Slurry based dip-coating is based on the electrostatic interaction between the solution and the substrate. The electric charge used is the surface zeta-potential. The zeta-potential can be varied depending on the pH. The zeta-potential is related to the pH through the following equation:

$$TiOH_2^+ \overset{+H^+}{\underset{-H^+}{\leftrightarrow}} TiOH \overset{+H^+}{\underset{-H^+}{\leftrightarrow}} TiO^-$$

The isoelectric point, pH_{iep} is defined as the pH at which the material has a neutral charge, i.e. a net electric charge of zero. Figure 2-13, below, demonstrates the trends between the relationship of zeta-potential and pH for glass fibres, P25 TiO_2, as well as $Ti(OBu)_4$ which is a precursor in the sol-gel method [53, 54]. When the pH < pH_{iep}, the zeta-potential is positive which would promote preferential adsorption of anions on the surface. Furthermore, when the pH > pH_{iep}, preferential adsorption of cations on the surface is promoted. It has been reported that the pH_{iep} for P25 TiO_2 (slurry) and a gel derived from $Ti(OBu)_4$ is approximately 7.2 and 6.5, respectively [53, 54]. Glass is reported to have a pH_{iep} of approximately 2 [56, 57]. The low pH_{iep} of glass indicates that surface groups have a low affinity towards protons. In order for electrostatic adhesion of the solution to the substrate to occur the polarity of the surface charges must be opposite. By this, attraction of the solutions to the substrate may occur. According to Figure 2-13, below, the ideal pH to work for both slurry and sol-gel methods is between 3-6. This ensures adhesions via electrostatic interaction [56, 57].

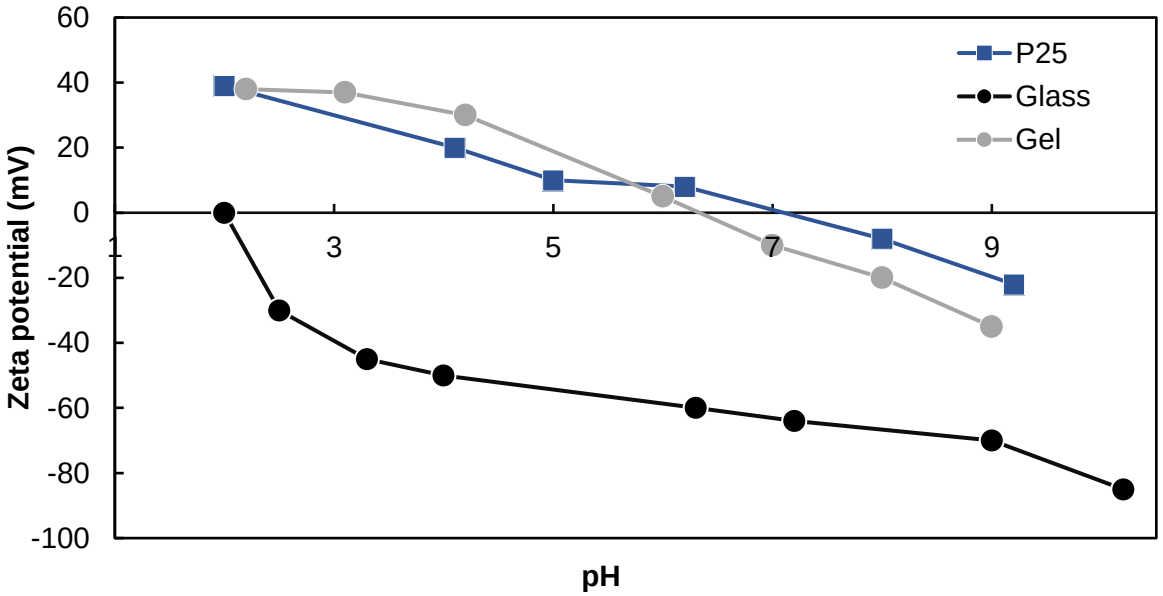

Figure 2-13: Zeta potential vs pH trend for P25, glass, and gel prepared from $Ti(OBu)_4$ using ethanol as a solvent ($Ti(OBu)_4$/ethanol molar ratio 1:10) adapted from [56, 57]

2.7.2.3. Variables affecting optical fibre coating

There are several variables that have been reported to affect the thickness and homogeneity of the catalyst layer coated on to the optical fibre via the dip-coating method, namely; fibre pulling rate, viscosity of catalyst suspension, pH of catalyst suspension, number of coatings and the form of TiO_2 suspension (slurry or sol-gel), as well as the addition of a surfactant.

Dip-coating of optical fibre for the use in optical fibre photoreactors has not been greatly researched. The effect of the substrate pulling rate has shown a proportional relationship with the thickness of the catalyst layer for pulling rates been 5 - 50 mm/min [6,55]. The viscosity of the TiO_2 suspension can be varied by changing the concentration of TiO_2 in the suspension. This is directly proportional to the coating thickness, with observed thicknesses of 0.75 µm - 4 µm for TiO_2 contents ranging from 1.25 wt.-% - 20 wt.-%. For various applications of these optical fibres, the average optimal thickness ranged between 0.4 µm - 1.1 µm [1, 3–5]. As seen in section 2.7.2, the pH of the suspension influences the degree of particle agglomeration and therefore the TiO_2 coating thicknesses on the optical fibre. These attractions result in particle agglomeration and hence an increased thickness [2, 14]. Lastly, multiple coatings result in an initial increase in coating thickness [1, 3–5]. However, an increased layer thickness may result in the formation of cracks in the coating layer. It has been reported that surfactants such as polyethylene glycol (PEG) can be used to reduce cracking, increase thickness and create pores in the coating layer [57].

The optical fibre coating process is multistep and must be done with extreme precision and caution so that no damage is done to the coating layer. To achieve a 1 g catalyst loading in the photoreactor of 0.7 µm coating thickness, 1.8 km of optical fibre will need to be coated. This would result in hand-coating 18 000 pieces of optical fibre assuming, 10 cm pieces of optical fibre are installed into the reactor. These coated optical fibre pieces must all have identical coating thicknesses which would require it to be withdrawn from the dip-coating process at a constant speed. This process would prove to be extremely time-consuming. Therefore, an automated continuous fibre coating process needs to be created to mass produce coated optical fibre.

3. Objectives

3.1. Problem statement

CO_2 may be captured from these point sources by absorption in an aqueous solution of NaOH. CO_2 can be photocatalytically converted into useful hydrocarbons using water as a reducing agent, and possibly using titania as the photocatalyst. This is an attractive route since solar energy is abundant and can be utilised without producing more CO_2.

To date, photoreactors have not achieved commercial conversions for CO_2 reduction. There are various factors that affect the reactor system's productivity in CO_2 reduction process. The main issue is related to photon transfer limitations. This occurs when there is insufficient light illumination of the catalyst surface in the reactor. Optical fibres have been widely used in telecommunications to transport signal and can potentially be used to transport light uniformly through a reactor. The catalyst can then be immobilised on to the fibre.

However, a large amount of fibre is required to achieve a significant catalyst loading within the reactor. To achieve a 1 g catalyst loading in the photoreactor with optical fibres coated with a catalyst layer with a coating thickness of 0.7 µm, would require the coating of 1.8 km of optical fibre. In order to produce a large volume of coated optical fibre, a multistep process must be developed in order to control coating thickness in an automated process.

3.2. Scope of study

The scope of the project is to design, construct and commission an automated process to increase the production volume of catalyst coated optical fibre from raw fibre (fibre including cladding) hence making the processing time-efficient and controllable by determining the various configurations and process parameters that affect the production.

3.3. Research Objectives

- Determine a method, including appropriate conditions, in which the cladding of optical fibre can be removed.
- Investigate methods to wash the bare fibre
- Determine process variables that affect the coating thickness of optical fibre
- Develop a start-up and shut down procedure for the process
- Characterise coated fibre

- Design construct and commission an automated optical fibre catalyst coating process (AOFCCP)
- Commission the automated optical fibre catalyst coating process to produce coatings between 0.4 – 1.1 µm

3.4. Design problem

The aim of the project is to design, construct and commission an automated optical fibre catalyst coating process to produce controllable uniform catalyst coating thicknesses on optical fibre, in order to make the process time efficient and increase the production volume of coated optical fibre. The system must include the 4 essential steps required for optical fibre preparation by-hand which are polymer coating stripping, washing of bare fibre, dip-coating and drying or calcination of coated optical fibre. The AOFCCP must be commissioned to perform 2 types of coating, namely a sol-gel suspension or P25 TiO_2 slurry. Controllability must be achieved by determining the relationship between the catalyst coating thickness and morphology and the system's process variables namely, pH, heat treatment, catalyst slurry concentration and pulling speed are used to determine the extent of controllability in the system.

3.5. Key Questions

- How can the thickness of the catalyst layer adhered to the fibre be changed?
- How does the coating surface coverage and thickness differ between the sol-gel and p25 slurry coating methods?
- Does the process sufficiently replicate the coating produced in literature?

3.6. Sustainable development goals

The project that will be undertaken will focus on the following sustainable development goals (SDG) 7, 9, 11, 12 and 13. This is because the project investigates CO_2 mitigation. CO_2 will be converted to methanol photocatalytically reducing the amount of thermal energy required. This project addresses SDG 9 and 12 by developing a novel technology that can be introduced into industry promoting responsible consumption and production. Furthermore, it addresses SDG 7, 11 and 13 by reducing the CO_2 emissions thus decreasing the concentration of CO_2 in the atmosphere and decelerating global warming. The ultimate aim of this project is to utilise solar energy for the conversion of CO_2 and thus no electrical power would be required.

4. Experimental Set-Up

This chapter will outline the experimental set-up. The process unit's functions and experiments described below collectively provide an investigation into the viability of an automated optical fibre catalyst coating system to produce controllable catalyst thicknesses by various process variables.

4.1. Preliminary development of block flow diagram

The primary goal of this thesis was to design, construct and commission an automated optical fibre catalyst coating process for the use in photcatalytic reactor systems. A major requirement for the process is to produce optical fibre with adjustable coating thicknesses. The overall process is summarised by the block flow diagram given in Figure 4-1.

Polymer-coated optical fibre is fed into the process as raw material from Unit 1. The protective polymer coating is stripped using acetone in Unit 2, exposing a bare fused silica optical fibre rod, which is washed in a 0.5 M sodium hydroxide solution in Unit 3. The dip-coating method is used in Unit 4 to coat the washed fibre with the desired catalyst. The wet optical fibre catalyst coated is fed directly into Unit 5, where it is dried and calcined at the desired temperature. The product is then collected on a spool in Unit 6, at the end of the process. The optical fibre that is pulled through the process is guided by rollers which are strategically located between units.

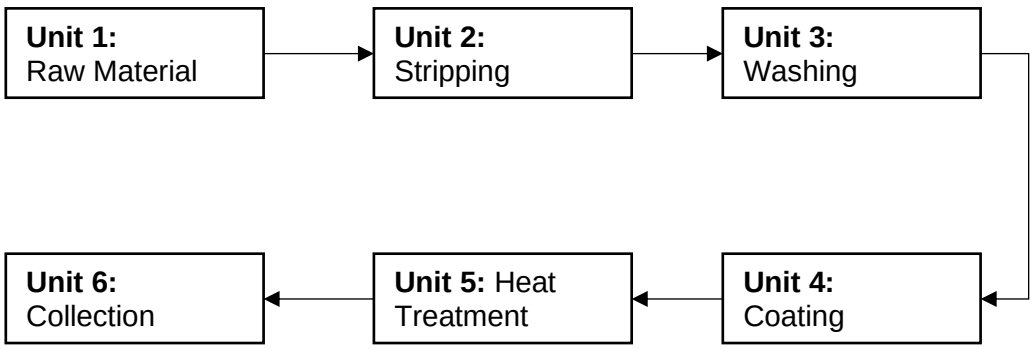

Figure 4-1: Block flow diagram of the proposed process to automatically coat optical fibre with a photo-catalyst

4.2. Identification and formulation of design requirements

A list of design requirements for the proposed process was formulated (see Table 4-1). These process design requirements had been identified specifically to meet product specifications. These requirements act as a platform for which the completed process can be evaluated to determine its performance against the initial outline requirements. Justifications for each of the specifications can be found in the detailed unit design and overall system layout (S).

Table 4-1: Process design requirements and specifications

No.	Unit	Design requirement	Description	Achieved	Demand /Wish
a	S	Automated process	Automated, continuous movement of optical fibre through the process	Yes	D
b	S	Repeatability	Replicate product specifications	Yes	D
c	1	Adaptability: Raw material	Using different optical fibres	Yes	W
d	4	Adaptability: Coating medium	Coating different catalysts	Yes	D
e	S	Adjustable set-up configuration	Ability to adjust roller positions or height.	Yes	D
f	5	Operating drying temperature	Unit 5 operating temperature requirements: **120°C - 700°C**	Yes	D
g	6	Speed control	Unit 6: Collection spool pulling speed requirements: **0.11** $\boldsymbol{mm/s}$ **- 3.15** $\boldsymbol{mm/s}$	Yes	W
h	2	Operating stripping temperature	Unit 2: Acetone stripping bath operating temperature range: **25°C - 50°C**	Yes	D
i	S	Controllable catalyst thickness	Controllable catalyst coating thickness (**0.4 µm - 1.1 µm**)	Yes	D

4.3. Identification of process variables

Various process variables are believed to have a direct effect on the coating thickness [18, 32, 38, 53, 54], such as the concentration of the slurry medium, the pH of the slurry medium, the pulling speed of the optical fibre through the process and the drying temperature. These variables may affect more than one process. For instance, the pulling speed effects, the withdrawal speed of the optical fibre in the dip-coating process (Unit 4) and the residence time in the oven (Unit 5). These variables can be adjusted or used in different configurations in order to achieve the desired product specification.

In this project, two dip-coating methods are studied, namely the slurry and sol-gel method. Slurry coating entails pulling the optical fibre through a suspension of P25 TiO_2 and water, whereas the sol-gel method involves the preparation of TiO_2 by hydrolysis of titanium butanate

[58] following which the optical fibre is pulled through the resulting gel. A list of the variables and ranges that are investigated for the respective coating methods in the associated units can be found in Table 4-2.

Table 4-2: Outline of process variables to be investigated

Location	Process Variable	Variable ranges as per coating method:	
		P-25 TiO_2	**Sol-gel**
Unit 4	pH of the coating medium	2.65 - 5.65	
Unit 4	Concentration of coating medium (wt.-%)	1 - 20	
Unit 5	Drying Temperature (°C)	200 - 500	400 - 600
Unit 6	Pulling Speed (mm/s)	0.11 - 3.46	

4.4. Detailed design of process units

A detailed design of the proposed system is separated into 6 process units and auxiliary components. This chapter will include the development of each individual unit and provide justifications for the design requirements found in Section 4.2. Moreover, detailed technical drawings will be provided which include the materials of construction for the respective units in the process. All measurements are in millimetres (mm) unless stated otherwise.

The optical fibre used in this study was supplied with the buffer polymer coating which is essential for its mechanical stability (see Table 4-3). The single mode optical fibre was obtained from CBI electric PTY (Ltd), RayCape.CC. It contained an optical fibre with a diameter of 125 µm covered with a polymer coating with a diameter resulting in an overall diameter of optical fibre and polymer coating of 245 µm. The optical fibre is delivered on a spool (ca. 1200 m and 900 g)

Table 4-3: Specifications of optical fibre used as raw material

Specification	Type
Manufacturer	CBI electric PTY (Ltd), RayCape.CC
Mode	Single
Primary polymer coating diameter (µm)	245
Outer fused silica diameter (µm)	125
Weight of spool with fibre (g)	900

4.4.1. Auxiliary Component Design: Rollers

The rollers are responsible for the transportation of the optical fibre through the process. The mechanical strength of the bare optical fibre is an important design variable to consider when designing the fibre coating process and in particular the rollers. Optical fibre is known to be very thin and brittle since it is, in essence, a thin (D = 125 μm) glass rod [42–44]. Therefore, the bending strength of the bare optical fibre was determined to ensure the fibre can be transported through the proposed process without intermittent breakage. It should, however, be noted that water and chemicals such as NaOH on the surface of the optical fibre may react with strained fused silica bonds, initiating slow crack growth which causes stress corrosion, thus ultimately affecting the mechanical integrity of the optical fibre [42–44].

Fatigue tests can be done to determine the stress of the optical fibre experimentally and thus determine the mechanical limitations of the optical fibre. In dynamic fatigue tests, the failure stress is investigated by applying constant stress. For the bending test experiment, a constant velocity of 1.86 cm.min^{-1} was used. The two-point bending test is the dynamic fatigue test used to determine the failure stress and critical radius of the optical fibre [42–44]. The critical radius is defined as the radius at which the optical fibre breaks when bent. The aim of this test is to determine the roller diameter limitation for the transportation of the optical fibre through the coating process by determining the critical radius and thus the critical diameter of the optical fibre.

The two-point bending test experimental set-up that is demonstrated by Figure 4-2 was used to determine the critical diameter of the bare optical fibre. Adhesive tape was used to secure both ends of the optical fibre against the face-plates ensuring the optical fibre is not misaligned to avoid fibre slip. The initial starting length (L) was recorded before the distance between the face-plates was periodically decreased. This causes an increase in strain located at point A. The distance L_f at which the optical fibre breaks was recorded and using equations (20), (22) and (23), shown in section 2.7.1, the critical radius, failure stress and failure strain was recorded. This experiment was repeated 10 times for an initial length of L_i at 1.6 cm 2 cm and 3 cm. Since initial length (L_i) affects the height of the arch, L_i was varied in order to determine its effect on the optical fibre critical radius.

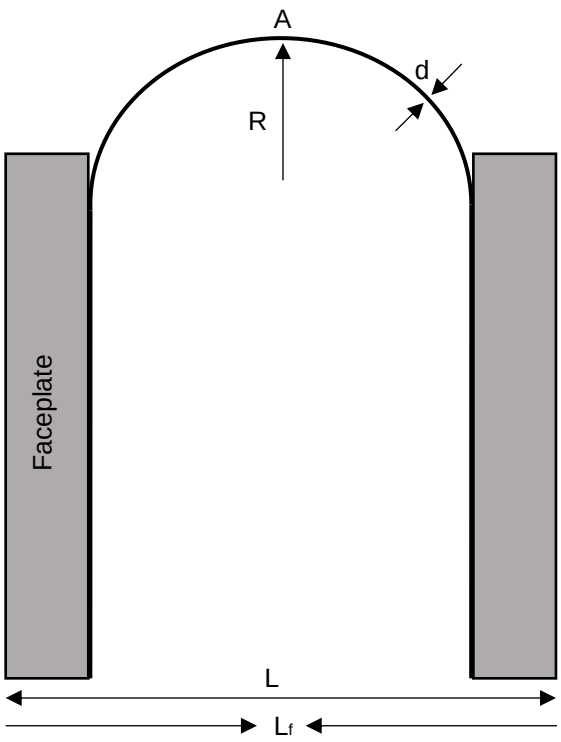

Figure 4-2: Two-point bending test set-up

The results obtained from the two-point bending test are given in Table 4-4. The failure stress and strain of optical fibres have been studied previously using the bending fracture test, which is an automated two-point or three-point bending test [42–44]. The failure stress obtained in the bending test in this project were a factor of 1000 lower than that found in literature [42]. This is possibly due to the differences in the strain rate, which is the velocity at which the face-plates are moved, the type of optical fibre used, type of bending test performed, uncertainties due to human error as well the conditions in which the experiments were performed [42–44].The starting distance L_i and hence the height of the arch did not seem to affect the calculated critical radii yielding an average deviation of only 0.26%. The average $\boldsymbol{L_f}$ obtained for each $\boldsymbol{L_i}$ investigated (1.6 cm, 2 cm, 3 cm) had a standard deviation of 3%, 5% and 3% respectively.

The highest critical radius of 0.29 cm and diameter of 0.58 cm from the obtained results was chosen as the critical bending radius and diameter in order to ensure the lowest probability of breakage during the operation of the process. For the design of the roller, a 100% contingency was added to the chosen critical diameter. Therefore, the diameter limitation for the design of the rollers was 1.15 cm. The roller design must be larger than 1.15 cm.

Table 4-4: Bending test results for roller diameter limitation

Average L_i (cm)	Average L_f (cm)	Average failure strain (mm/mm)	Average failure stress (N/m^2)	Average critical radius (cm)	Average critical diameter (cm)
1.6	0.68	0.21	23.11	0.28	0.57
2.0	0.69	0.21	22.81	0.29	0.58
3.0	0.69	0.21	22.53	0.29	0.58

A mechanical drawing of the final roller for the transportation of optical fibre through the process is given in Figure 4-3. The rollers are made of polytetrafluoroethylene (PTFE) more commonly known as Teflon. This is an ideal material since it has been reported to be non-sticking, chemically resistant and has a low coefficient of friction [59]. The rollers are used inside the vessels as well as between units as an optical fibre guide and are held upright with the help of a retort stand and clamp. This was required in order to easily adjust the roller height and configuration within the process.

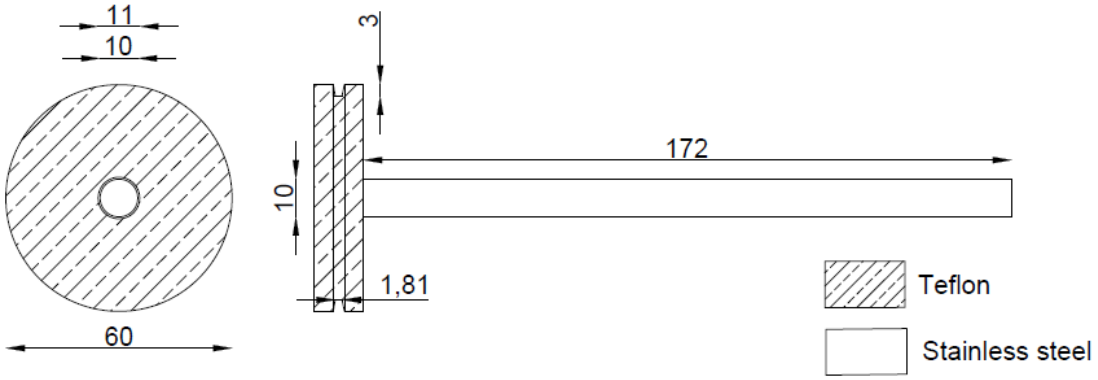

Figure 4-3: Mechanical drawing of rollers used for transportation in the process (dimensions in mm)

4.4.1. Design of Unit 1: raw material feed

This raw material to be used in the process is located in Unit 1. The main function of this unit is to hold the raw material so that it can be easily fed into the process. It is important that the design of the unit provides minimal tension to the fibre in order to reduce the likelihood of breakage, while still having enough friction to avoid the free flow of optical fibre into the process. The weight of the plastic optical fibre spool provides sufficient friction to avoid free flow. As seen in the technical drawings of Unit 1 (Figure 4-4 and Figure 4-5), a stainless steel pipe with Teflon® washers was used to reduce tension in the optical fibre line, since Teflon is a smooth low friction material [59]. Unit 1 has been designed to allow for easy replacement of raw material addressing design requirement (c).

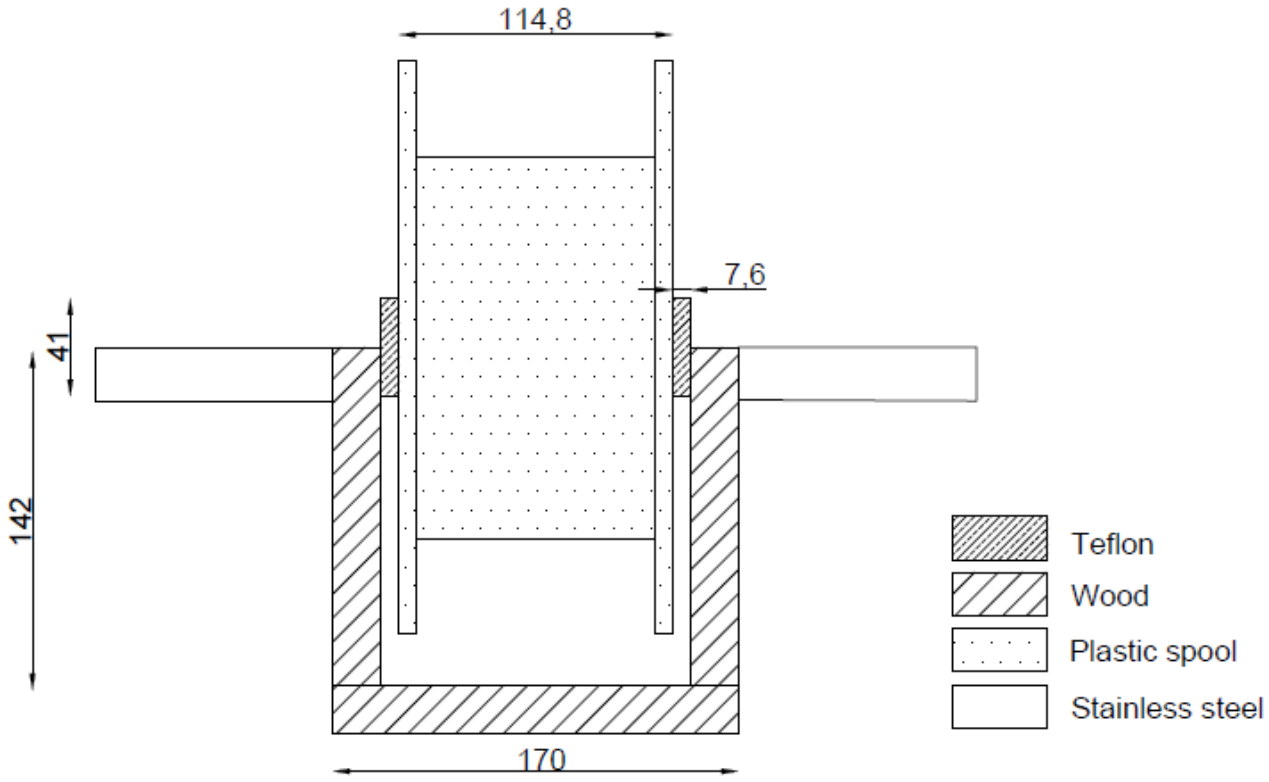

Figure 4-4: Mechanical drawing of Unit 1 - feed of optical fibre (side view; dimensions in mm)

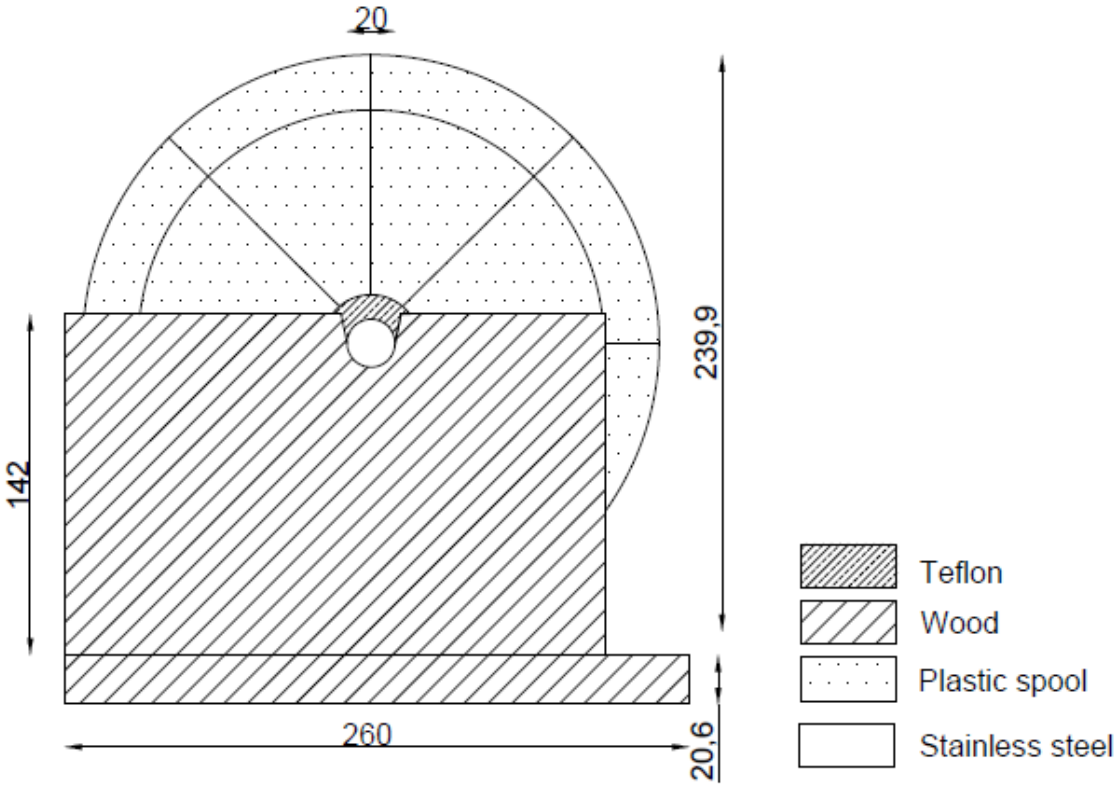

Figure 4-5: Mechanical drawing of Unit 1 - feed of optical fibre (front view; dimensions in mm)

4.4.2. Design of Unit 2: stripping

Optical fibre was fed from Unit 1 into Unit 2 where the buffer polymer coating was stripped from the optical fibre. Presently, there are 3 methods of stripping optical fibre, i.e. mechanical stripping [4, 39], stripping by heat treatment [1, 6], and chemical stripping [5, 36, 45, 57]. All three methods were considered for the proposed process.

The first method, mechanical stripping, involves stripping the optical fibre with a tool similar to a wire stripper. This method was successful to remove the buffer polymer coating from the optical fibre. However, this method does not lend itself easily for automation due to the fragile nature of optical fibre and their extremely small diameter.

Heat treatment in a temperature range of 400 – 500°C has been reported to successfully burn off the buffer polymer coating [1, 7, 20]. This test was repeated using thermogravimetric analysis (TGA) on the optical fibre. For this experiment, the optical fibre was heated in air to 250 °C with a ramp rate of 10 °C·min$^{-1,}$ held for 15 min before being heated to 350 °C at a heating rate of 10 °C·min^{-1} . The experiment was held at 350 °C for 15 minutes before being heated further to 450 °C at a heating rate of 10 °C·min^{-1} .The results from the TGA analysis can be seen in Figure 4-6. A total weight loss of 46.5% was obtained after heating the optical fibre up to 450 °C. It was determined visually that the polymer coating was not completely

burnt off as it formed a black rough layer around the fused silica optical fibre and would require additional steps to remove. This indicates that the stripping process was not completed, which is contrary to results obtained in literature which indicated that the polymer coated optical fibre with diameter ca. 225 µm was stripped down to a diameter of 112 µm, suggesting a completed stripping process [1, 7, 20]. Since the stripping process via heat treatment was incomplete it was not considered for the automated process since it would require extra steps which would ultimately make the automation more complex.

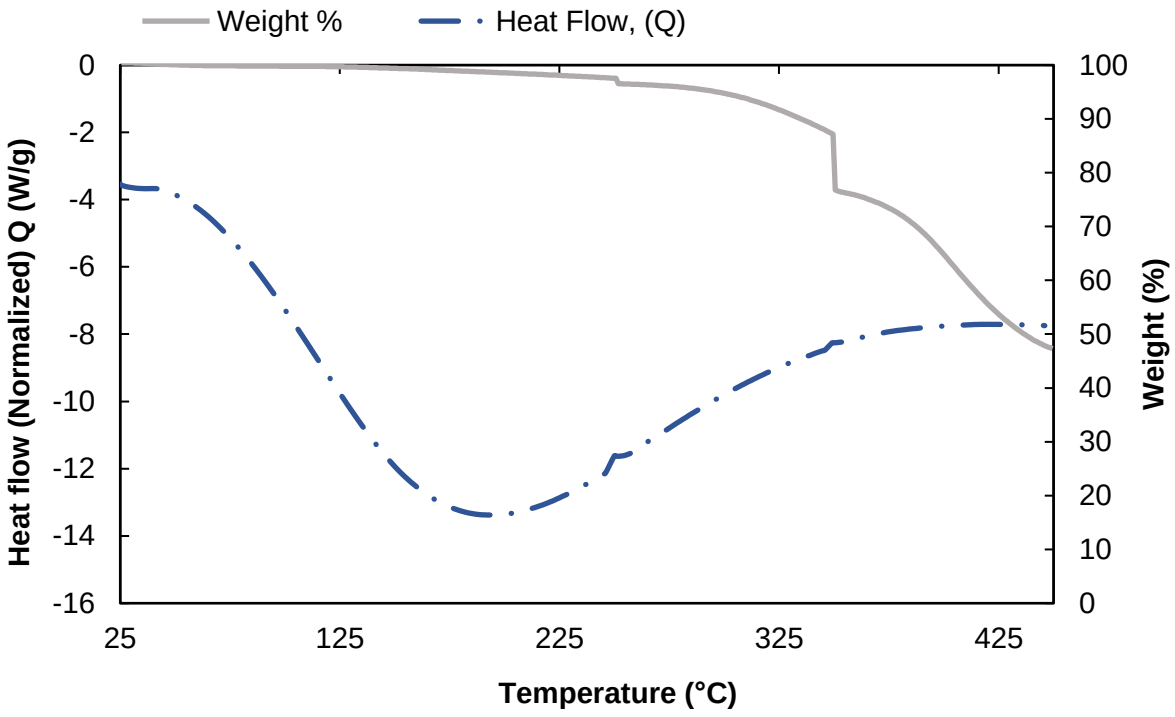

Figure 4-6: TGA analysis for polymer layer decomposition (heating in air at a constant ramp rate of 10 °C·min^{-1} ; 25 °C - 250 °C, 15 min hold, 250 °C - 350 °C , 15 min hold, 350 °C – 450 °C)

Striping via chemical methods has been reported to occur in either acetone or sulphuric acid [44, 60, 61]. For this process, acetone was chosen as it was deemed to be safer to incorporate into an automated process than sulphuric acid due to human operation and handling of the optical fibre in unit 2. The buffer polymer coating was completely stripped off from the fused silica optical fibre when submerged in acetone. However, it was noted that at room temperature the time taken to achieve complete stripping of the optical fibre was ca. 30 mins. This would imply that stripping of the buffer polymer coating becomes the limiting step in the overall process. For this reason, methods to reduce the stripping time were investigated. Pieces of polymer coated optical fibre were submersed in a beaker containing acetone (50 mL). The beaker was heated and stirred at 300 rpm using a heating plate. The time it took to remove the polymer coating from more than 75% of the optical fibre surface was recorded. Figure 4-7 demonstrates the relationship investigated between the so-determined stripping

time of the optical fibre and temperature of the acetone bath. The stripping process seems to follow an Arrhenius-type of expression implying that the stripping process seems to have an activation energy of ca. 70 kJ/mol. It is thus possible to speed-up the stripping process dramatically by increasing the temperature of the stripping process to ca. 50 ^{o}C. At this point, stripping will no longer be the rate limiting process in the overall process.

During this experiment, it was discovered that disturbing the coating layer using sandpaper (1 mm roughness) decreased the stripping time further. However, it is important to avoid damage to and breaking of the optical fibre during this roughening procedure. It was further noted that there some residual buffer polymer coating which remained loosely attached to the optical fibre, resulting in the need for a filter. A sponge was used as a filter to prevent any residual buffer polymer coating from exiting Unit 2 as the fibre is pulled through the process.

Therefore, from the three stripping methods, stripping by acetone was shown to be feasible as it is the most efficient and safest method to incorporate into the process design. It should be noted fresh acetone must be used to achieve consistent results. The solvent changes colour in the stripping process, possibly due to leaching of colourants and plastizer from the polymer into the solvent.

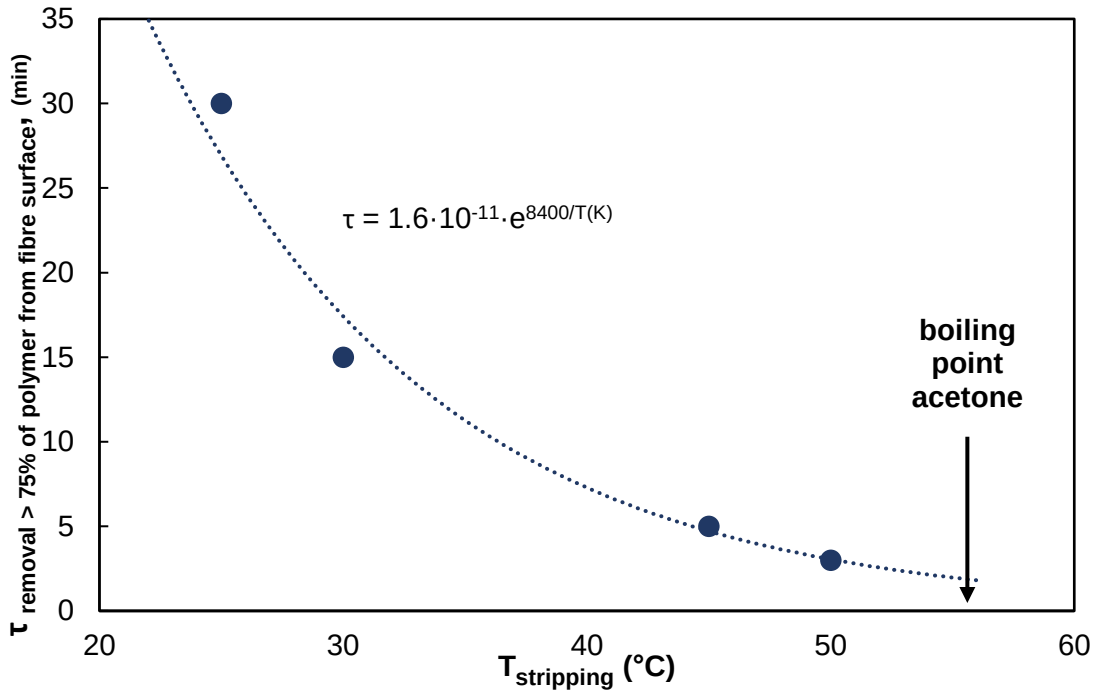

Figure 4-7: Relationship between the temperature of acetone bath (250ml) and stripping time to remove the buffer polymer coating from at least 75% of the fibre surface

Figure 4-8 and Figure 4-9 show the mechanical drawings of the two-roller system used in Unit 2 to strip the optical fibre from its buffer polymer coating. The optical fibre is drawn through a 5 L vessel containing acetone. A two-roller system was used to increase the residence time of the optical fibres in the acetone bath. Using a deeper vessel with more acetone could also be used to decrease the stripping time. The vessel is placed on a heating plate with magnetic stirring capabilities (Heidolph MR 3001K). The latter is required to ensure uniform heating in the acetone bath. A thermocouple placed in the acetone bath is used to control the temperature. This is the justification for design requirement (i) in Table 4-1. Acetone is flammable, it has explosion limits between 2 vol % - 12.8 vol % and has a low flash point (-17°C) with its auto-ignition temperature given as 465 ^{o}C. Hence, safety measures were put in place to minimise risks associated with having acetone at temperatures close to its boiling point. The stripping unit (Unit 2) is fitted with a lid that can be used to reduce evaporation, which is not shown in the mechanical drawing below. The heating plate is made explosion proof by securing all openings with aluminium foil. Furthermore, the whole process unit is placed in a walk-in fume hood to ensure continuous extraction of the excessive amounts of heated acetone.

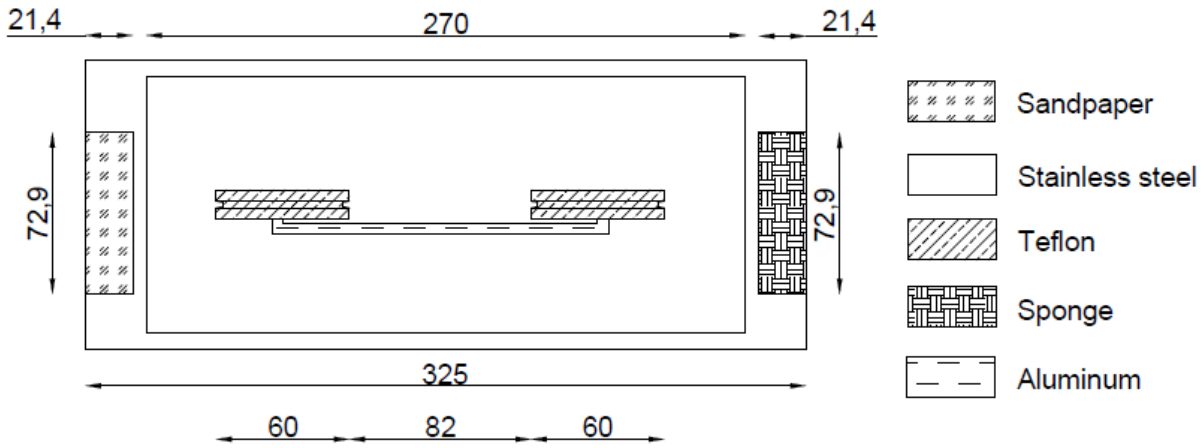

Figure 4-8: Mechanical drawing of Unit 2 – stripping unit (top view; dimensions in mm)

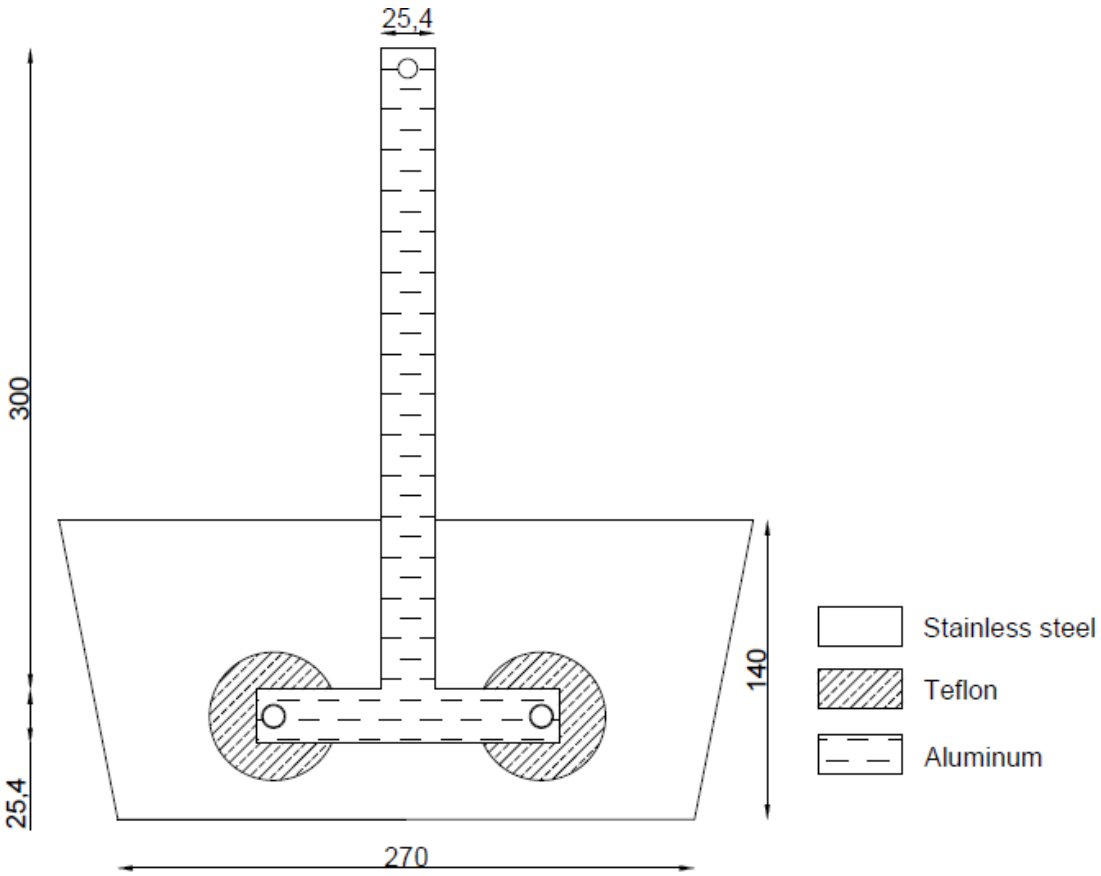

Figure 4-9: Mechanical drawing of Unit 2 – stripping unit (Cross-sectional front view; dimensions in mm)

4.4.3. Design of Unit 3: washing

Bare fused silica optical fibre after being stripped enters Unit 3. The main function of Unit 3 is to wash the optical fibre removing any residual organic substances from the fibre surface before the dip-coating process. Two methods of washing quartz optical fibre have been studied namely washing by the submersion of the bare optical fibre in deionised water (DI H_2O) or a 0.5 M sodium hydroxide solution, (NaOH) [5, 36, 45, 57]. These methods have been studied using thermal gravimetric analysis (TGA) of optical fibre that has been stripped and washed with either deionised water (Figure 4-10) or NaOH (Figure 4-11). The washed fibre was heated in air to 350 °C at a ramp rate of 10 °C·min^{-1} and the weight loss was determined. A similar weight loss was achieved using either washing medium (mass loss after washing with deionised water: 0.75%, mass loss after washing in an aqueous solution containing 0.5 M NaOH: 0.88%). From these results, it was concluded that either of the mediums can be used as a similar result was obtained. However, NaOH has been reported to have added benefits [62, 63] as it serves as a pre-treatment for the surface. This pre-treatment may result in enhanced hydrophilicity and an increase in the number of points for TiO_2 attachment. Therefore, NaOH solution has was chosen as the washing medium. Since NaOH may be

corrosive to certain metals and is harmful to humans, the appropriate personal protective equipment must be used at all times . Due to the nature of the design of this unit, the washing medium is easily interchangeable with another washing medium.

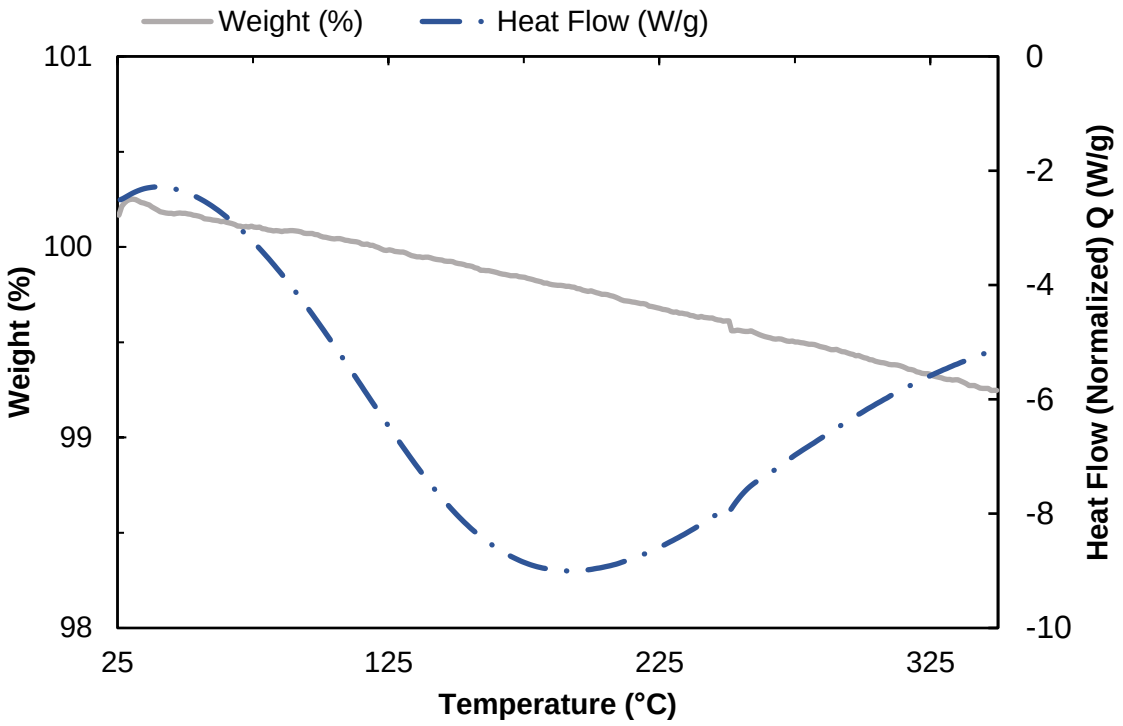

Figure 4-10: TGA analysis for optical fibre washed with de ionised H_2O (heated in air to 350 °C at a ramp rate of 10 °C·min^{-1})

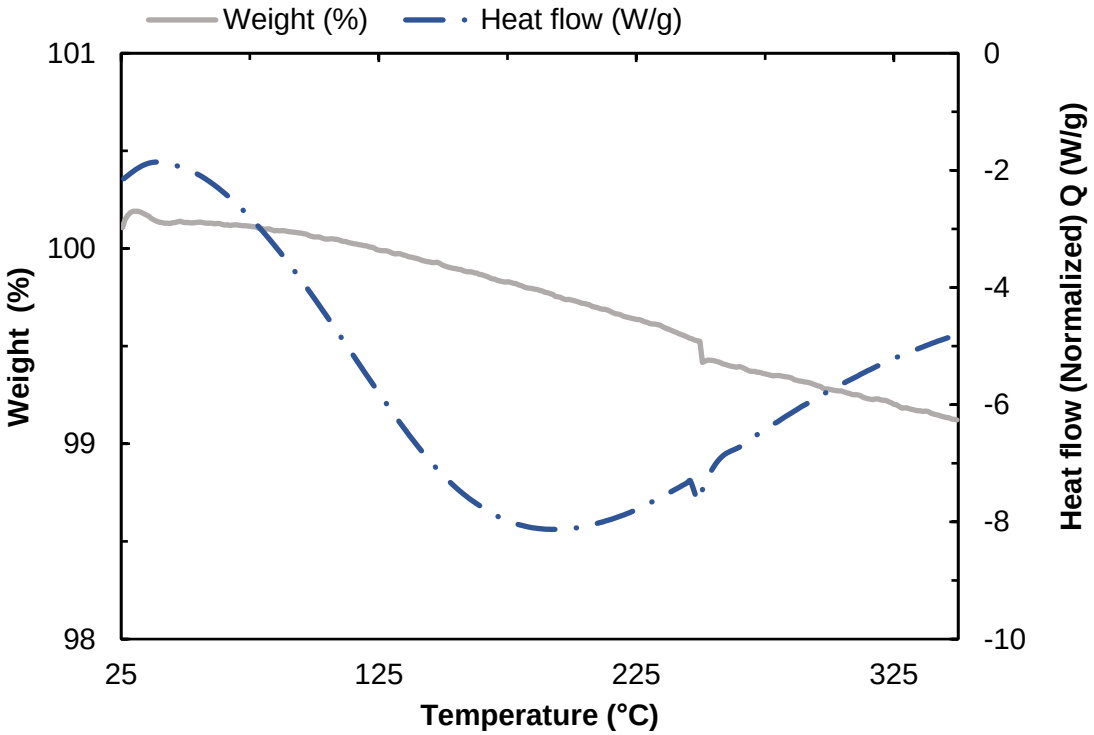

Figure 4-11: TGA analysis of optical fibre washed with a NaOH solution (heated in air to 350 °C at a ramp rate of 10 °C.min^{-1})

Since NaOH oxidises aluminium, the roller used in Unit 3 was mounted on a stainless-steel rod. Only one roller was used in order to reduce vessel diameter and the amount of washing medium used. A detailed mechanical drawing of Unit 3 which has a volume of 2.5 L can be seen in Figure 4-12. In order for complete submersion of the optical fibre, the vessel needs a minimum volume of 250 ml of NaOH solution.

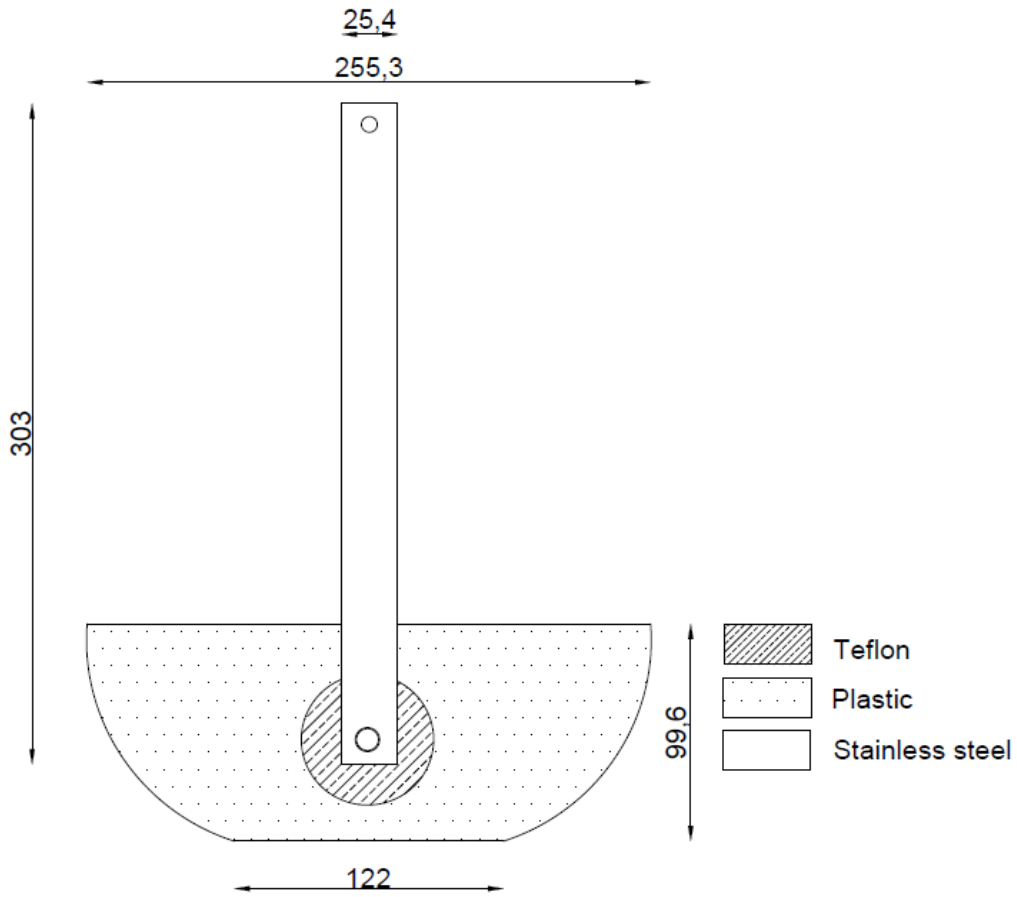

Figure 4-12: Mechanical drawing of Unit 3 – washing unit (cross-sectional front view; dimensions in mm)

4.4.4. Design of Unit 4: dip-coating

Unit 4 is where the stripped and washed optical fibre is coated via the dip-coating method with the desired photocatalyst. As previously mentioned, two types of coating mediums were investigated, namely slurry dip-coating and a sol-gel dip-coating mixture. The unit was designed so that the system can accommodate any catalyst, therefore according to design requirement (d), there is no limitation on the type of photocatalyst as long it can be suspended in a liquid. The slurry/gel needs to be constantly stirred to maintain a uniform concentration in the slurry/gel. This is achieved by using a magnetic stirrer (Heidolph MR 3001).

The dip-coating vessel has a narrow base and wide top (see Figure 4-13) to ensure that the catalyst coated optical fibre does not come into contact with the vessel walls and the heater in Unit 5 until it is completely dried, thus avoiding damage to the coating. Furthermore, the vessel shape minimizes of the amount of coating medium required. The volume of the vessel is 500 ml and in order for complete submersion of the optical fibre, the minimum volume of coating medium was 100 ml.

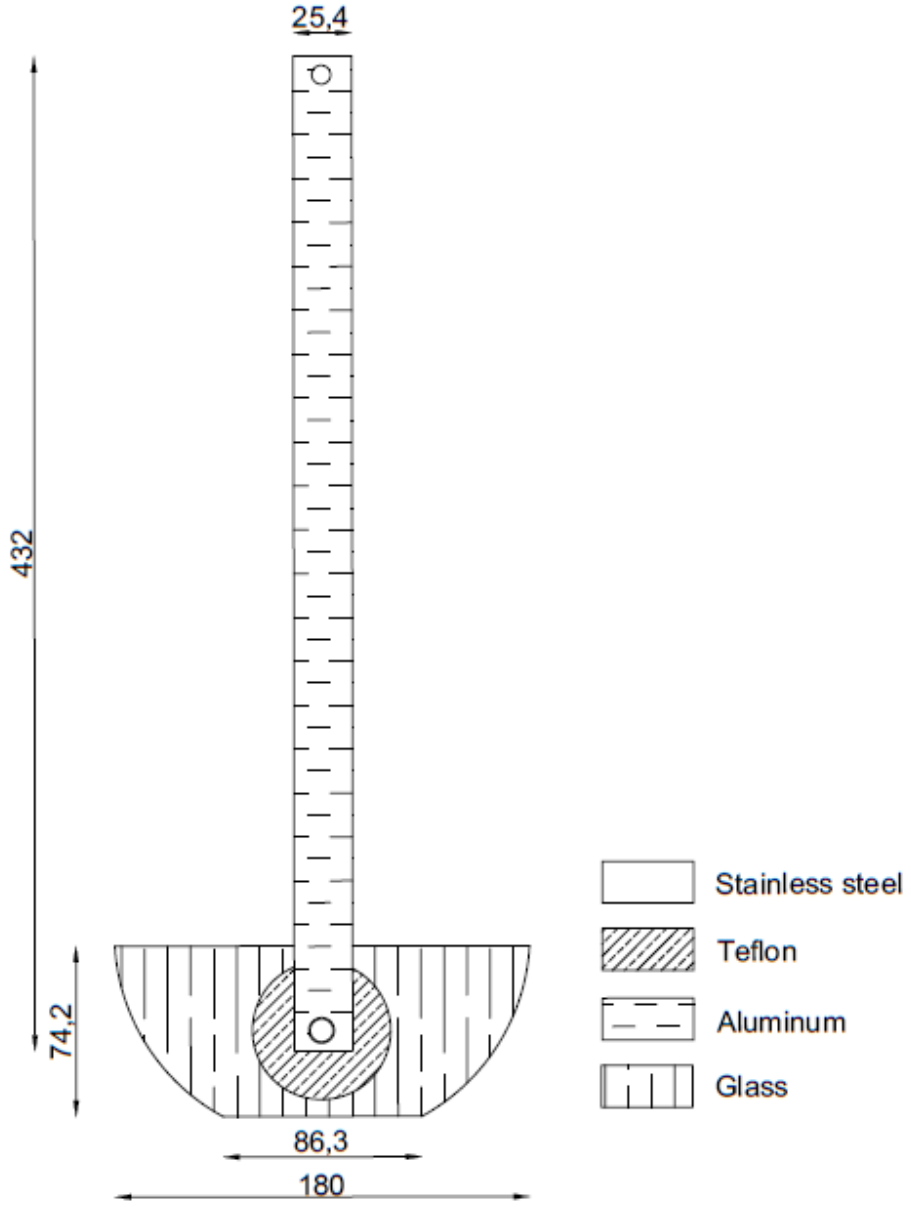

Figure 4-13: Mechanical drawing of Unit 4 – dip-coating process (Cross-sectional front view; dimensions in mm)

4.4.5. Design of Unit 5: heat treatment

Heat treatment of the coated fibre follows immediately after the optical fibre has passed through the dip-coating bath (Unit 4). There is no intermediate roller placed between Unit 4 and 5 to ensure no contact or damage to the coating. The oven was designed and built for this process in order to meet the design requirement (f). A technical drawing can be seen in Figure

4-14 and Figure 4-15. It is a two-part tubular oven; one half, which contains the heating elements, is fixed onto a stand and the other half is the door which latches the oven closed.

There are three sections within the oven that contain stainless steel shields which all have different functions. The protective shields on the outer edge of the heating elements prevent damage to the glass heating elements. The inner edge of the heating elements each contains a rectangular metal shield which creates a pathway in the centre of the oven for the thermowell as well as the moving coated optical fibre. The purpose of this shield to maintain a constant temperature in the pathway. The optical fibre has a very low thermal mass; therefore, it is assumed that the fibre may feel the fluctuations in temperature from the pulsing heating elements. Hence, it is important to maintain the temperature that the optical fibre experiences. The third area is the back plates of the heater which separates the insulation, which is packed on either side of the oven, from the inner components of the oven.

The specifications of the oven are given in Table 4-4. Quartz halogen infrared heating elements were used as they provide precision-controlled, fast response heating. Two heating elements which are rated for 1000 W were connected in parallel. In order to prevent a build-up of static air, an air inlet is installed on the optical fibre inlet side of the oven. This allows a small flow of air through the heater. The air exits with the optical fibre.

Table 4-4: Specifications for Unit 5 – heat treatment

Specification	Type
Heating element	Quartz Halogen Infrared
Thermocouple	J Type
Air inlet flowrate ($ml \cdot min^{-1}$)	30
Operating temperature range (°C)	200 - 600
Temperature controller	Gefran 600 (Output = 100%, P = 0.1, I = 0.04, D = 0.01)

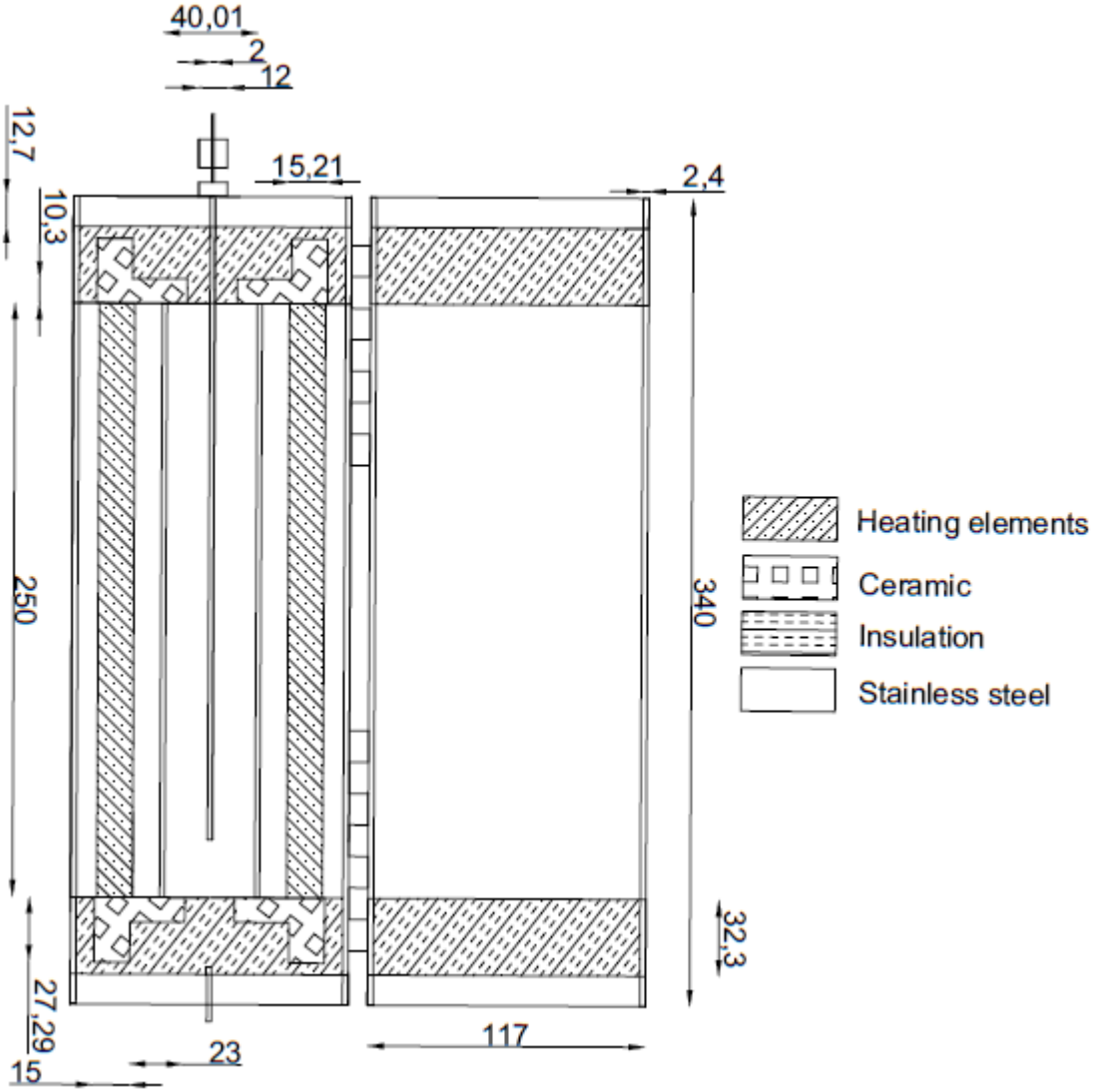

Figure 4-14: Mechanical drawing of Unit 5 – heat treatment (front cross-sectional view; dimensions in mm)

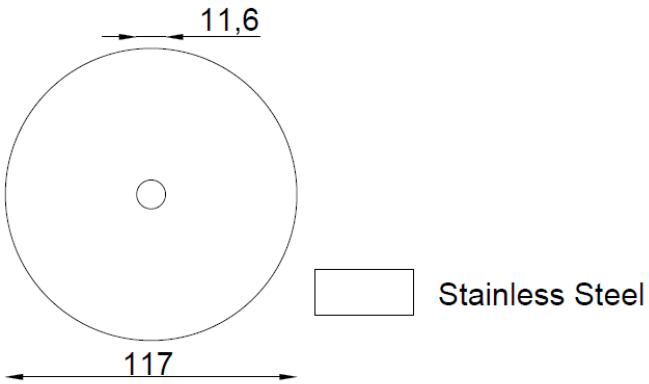

Figure 4-15: Mechanical drawing of Unit 5 – heat treatment (Side view; dimensions in mm)

Temperature calibration was done for the oven for the operating temperature range of 200 °C - 600 °C (see Figure 4-16). The controlling thermocouple of the heat treatment unit is placed ca. 9 cm from the inlet temperature. It can be seen that the thermocouple is reading the set-point temperature at approximately 9 cm from the reactor inlet. The presence of multiple shields, the air inlet and the distance between the centre pathway and the heating elements will preclude a homogenous temperature along the path of the moving optical fibre. The inlet side of the oven is the coolest part of the oven as a consequence of the air flowing through the heat treatment unit. The temperature reaches a maximum towards the middle of the oven. The temperature decreases towards the end of the oven as it is open to the surroundings.

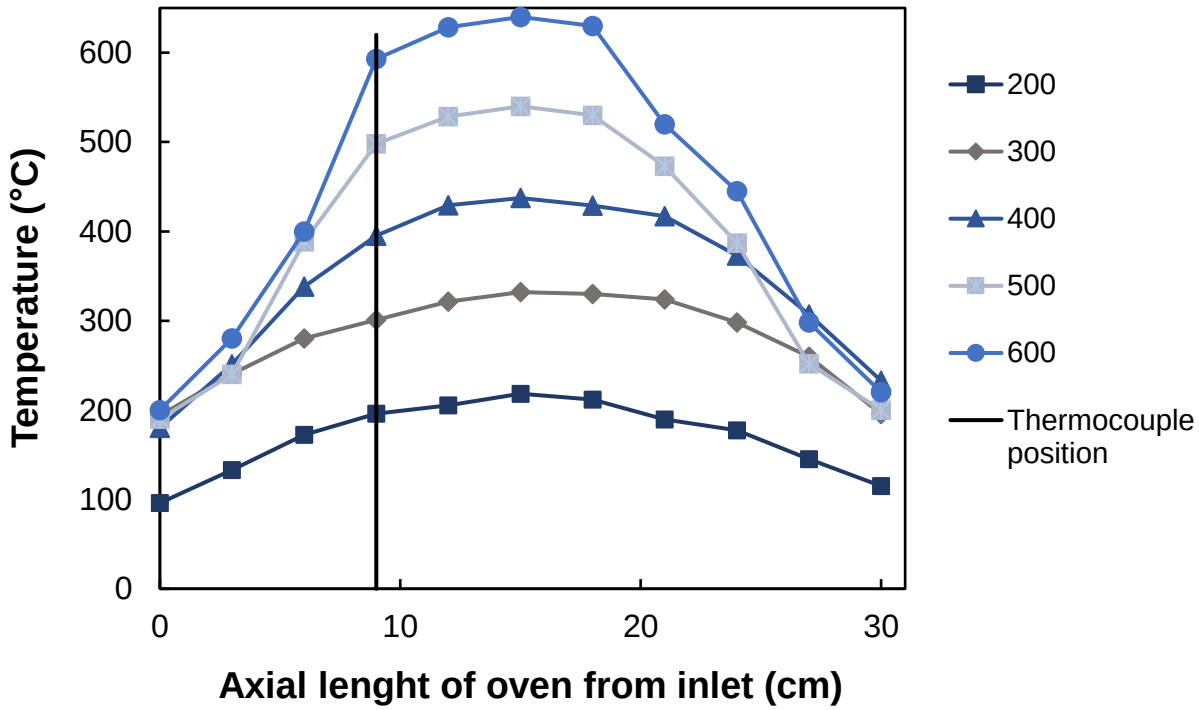

Figure 4-16: Temperature profile in the heat treatment unit along the pathway of the optical fibre

4.4.6. Design of Unit 6: collection/pulling

Lastly, after the coated optical fibre is dried, it is directed by the last roller to Unit 6, where the coated fibre product is collected on a spool. Unit 6 is also responsible for controlling the speed at which the fibre is pulled through the process. The collection spool is connected to a motor and a control box which is used to precisely control the speed of the rotating motor and hence the speed at which fibre moves through the system. A gear system was required in order to reduce the speed to those specified in literature, as they cannot be achieved by the stepper motor [6,55]. The gear system gears down the rotational speed of the motor by a factor of 10 to obtain a slowly rotating spool. The mechanical drawings for Unit 6 can be found in Figure 4-17 and Figure 4-18. Table 4-5 provides more information on the set-up and operation of Unit 6. The code used for speed control can be found in Appendix D.1.

Table 4-5: Specifications for Unit 6

Specification	Type
Motor type	Stepper motor
Motor control board	Arduino Mega2560
Software	Arduino IDE
Power supply	12 V
Code	Appendix D.1.

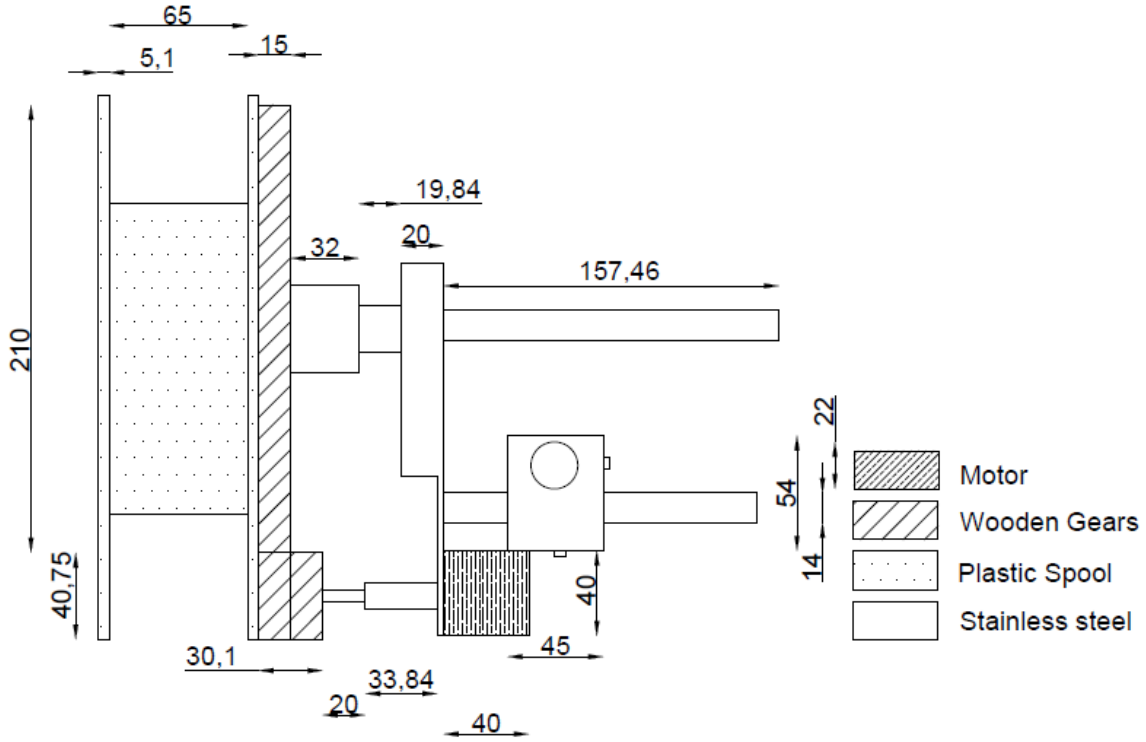

Figure 4-17: Mechanical drawing of Unit 6 – collection/pulling (front view cross-section; dimensions in mm)

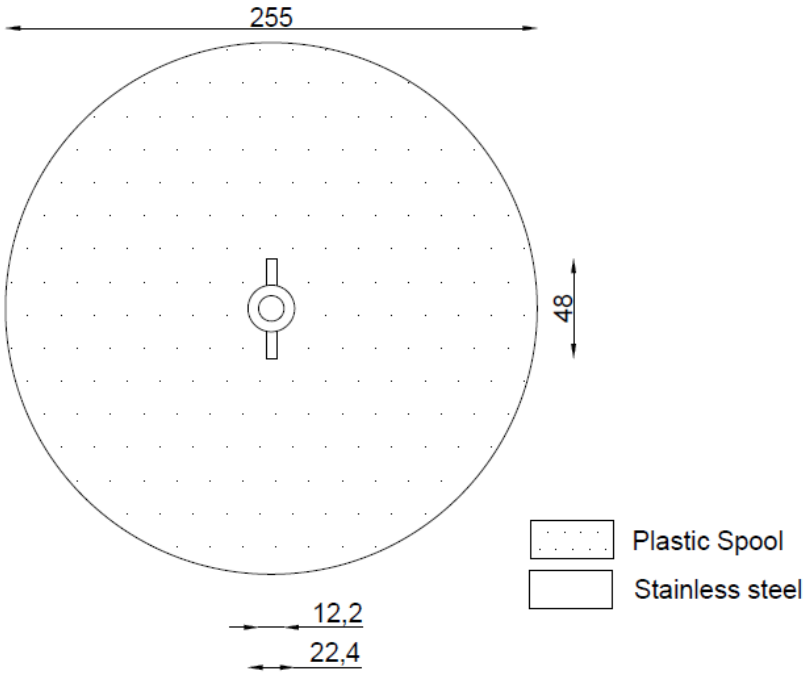

Figure 4-18: Mechanical drawing of Unit 6 – collection/pulling (Front view; dimensions in mm)

4.5. Overall system layout and safety

As detailed above, each unit is explicitly designed and built to meet specific requirements which work together to meet the overall process objective. The overall process consisting of all 6 process units and auxiliary components is shown in Figure 4-19 and Figure 4-20. In accordance with design requirements (a) and (e), the use of this process is automated and can be easily manipulated of the specific control variables. The units are easily movable, and rollers can be adjusted on the retort stand to adapt the process configuration.

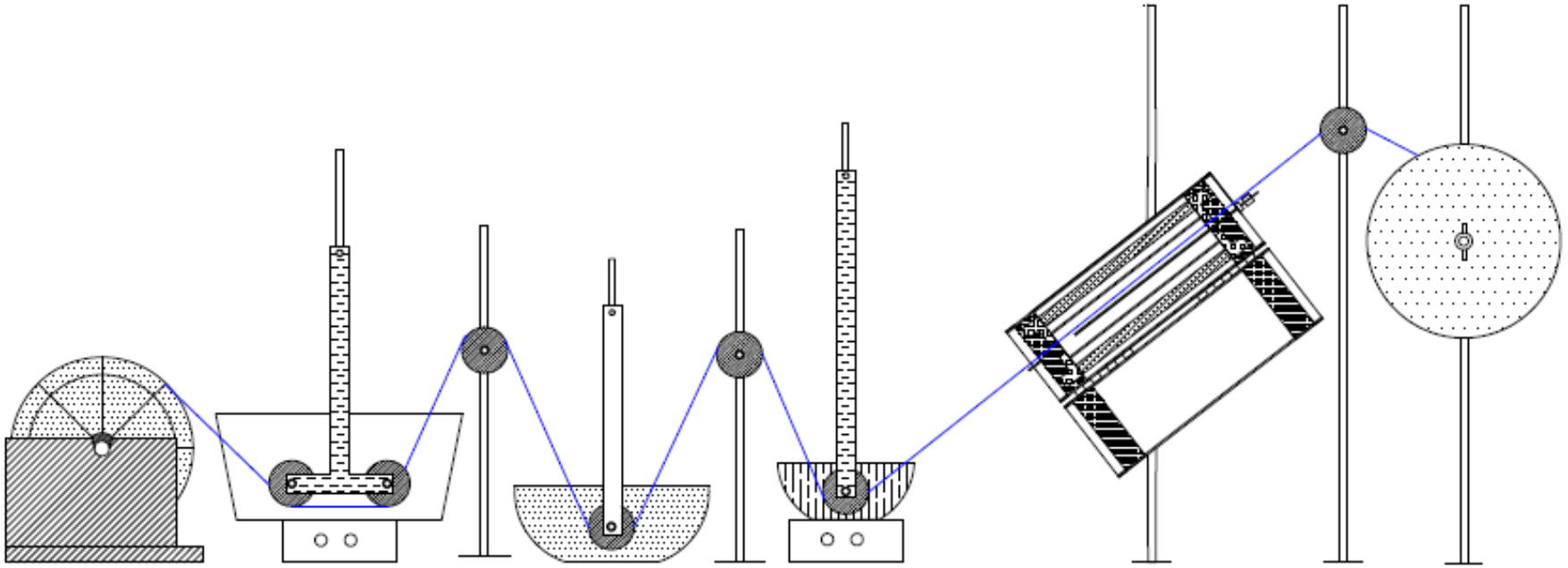

Figure 4-19: Cross-sectional front view of the overall system

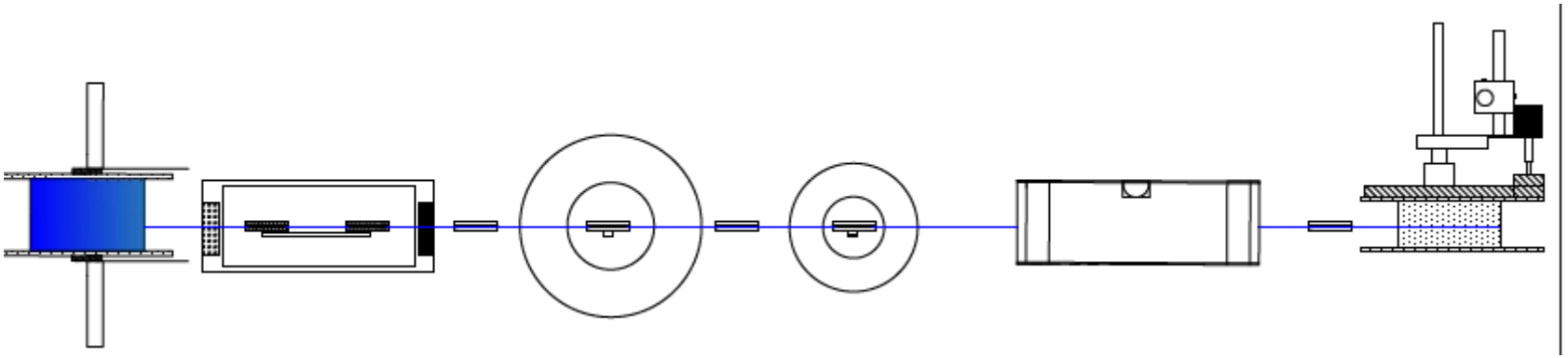

Figure 4-20: Top view of the overall system

The use of acetone at temperatures close to its boiling point (54°C), requires the operation of the whole process in an extraction environment. Hence, the process is located in a 4 x 3 m walk-in fumed hood. Figure 4-21 shows the layout and floor plan for the process. There are two main exits from the fume hood which are easily accessible and there are sliding doors along both sides of the fume hood represented by the dashed line in Figure 4-21. A workspace is allocated for easy access and control of the process. There are two emergency shutdowns switches, one inside the fume hood, and another outside the fume hood. A fire blanket and a fire extinguisher located within 10 m of the fume hood.

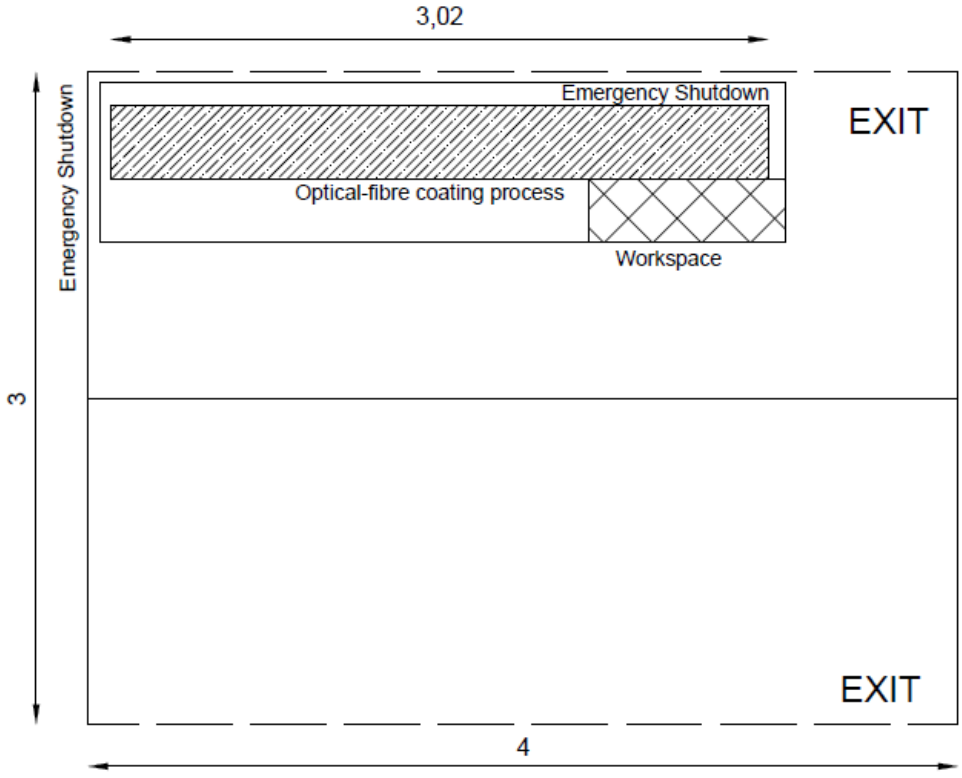

Figure 4-21: Floor plan layout of the walk-in fume hood containing the process

5. Methodology

The following chapter will outline the methodologies used in this project in three major sections namely, preparation of the slurry/gel containing the catalyst, the automated optical fibre catalyst coating process and the preparation for optical fibre coating characterisation.

5.1. Catalyst synthesis

5.1.1. Preparation of P25-slurry

The catalyst slurry was a suspension of P25 (TiO_2; Evonik) in deionised water. A buffer solution was used to maintain a constant pH of the slurry (see Table 5-1). The buffer solution comprised of a mixture of acetic acid and ammonium acetate. The boiling points of acetic acid and ammonium acetate are 118 °C and 117 °C respectively. Therefore, during the heat treatment in Unit 5 (typically larger than 200 °C), both the compounds in the buffer solution and water are evaporated, which should result in a layer of pure P25, TiO_2, on the outer surface of the optical fibre.

A slurry volume of 300 ml was required for each experiment to obtain sufficient submersion of the roller and hence the optical fibre, The investigated process variables for the dip-coating on P25 on the optical fibre are pulling speed (residence time), solid content of slurry, pH of the slurry and drying temperature during the final heat treatment (see Table 5-1). Standard conditions (shown in **bold** in Table 5-1). were chosen for each variable in order to maintain consistency within the different variable ranges which were tested. This allows for an accurate representation of the impact the tested process variable has on the catalyst coating thickness and coverage. Each run was repeated 3 times in order to ensure repeatability of results.

Table 5-1: Process variable ranges investigated for dip-coating optical fibre with a P25 slurry

Process Variable	Range Tested
Pulling speed ($mm \cdot s^{-1}$)	0.12, 0.58, **1.15**, 1.73, 2.30, 2.88, 3.46, 4.03, 5.76
Solid content (wt.-%)	1, **5** ,10, 15, 20
pH of the slurry[1]	2.65, 3.65, **4.65**, 5.65
Drying temperature (°C)	**200**, 300, 400, 500

[1] pH controlled by changing the relative amounts of acetic acid and ammonium acetate in the slurry

5.1.2. Sol-gel suspension preparation

The sol-gel method was used to prepare a TiO_2, anatase layer using the method described by Akpan and Hameed [64]. Two solutions were made in separate beakers namely solution A and solution B. Solution A was prepared by mixing 35 ml of ethanol (absolute 99.9% pure), 15 ml of deionised water and 3 ml of nitric acid. Solution B was prepared by mixing 40 ml of ethanol and 17 ml titanium (IV) butoxide ($Ti(OBu)_4$) in a completely dry beaker, since ($Ti(OBu)_4$) is susceptible to precipitation when in contact with water. Solution A was mixed at a constant speed of 175 rpm on a magnetic stirrer. Solution B was added to Solution A in a drop-wise manner. The combined mixture was subjected to sonicated for 30 minutes to ensure a homogenous mixture. The sonicated mixture was further stirred for 8 hours before being used in the fibre coating process.

The process variables investigated in the dip-coating method using the gel prepared via the sol-gel method are given in Table 5-2 below with the standard conditioned shown in **bold**.

Table 5-2: Process variable ranges investigated in the dip-coating process using a gel prepared using the sol-gel method

Process Variable	Range Tested
Pulling speed ($mm.s^{-1}$)	0.12, 0.58, **1.15**, 1.73, 2.30, 2.88, 3.46, 4.03, 5.76
Drying temperature (°C)	400, **500**, 600

5.2. Automated optical fibre catalyst coating process (AOFCCP)

The automated optical fibre catalyst coating process (AOFCCP) that was designed and constructed as per section 4. The system shown by Figure 5-1 was commissioned using two coating methods as described above and as stipulated by design requirement d, the catalyst medium in the process must be easily interchangeable.

The standard operating procedure for the AOFCCP is split into two sections, the start-up procedure which outlines the steps required to start the process and allow it to reach operational steady-state. Where the steady-state of the process is defined as the continuous coating of the optical fibre at a particular speed with all units successfully performing its function. The second section is the shutdown procedure which outlines the necessary steps required to safely shut down the process form the operational steady-state function.

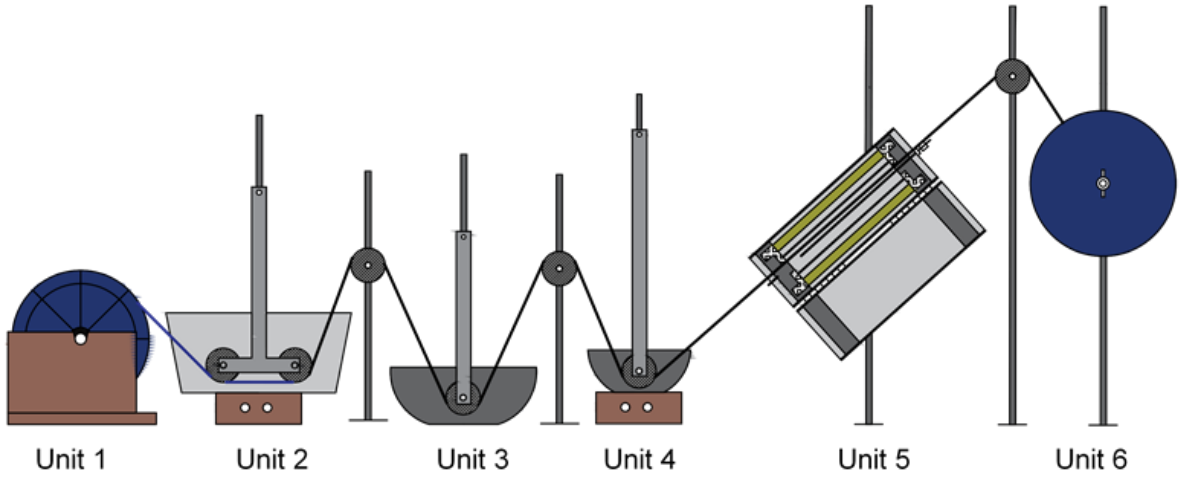

Figure 5-1:Experimental set-up of the AOFCCP drawn to scale

5.2.1. Start-up procedure

The following procedure was followed to start-up the coating process

The optical fibre needs to be threaded through the whole set-up from the feeding unit (Unit 1) through all rollers in each unit through to Unit 6. All rollers must be properly aligned so that the optical fibre can move from Unit 4 through Unit 5 and onto Unit 6 without contacting any surface thus attempting to minimise damage to the coating prior to the drying stage. The end of the optical fibre has to adhere to the collection spool in Unit 6 with adhesive tape.

The vessel in the stripping unit (Unit 2) need to be filled with approximately 800 ml of acetone (99% pure). The temperature of this unit will be set to 45 °C and the mixing speed of the magnetic stirrer to 600 rpm. After the acetone bath has reached the set-point temperature ensuring the optical fibre is completely submerged in the bath and is beginning to strip. Remove the access polymer coating if required before the process can begin pulling. The vessel in the washing unit, Unit 3, will be filled with 250 ml of an aqueous solution of sodium hydroxide (0.5 M). In the dip-coating unit, Unit 4, 100 ml or 300 ml of gel or slurry will be placed in the vessel. The slurry/gel will be stirred using a magnetic stirrer set to 400 rpm.

The process is started by setting the desired speed on the controller (Arduino software) and power up the motor. Monitir the bare fibre end as it moves through the process. The stepper motor is switched OFF once the bare fibre end exits the washing unit, i.e. Unit 3. The furnace for the heat treatment (Unit 5) is switched ON the heater at unit 5 and set to the desired temperature. Once the furnace has reached the desired temperature, the fibre is pulled

through the process by switching ON the motor. This will allow the bare fibre to pass through the slurry/gel containing the catalyst at the desired speed. The catalyst coated optical fibre is collected on the collection spool on Unit 6. Once all units are operational and 1 m of optical fibre is coated and collected the system is assumed to be at operational steady-state.

5.2.2. Shut-down procedure

The procedure below describes in detail the steps required for safe process shutdown and product collection.

Once the desired quantity of the product has been collected, then the system can be shut down. The power to the motor must be switched off to stop the movement of the optical fibre through the process. The heaters and mixers in Unit 2, 4 and 5 respectively must be switched OFF. The coated optical fibre line can be cut immediately after the heat treatment, Unit 5, and the product can be collected.

5.3. Characterisation of coated optical fibre

In order to determine the thickness of the catalyst coating and the coverage of the fibre by the coating, the coated fibre was characterised using scanning electron microscopy (SEM). Raman spectroscopy was used to confirm the formation of TiO_2 and identify the crystal phase.

5.3.1. SEM preparation for evaluation of surface coverage

The coverage of the coated optical fibre was viewed using SEM. At least 10 pieces of the collect product were chosen at random and placed onto a stub covered in carbon tape. Tweezers were used in order to reduced damage to the coating caused by handling. Carbon glue was not used as it causes smudges on the optical fibre coating which leads to poor coating visibility. It should be noted that the ends of the sample should be avoided as it is prone to be damaged by handling. The stubs were labelled and coated in carbon for 30 minutes using a *Blazers evaporation coater* before SEM was done in order to determine the extent of coverage. An example of the prepared sample is shown in Figure 5-2.

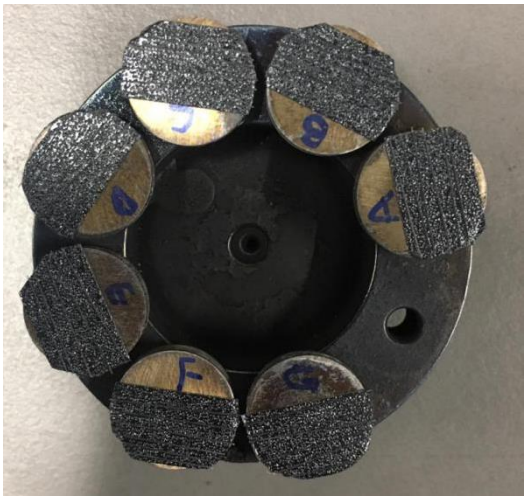

Figure 5-2: Coated optical fibre prepared on the stub for SEM

5.3.2. SEM preparation for evaluation of coating thickness

In order to provide the most accurate measurement of the thickness of the coating, the measurement must be taken over the cross-section of the fibre. This can be done by using Spurr's resin which is commonly used in electron microscopy, allows for the optical fibre to stand vertically. At least 10 different pieces of fibre from a sample was placed in an Eppendorf tube® . It is important that the fibre ends reach the bottom of the Eppendorf tube® . Since not all fibre pieces reach the bottom of the Eppendorf tube® using as much fibre as possible should be used. Half of the Eppendorf tube® was filled with resin whilst ensuring minimal disturbance to the sample then dried for 24 hours at 60 °C (see Figure 5-3)

The preparation of the resin for SEM comprises 3 steps; sanding, polishing, sonication, drying and coating. The tip of coated fibre glass in the Eppendorf tube® was cut with a blade and the hardened resin cone was pushed out. The tip of the resin was sanded using electro-coated silicon carbide waterproof sanding paper, grit 800, until at least 5 fibre ends were exposed. Sanding was used to control the height of the resin cone. It is important to note that the resin cone tip must be as flat as possible, and the resin height must be constant for all the samples to ensure consistent picture quality for all samples since the working distance between the sample surface and the beam remains constant for all samples in the microscope.

The flattened resin cone tip was polished using alumina polishing powder and water in order to improve visibility of the exposure fibre ends on the surface. Polished resin cones were sonicated in deionised water for 30 minutes in order to remove residual alumina powder that may remain on the surface. The exposed surface was dried using compressed air, then stuck onto a stub for coating using a combination of carbon and glue. Energy-dispersive X-ray spectroscopy (EDS) was used to identify alumina particles when required since residual alumina powder may remain on the exposed resin surface from the polishing process which

may lead to a false coating thickness on certain areas of the fibre cross-section . An example of the prepared resin sample is shown in Figure 5-4.

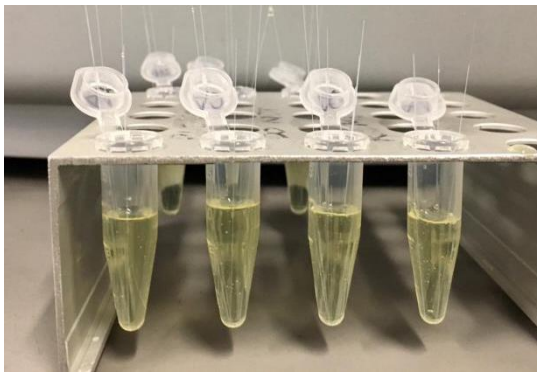

Figure 5-3: Coated optical fibre vertically in Eppendorf tube®

Figure 5-4: Resin cone showing exposed flat surface

5.3.3. SEM analysis

The SEM analysis performed in this study was done using the Thermo Fisher NovaNano SEM 230 and Tescan MIRA3 SEM. The NovaNano SEM is equipped with a field emission gun which allows for high emission SEM images as well as an Oxford EDX system which was used when needed to distinguish between the TiO_2 layer and the alumina polishing powder. Surface morphology of the coated optical fibre was studied by taking SEM images with magnifications 500X, 1000X and 1500X using either microscope operated at 5 keV. The coating layer thickness measurements were taken using either microscope operated at 20 eV. Detailed specifications used can be found on the information bar of the SEM images.

5.3.4. Raman analysis

Sample preparation for Raman was identical to that used in section 5.3.1 however these samples were not be coated in carbon. The Witec confocal Raman microscope (alpha 300) was used to perform the mapping on the optical fibre coating layer. The Raman maps were taken using a 50X objective. The large-scale image scan was taken using 150 points per line for a scan width of 50 µm and 60 lines per image for a 15 µm scan depth from the coating layer into the optical fibre.

6. Results

This chapter will outline the results obtained from the commissioning of the automated optical fibre catalyst coating process (AOFCCP). Experiments were performed to demonstrate the production of optical fibre coated with a catalyst layer of variable thickness using an automated optical fibre catalyst coating system.

6.1. Uncertainty in results

Dip-coating by hand creates uncertainties which can be avoided with the use of an automated system. The angle of immersion and emergence, as well as the withdrawal speed cannot be precisely controlled in manual dip-coating since there exist uncertainties due to human error. Therefore, an automated dip-coating system is essential to minimise these uncertainties.

The slurry concentrations and pH were kept constant in order to prevent uncertainty due to the extent of suspension homogeneity and optical fibre coating surface homogeneity. There are uncertainties surrounding characterisation and dip-coating that may lead to subsequent uncertainty in the results observed in these experiments. For dip-coating, the standing time of the catalyst containing slurry/gel between changes in the process variables may lead to possible uncertainty of the results. This uncertainty was minimised by making a new batch of catalyst per day. Since a process variable range was repeated 3 times (See Table 5-1), the order of the conditions in the range was reversed to further ensure the uncertainty of solution standing time is minimised.

Uncertainty surrounding the characterisation of optical fibres under SEM relates to the availability of a measurable thickness which depends on the sanding and polishing process. The coating on the cross-section may be damaged by the sanding process, and the alumina polishing powder from the polishing process may remain on the exposed cross-section. The portion of measurable thicknesses taken from that sample is assumed to represent the coating across the various optical fibre belonging to a constant variable that was being analysed. The linear speed of the optical fibre moving through the system will vary as the optical fibre accumulates on the spool due to the increase of the spool circumference, but for this project, this can be neglected due to the very small diameter of the optical fibre and the small amount of coated optical fibre collected for each run.

6.2. Analysis of coating uniformity, repeatability and significance

The extent of the repeatability of the product obtained from the automated optical fibre catalyst coating process (AOFCCP) was studied by determining the standard deviation in the results obtained in the repeated experiments. The coating thickness is typically small (< 1µm) and as a result, small deviations may result in a large standard deviation across the sample set. Therefore, assumptions were made for standard deviation limits in order to evaluate the precision and uniformity, repeatability and significance of the results obtained. Table 6-2, below, outlines the assumptions made and the results can be found in Appendix A.1.

Table 6-1: Assumptions made for the statistical analysis of the results

Standard deviation Test	Description
Precision & Uniformity	A set of results obtained from a single run is assumed to be precise and the coating thickness is regarded as uniform if the standard deviation is equal to or less than 30%.
Repeatability	The results of experiments which are repeated 3 times (a subset) were assumed to be repeatable if the standard deviation of the average thickness of each experiment in the set is below 10 %.
Significance	The relationship between the tested variable and the accumulated average coating thicknesses obtained for each set in the range test is assumed to be insignificant if the standard deviation is below 2%.

The precision in the results obtained per run for the experiments performed for all process variables and in all subsets was below 30% except for the pulling speed experiments with a high pulling speed of 2.9 $mm.s^{-1}$ and 3.5 $mm{\cdot}s^{-1}$ through the gel. This indicates that, based on the chosen assumptions, all the experiments besides the sol-gel experiments at fast pulling speeds produce precise results and uniform coating thicknesses.

As seen in Appendix A.1. all the experiments performed per subset for all variables had a standard deviation of less than 10%, indicating that the results obtained are reproducible. This standard deviation is shown as error bars on graphs. The last test was used to determine if the variable had any significant effect on average coating thickness on the optical fibre. All process variables, except for pH, that were investigated had a deviation of above 2% indicating that the process variable can be used to manipulate the coating thickness in the AOFCCP. The standard deviation of the results obtained from the pH range investigated was below 2%

which indicates that the pH of the P25 slurry had no significant effect on the average coating thickness on the optical fibre.

6.3. Observation analysis of coating morphology

The surface morphology of the TiO_2 coating was assessed from SEM images. The conclusions made regarding the extent of surface coverage and homogeneity of the coating was based on observation. Therefore, various terms used to describe the observations are define and illustrate the following section.

6.3.1. Degree of surface coverage

The degree of surface coverage of the coating is assessed by the areas of the optical fibre which are not covered by TiO_2 particles. SEM images are black and white; therefore, the extent of the coverage was also evaluated by the grey scale of the coating. The optical fibre is seen as a dark grey as demonstrated by the image of the bare optical fibre (see Figure 6-1 and Figure 6-2). Once the coating is adsorbed onto the optical fibre, the grey surface is covered with white TiO_2 particles. It is assumed that the areas on the optical fibre that appears brighter have a thicker coating.

The extent of the coverage of the surface with coating compared to the bare optical fibre has been classified as low, moderate, high surface coverage. High coverage of the surface is defined as the complete coverage of the optical fibre. Moderate coverage of the optical fibre is a coating which consists of minimal areas of the optical fibre having little to no TiO_2 particles. Lastly, a low surface coverage is defined as the coverage of less than half of the observed optical fibre surface. The appearance of the coating differs for the two different coating methods used in this study. Coating using a slurry of P25 has a brighter contrast on the SEM-image (see Figure 6.1). At high coverage, the coating appears rather smooth (b), but at moderate coverage and in particular low coverage, islands with no TiO_2 particles can be observed on the surface of the optical fibre (c & d). The surface roughness obtained was similar to that achieved in literature , it can be seen that the surface appears to be corrugated and is uneven [1,2]. The surface of the optical fibre coated with titania obtained from the sol-gel process appears to be light grey in colour (see Figure 6.2). At high coverage, the coating appears to be smooth and skin-like which is in agreement with results obtained in literature [67] . The coverage catalyst layer which is formed via sol-gel coating is strongly linked to the extent of the cracking and deformations. Unlike coating using P25 , there are no islands of TiO_2 particles on the surface. A smooth, high coverage optical fibre can be seen in (b) whereas , in (c) the appearance of cracking occurs which is regarded as moderate coverage. Low

coverage is seen by (d) , which show cracking with more than half of the catalyst layer peeled off.

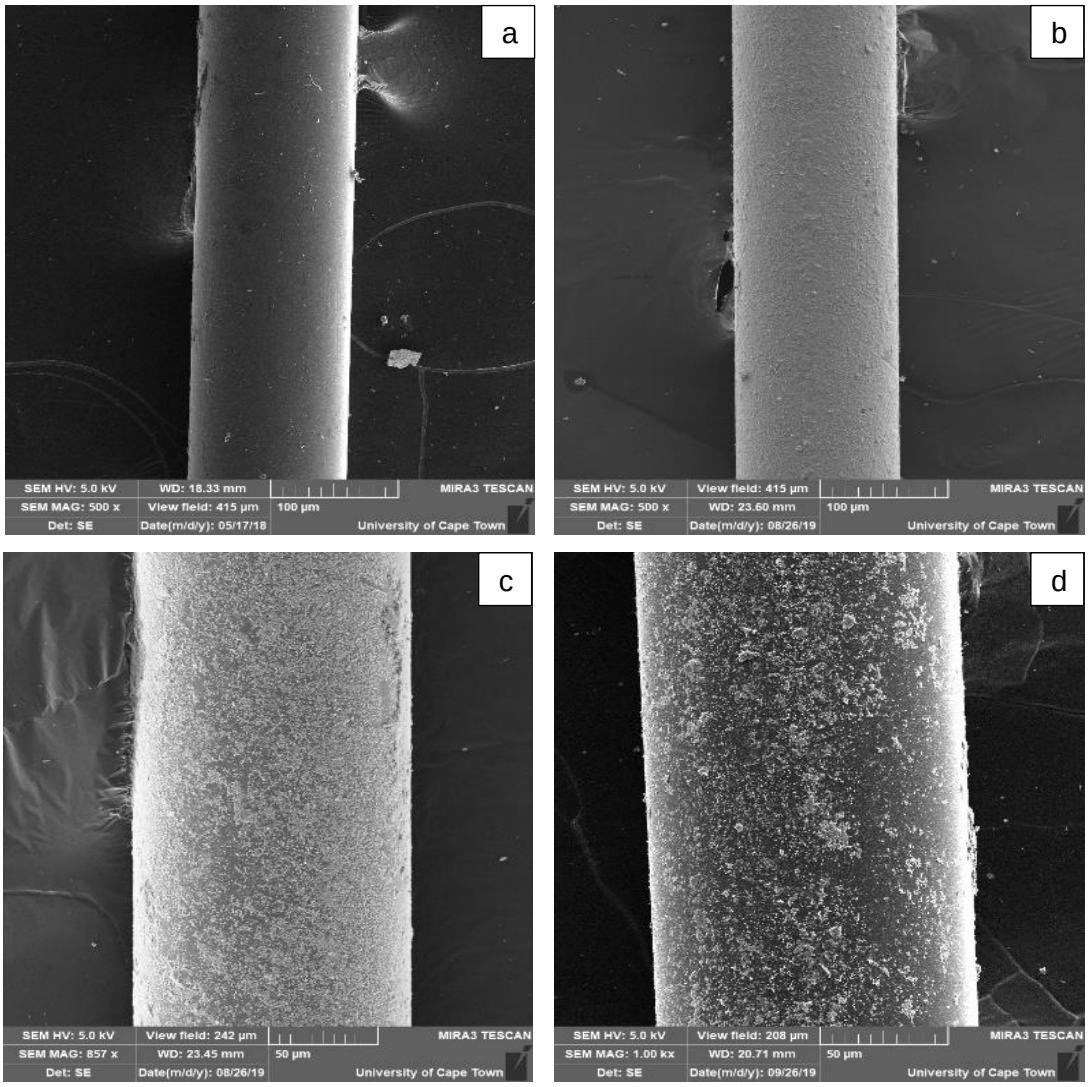

Figure 6-1: SEM images of bare optical fibre and optical fibre coated by pulling through a slurry containing P25. (a) Bare optical fibre at 500X magnification, (b) High surface coverage at 500X magnification, (c) Moderate surface coverage at 1000X magnification and (d) Low surface coverage at 1000X magnification

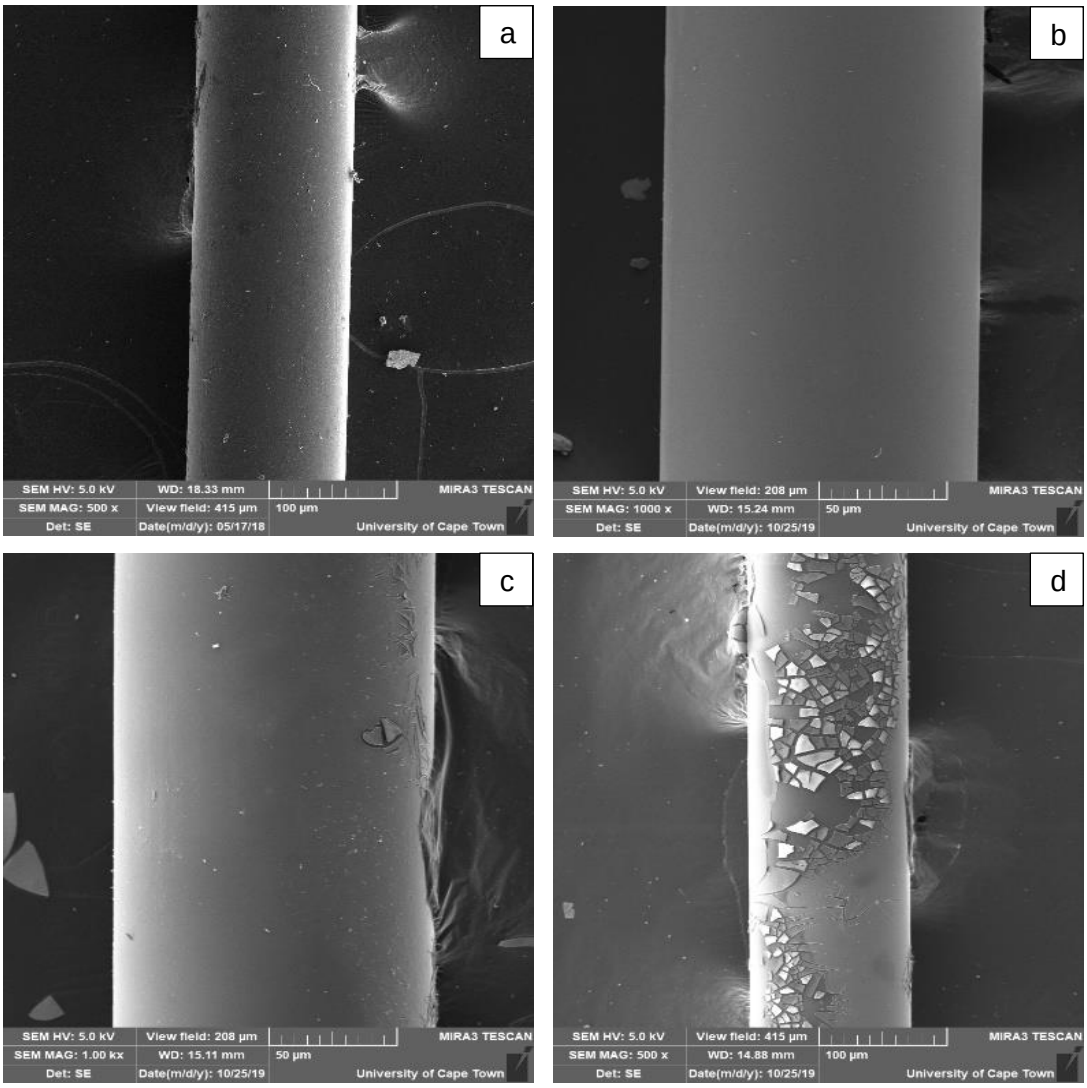

Figure 6-2: SEM images of bare optical fibre and optical fibre coated with titania obtained from the sol-gel process. (a) Bare optical fibre at 500X magnification, (b) High surface coverage at 1000X magnification, (c) Moderate surface coverage at 1000X magnification and (d) Low surface coverage at 500X magnification

6.3.2. Homogeneity of the surface coating

The homogeneity of the surface is assessed by the extent of the deformations on the coating. The homogeneity of the P25 slurry coated optical fibres is a measure of the dispersion of the TiO_2 particles on the surface which may cause agglomerations and uneven coverage as seen in Figure 6-3 (a). The homogeneity of the sol-gel coated optical fibre is mostly determined by the presence and extent of cracking on the surface as seen in Figure 6-3 (b).

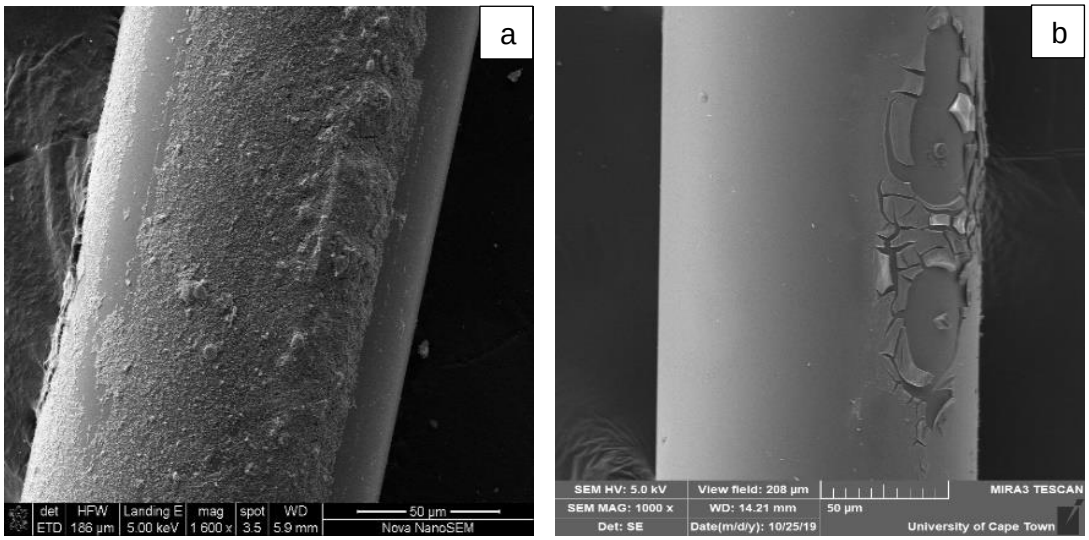

Figure 6-3:SEM of two coated fibres at 1000X magnification showing inhomogeneity of the coating, (a) coating using a slurry of P25 (b) coated by pulling through a gel obtained from sol-gel process

6.4. Optical fibre coating characterisation

The photocatalyst that was synthesised and used in the project was characterised using various methods. Raman mapping was done on samples coated using the sol-gel method to determine whether TiO_2 was formed and if so, what crystal phase was formed. Furthermore, scanning electron microscopy was used to evaluate the thickness of the catalyst coating on the fibre.

6.4.1. Raman mapping

For sol-gel coating, the suspension was calcined in air in Unit 5. The pulling speed determines the duration that an area of the coated optical fibre spends in the oven. Hence, the pulling speed also determines the residence time in the furnace. The calcination temperature and residence time are variables that can be adjusted in order to ensure complete transformation of the sol-gel suspension into a TiO_2 film. To date, the catalyst coating of optical fibre has been done by hand. The calcination step ranges from heat treatment durations of between 5 - 6 hours at temperatures between 500 °C - 700 °C. Calcination temperature has been reported

to influence the crystal phase of TiO_2 that is formed. XRD could not be used for the identification of the crystal phase due to the insufficient loading of catalyst in the crushed amorphous fused silica optical fibre sample. This is caused by the very thin coating of TiO_2 on the optical fibre. Therefore, Raman was chosen to confirm the crystal phase of TiO_2 for varying calcination temperatures and residence times. Anatase form of TiO_2 has been reported to have superior photoactivity when compared to rutile [72,73]. Therefore, for this project, anatase is the desired crystal phase of TiO_2.

6.4.1.1. Effect of speed and residence time on the crystal structure of sol-gel coated optical fibre

Table 6-2 shows the range of pulling speeds that were investigated in the project as well as the corresponding optical fibre residence times in Unit 5. TiO_2 synthesis using the sol-gel method has been reported to use a calcination time of ca. 5 hours [1,6]. The residence times that were used in this study vary drastically between the fastest and slowest speed and are between 85.5% (slowest speed) to 99.5% (fastest speed) lower than the literature value of 5 hours .Therefore, it is important to ensure that the extreme change in the preparation method does not affect the expected coating layer. Experiments were done by varying pulling speed while maintaining a calcination temperature of 500 °C.

Table 6-2: Pulling speed range and corresponding residence times of optical fibre in Unit 5 at 500°C

Pulling Speed ($mm.s^{-1}$)	Residence Time (min)
0.12	43.41
0.58	8.68
1.15	4.34
1.73	2.89
2.30	2.17
2.88	1.74
3.46	1.45

Figure 6-4 shows an example of the images taken of the surface of the coated optical fibre sample that was mapped using the Raman. The sample acts as a representation of the batch as it was chosen at random. It can be seen from the Raman map that the coating has a relatively uniform thickness along the length of the optical fibre. Furthermore, the coverage of the coating appears to be satisfactory with only minor defects for this sample.

Based on Figure 6-4, the surface has moderate coverage based on the inconsistent layer shown in red. Furthermore, the height of the red layer was not consistent in certain areas suggesting that the homogeneity of the coverage was poor. Since the sol-gel TiO_2 coatings are skin-like, it is difficult to visibly detect the difference between the bare optical fibre and smoothly coated fibre. Therefore, It should be noted that coating deformations such as cracks and bumps were chosen to map over in order to ensure the presence of the catalyst film in that sample area.

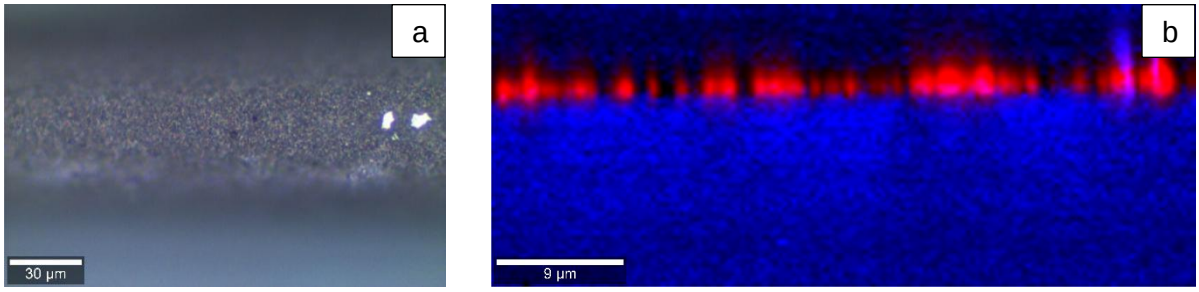

Figure 6-4: Raman map of optical fibre coated using the sol-gel method (pulling speed: 0.58 $mm \cdot s^{-1}$; calcination: 8.7 min at 500°C). (a) Sample map, (b) Raman map

Figure 6-5 shows, the Raman spectrum obtained for each pulling speed investigated. Shown in Figure 6-5 is the Raman spectrum for the sample collected at a pulling speed of 1.12 $mm.s^{-1}$, 43.41 minutes residence time and 500 °C calcination time. The spectrum obtained is compared to the reference for anatase TiO_2 and rutile TiO_2. It is confirmed that the crystal phase of TiO_2 formed using the sol-gel method was anatase as the spectrum of the sample and the anatase reference both showed large speaks at ca 150 cm^{-1} whereas the rutile reference shows a large peak at ca. 610 cm^{-1} . The results obtained for all residence times investigated showed that anatase was formed for all residence times despite the much shorter calcination time used on the automated set-up that typically used in the batch preparation of titania using the sol-gel process [1,6] (see Figure 6-6). This may possibly indicate that the process is not limited by a solid-state reaction. The fibre with a thin coating moving through the furnace will allow effective removal of product compounds, such as water, in comparison to a thick layer of material in a static oven used in typical catalyst preparation methods. Sample images and Raman maps for each residence time can be found in Appendix B.1.

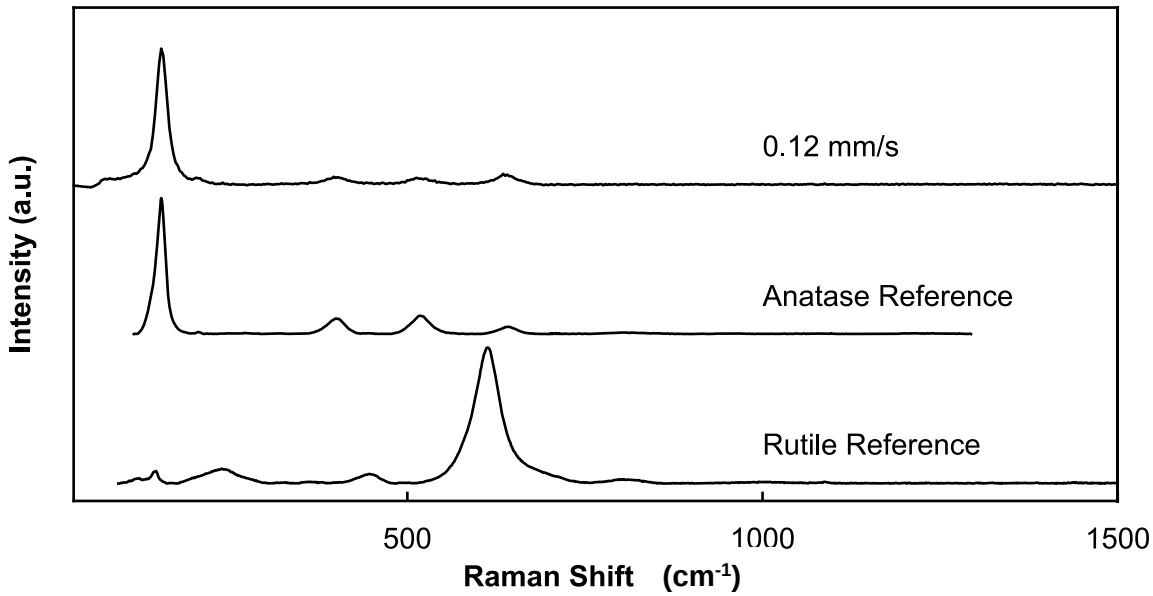

Figure 6-5: Determination of TiO_2 crystal phase formed using the sol-gel coating method at a calcination temperature of 500 °C and speed of 0.12 mm.s^{-1}

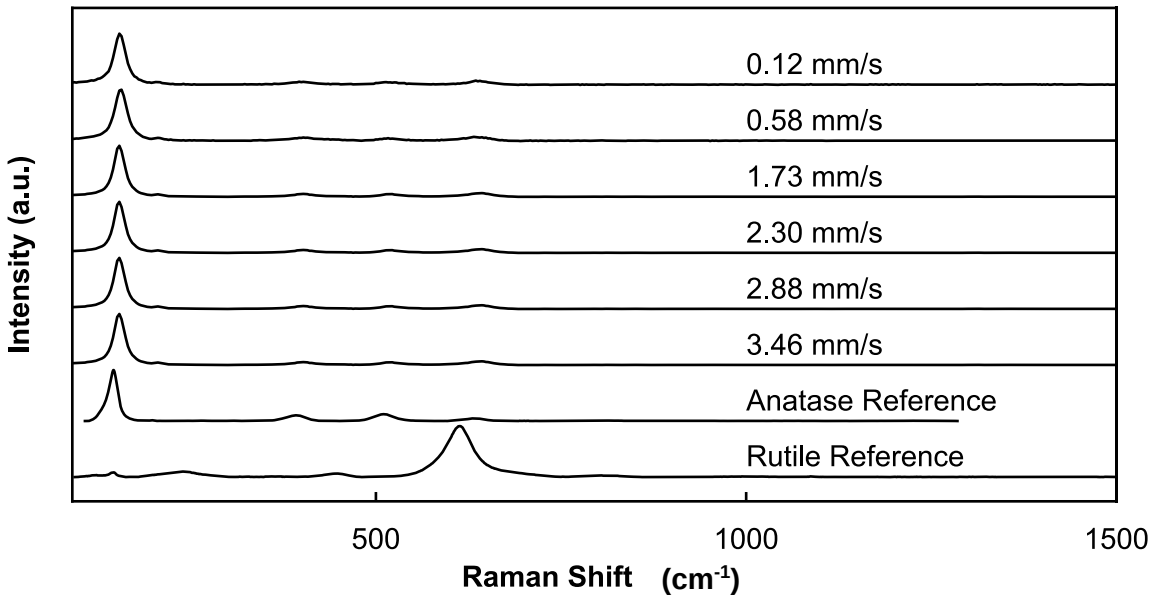

Figure 6-6: Effect of the pulling speed on the Raman spectrum obtained from the Raman map of the sol-gel coated the optical at a calcination temperature of 500 °C

6.4.1.2. Effect of calcination temperature

The calcination temperature plays a crucial role in determining the structural and optical properties of TiO_2 that is prepared via the sol-gel preparation method. It has been shown that non-crystalline TiO_2 can be formed at calcination temperatures below 400°C, whereas the formation of anatase occurs at calcination temperatures between 400°C – 600°C [66]. The phase transformation of TiO_2 from anatase to rutile is reported to occur at calcination temperatures above 600 °C depending on the catalyst preparation method. Therefore, since anatase is the desired crystal phase, a calcination temperature in the range between 400 °C - 600 °C was investigated in order to determine the effect it has on the crystal phase of TiO_2 formed in the new preparation system's operating conditions. Figure 6-7 (a), shows an image of the coated optical fibre that was sampled. Figure 6-7 (b), is the Raman map of the sample which confirms the coating thickness uniformity along the optical fibre length that was sampled. Sample images and Raman maps obtained from experiments can be found in Appendix B.1. Experiments were done by varying calcination temperature while maintaining a constant pulling speed of 1.15 $mm{\cdot}s^{-1}$ which corresponds to a residence time of 4.34 min in the oven.

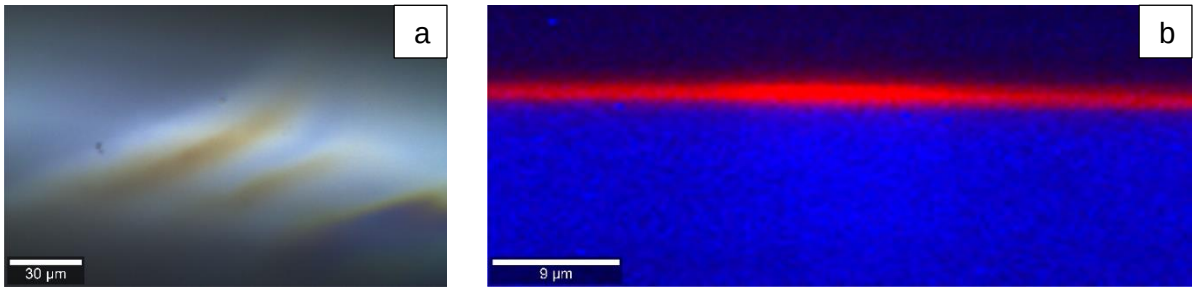

Figure 6-7: Raman map of optical fibre coated using the sol-gel method (pulling speed: 1.15 $mm{\cdot}s^{-1}$; calcination: 4.3 min at 500°C). (a) Sample map, (b) Raman map

Figure 6-8 illustrates the Raman plot for the coated optical fibre that was calcined at different temperatures. It can be seen that the collected Raman spectra and the anatase reference all show a large characteristic speak at ca. 150 cm^{-1} whereas the rutile reference shows this characteristic peak at ca. 610 cm^{-1}. This confirms that anatase was formed for the temperature range of 400 °C – 600 °C that was investigated. This corresponds to results reported by Hamadanian *et al.* [66]. It can thus be concluded that the coating consists of pure anatase if the optical fibre is coated by dip-coating in the gel obtained from the sol-gel process and calcined in the temperature range between 400 ^oC and 600 ^oC using a pulling speed between 0.12 $mm.s^{-1}$ and 3.46 $mm.s^{-1}$

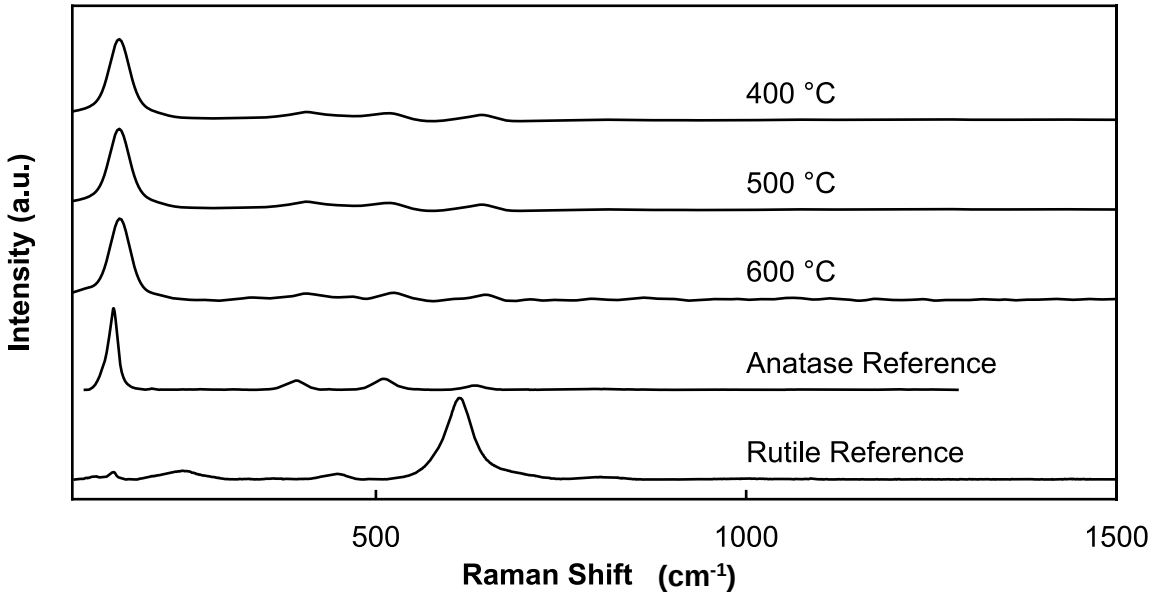

Figure 6-8: Effect of calcination temperature on the Raman spectrum obtained from the sol-gel coated on the optical fibre obtained by dip-coating.

6.4.2. Evaluation of process variables on coating morphology and thickness

The automated optical fibre catalyst coating process (AOFCCP) was used to coat the optical fibre with TiO_2 photocatalyst. Various process variables were investigated for two different coating methods, namely sol-gel and P25 slurry coating. This was done in order to determine the effect of these process variables, which were outlined above, on the coating morphology and thickness. This is crucial in order to establish a system which can produce controllable catalyst coating thickness of between 0.4 – 1.1 µm (see Table 4-1). The experiments were performed in triplicate and the results are outlined below. The coating morphology and thickness were evaluated using SEM images. The results section, below, shows how each process variable affects the system results achieved for both the sol-gel and P25 slurry coating methods.

6.4.2.1. Standard process conditions

For each process variable that was investigated an operating range was chosen. in order to test the repeatability of the system, all other system process variables and conditions were kept constant. Therefore, standard process conditions were chosen, as seen in Table 6-3 The automated optical fibre catalyst coating process (AOFCCP) was operated at the standard process conditions by dip-coating either a slurry containing P25 or a gel obtained from the sol-gel procedure. These results were used as a base case for further investigations.

Table 6-3: Standard operation conditions in the automated optical fibre catalyst coating process

Process Variable	Slurry of P25	Gel from sol-gel process
Pulling speed ($mm \cdot s^{-1}$)	1.15	1.15
Solid content (wt.-%)	5	3.47
pH of the slurry[1]	4.65	3
Drying temperature (°C)	200	500

6.4.2.1.1. Dip-coating the optical fibre in a slurry containing P25

The results of the coating of optical fibre by dip-coating using a slurry containing P25 using the automated optical fibre catalyst coating process (AOFCCP) at the standard conditions (pulling speed of 1.15 $mm \cdot s^{-1}$, solid content in the slurry of 5 wt.-%, pH of the slurry of 4.65 and a drying temperature of 200 °C) is given in Figure 6-9. The average coating thickness measured after triplicate runs was 0.48 µm with a 3% deviation. The surface morphology showed high surface coverage with a good homogeneity was good as seen by minimal agglomeration and deformation on the coating surface. It can be stated that the system is able to meet the design requirements using the standard process conditions since it produces a coated optical fibre with high surface coverages and homogeneity, with a thickness that falls within the desired range of 0.4 -1.1 µm.

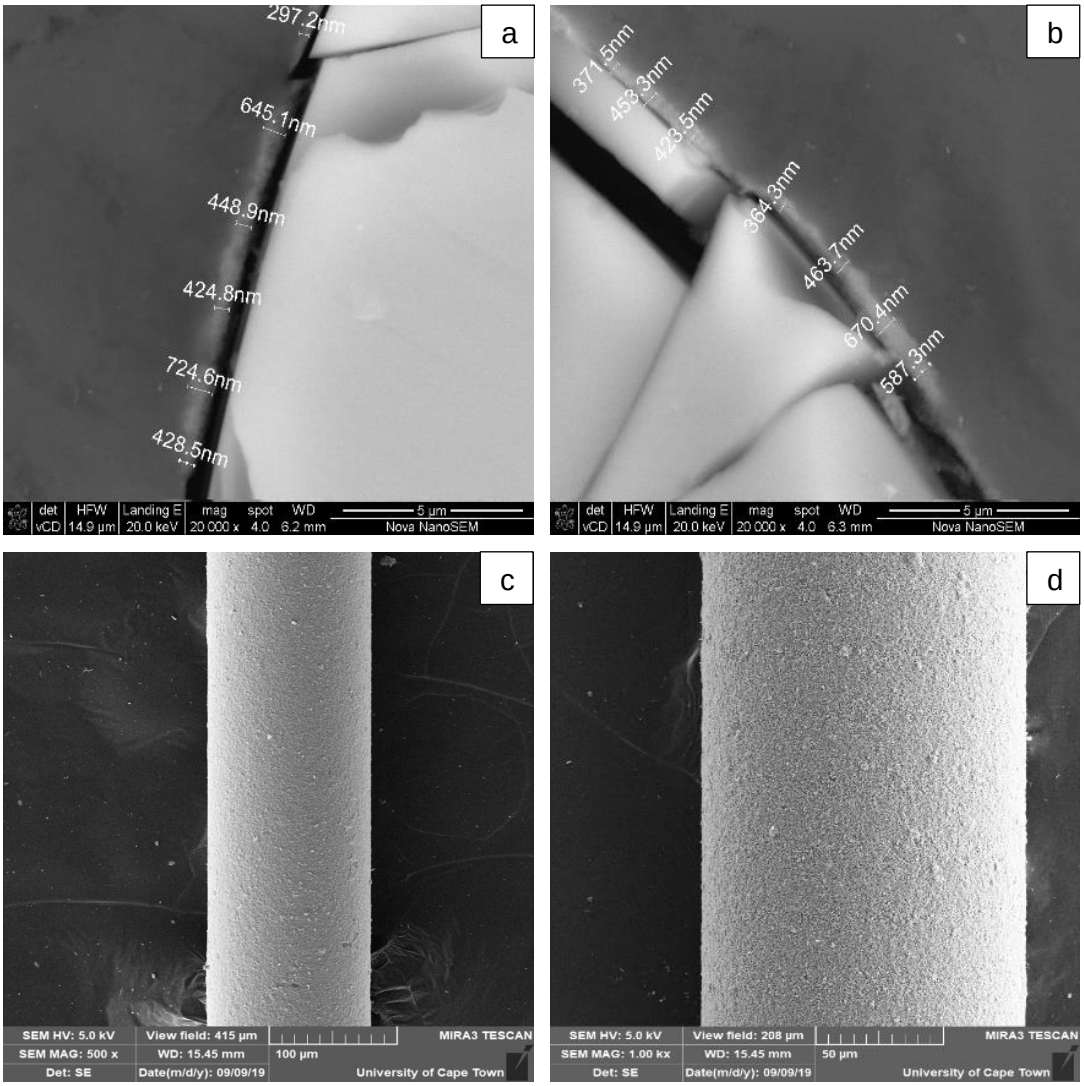

6.4.2.1.2. Dip-coating the optical fibre in a gel from sol-gel processing

Figure 6-9: SEM of coated optical fibre produced by dip-coating in slurry containing P25 at standard process conditions (see Table 6.3). (a & b) Coating thickness measurements, (c & d) Surface morphology images at 500X and 1000X magnification respectively.

The standard process conditions that were chosen for the sol-gel coating on the AOFCCP were a pulling speed of 1.15 $mm.s^{-1}$ and calcination temperature of 500 °C. The resulting optical fibre can be seen in Figure 6-10, which show the coating thickness – measured using SEM – and the surface morphology. The average coating thickness measured after triplicate runs was 0.37 µm with a 0.45 % deviation. The coating on the optical fibre had high coverage and the coating on the surface appeared to be homogeneously smooth with no visible deformations and cracking. It can be stated that for the standard process conditions the system is able to produce coated optical fibre with high surface coverages and homogeneity however the thickness is below the desired range (see Table 6-3). Therefore, temperature and pulling speed must be further investigated in order to determine their effect on the coating

thickness and morphology. It can be seen in Figure 6-10 (b), the coating layer shifted away from the optical fibre surface, this is possibly caused by the drying of the resin.

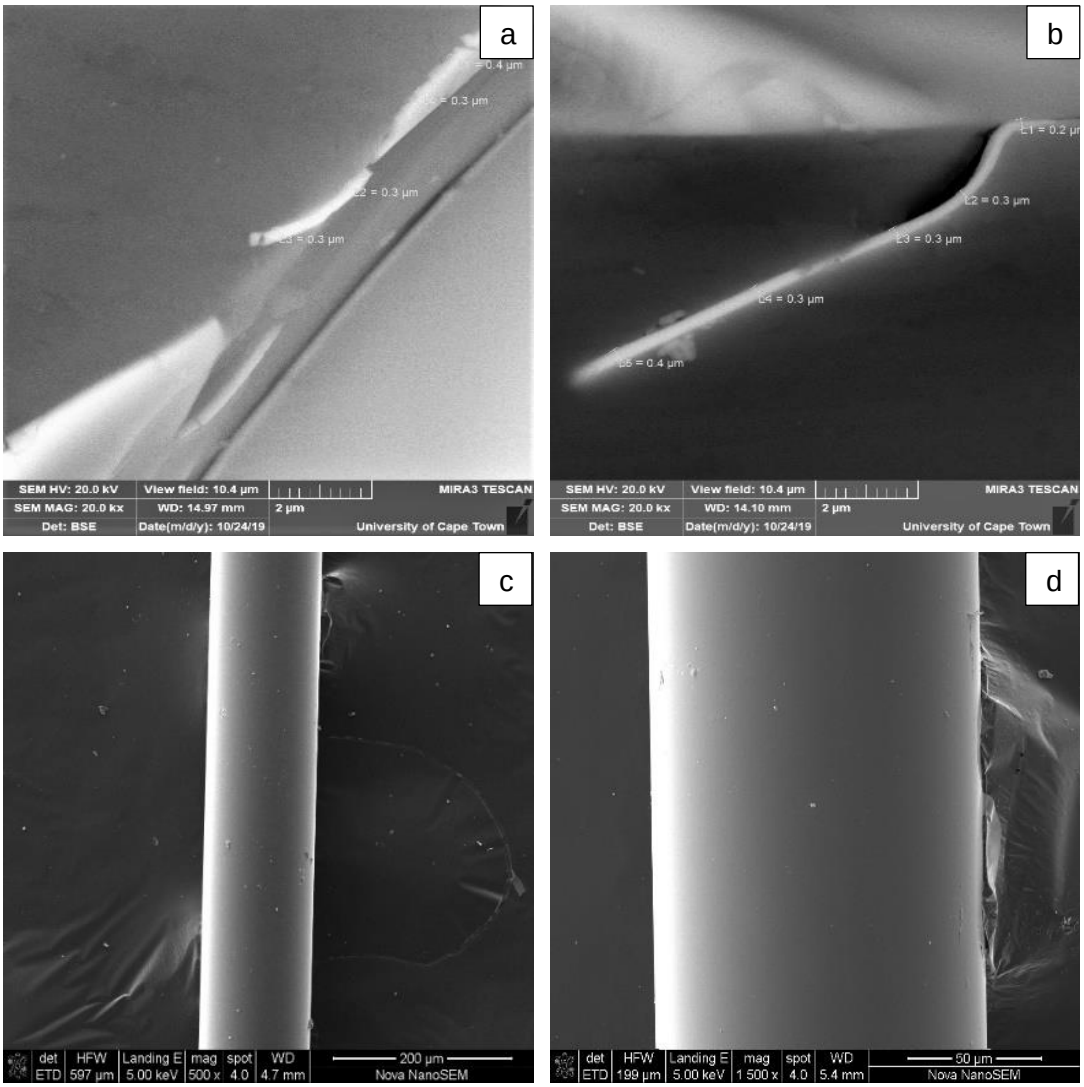

Figure 6-10: SEM of coated optical fibre by dip-coating in a gel at standard process conditions (1.15 mm·s^{-1}, 500°C). (a & b) Coating thickness measurements, (c & d) Surface morphology images at 500X and 1000X magnification respectively.

6.4.2.2. Effect of pulling speed on coating morphology and thickness

The effect of pulling speed was investigated in the automated process. This variable affects two areas in the process namely, withdrawal speed from the dip-coating process as well as the residence time of the optical fibre in the oven.

The classical dip-coating approach involves the submersion then withdrawal of a substrate out of a solution at a constant speed. The withdrawal speed of the substrate out of the solution is an important variable in the coating process and plays a crucial role in controlling the properties of the coated film [49, 68, 69]. The thickness of the film that is deposited on the optical fibre is controlled by factors such as the draining and entraining forces as well as the

drying rates [68, 69]. Draining forces allow the liquid to move away from the optical fibre whereas entraining forces work to retain the liquid on the optical fibre [51]. The rate of evaporation in the drying process also plays a crucial role in determining the thickness of the layer. Therefore, the speed at which the optical fibre is withdrawn from the solution affects these factors which in turn affect the thickness of the film. There are two forms of drying that occurs, the first being the constant rate period drying, i.e. the rate of evaporation controls the process, which occurs during or after coating of the optical fibre when the solvent evaporates uniformly from the surface of the saturated film [51]. The second form of drying is called the falling film rate period. This is diffusion-controlled process, which occurs on the unsaturated film that is formed after constant rate drying has taken place [51] .

The effect of withdrawal speed on the film thickness has been widely studied and it has been reported that the thickness of the film increases with increasing withdrawal speeds under certain conditions [68 – 70] using any aqueous solution under the appropriate process conditions [74]. Dip-coating under extreme conditions, in the so-called capillary regime, can achieve ultra-thick films even when using highly diluted solutions at ultra-low withdrawal speeds (lower than 0.1 $mm{\cdot}s^{-1}$) [70]. In the intermediate regime (withdrawal speeds between 0.1 -1 $mm{\cdot}s^{-1}$) and the viscous drag regime (withdrawal speeds > 1 $mm{\cdot}s^{-1}$) the thickness of the film layer is proportional to the withdrawal speed by either $t_f = U^{\frac{2}{3}}$ or $t_f = U^{\frac{1}{2}}$ under certain conditions [70 – 72].

For both coating methods, the principle behind the effect of the pulling speed was the same with only variations due to the differences in the coating medium. The pulling speed that is chosen affects the withdrawal speed of the optical fibre out of the coating solution. At fast speeds thicker coatings are expected due to decreased time for gravitational draining and evaporation [51]. Moreover, for fast pulling speeds, there is a decrease in residence drying time, which results in the drying of the film to be dominated by constant rate period. The thickness will thus be dependent on the initial thickness entrained on the optical fibre which results in a thicker film [8,12]. For slow speeds, the thickness of the film coated on the optical fibre is controlled by the evaporation and gravitational forces [8,12]. Due to the increase in time, there is more drainage that occurs resulting in a decrease in coating thickness. The drying is dominated by the falling rate period which results in a greater amount of evaporation and thus a decrease in film thickness [8, 11, 12].

6.4.2.2.1. Coating by dip-coating using a slurry containing P25

The coating coverage and homogeneity of the optical fibres were determined using SEM. Images were taken to determine the effect that the withdrawal speed has on the coating. It can be seen in Figure 6-12 that the coating is a rather rough, corrugated layer regardless of the withdrawal speed chosen. The coverage of the optical fibre seemed to become better with higher pulling speeds. The slowest speed of 0.1 $mm{\cdot}s^{-1}$ showed a slightly poor coating as indicated by the visible appearance of the optical fibre through the coating. The homogeneity of the coating also increased with an increase in withdrawal speed. It can be seen that for the fastest speed, there is a drain line which is possibly due to the short residence time. This resulted in the poor drainage of the slurry causing poor homogeneity of the coating. The thickness of the catalyst coating on the optical fibre as a function of the pulling speed as obtained from the automated optical fibre catalyst coating processes are given in Figure 6-11.

It can be seen that there is an increase in thickness as a function of withdrawal speed. The highest achieved thickness was 0.7 µm with a 1.48% deviation at a pulling speed of 3.46 $mm.s^{-1}$. The thicknesses agreed with what was expected from the intermediate and viscous drag regimes when compared to work done by Grosso *et al*. [77]. For fast withdrawal speeds, the coating is governed by the film that is initially entrained on the optical fibre. Since the withdrawal speed is fast there is decreased time for drainage due to gravity as well as evaporation. For slow speeds, the thickness is governed by the gravitational and drainage forces. The coating thickness is directly proportional to the pulling speed for the range of 0.12 $mm.s^{-1}$ – 3.46 $mm.s^{-1}$ that was investigated.

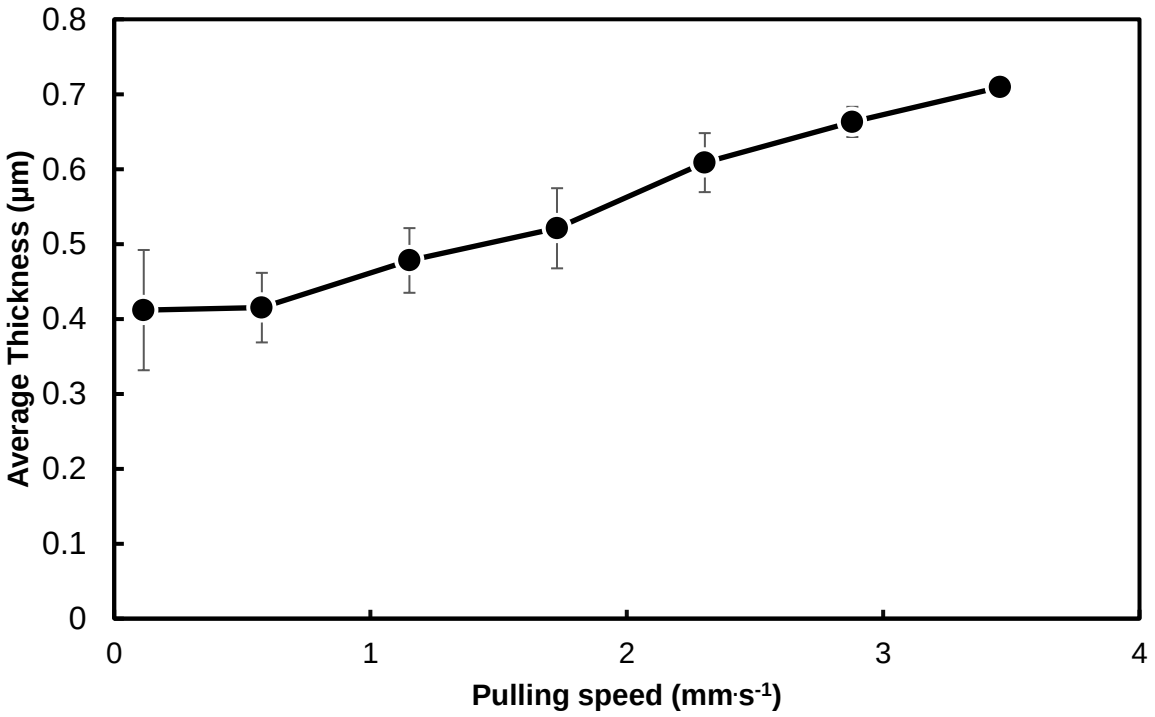

Figure 6-11: Effect of the pulling speed on the average coating thickness on the optical fibre achieved by dip-coating in a slurry containing P25 using the AOFCCP under standard process condition (see Table 6.3)

Figure 6-11 illustrates the effect the pulling speed had on the average coating thickness. It can be seen that for slow speed of 0.12 $mm.s^{-1}$ - 0.58 $mm.s^{-1}$ there is only a 1% deviation which indicates that for these speeds the formation of the coating layer on the optical fibre is governed by the diffusion rate and hence falling rate period drying occurs. This may indicate that the thickness of 0.4 µm is closely approaching the minimum thickness that can be achieved using those specific process conditions. The constant rate period is the drying of the saturated film that is initially formed. Since the solvent is water with a boiling point of 100 °C, and the thickness is very small, we can assume that complete evaporation of the solvent occurs therefore, it can be assumed that the thickness of the film controlled by the pulling rate for constant temperature is unaffected by the residence drying time. Figure 6-13 shows the SEM images that were taken over the cross-section of the optical fibre recording the thickness achieved by the pulling rate.

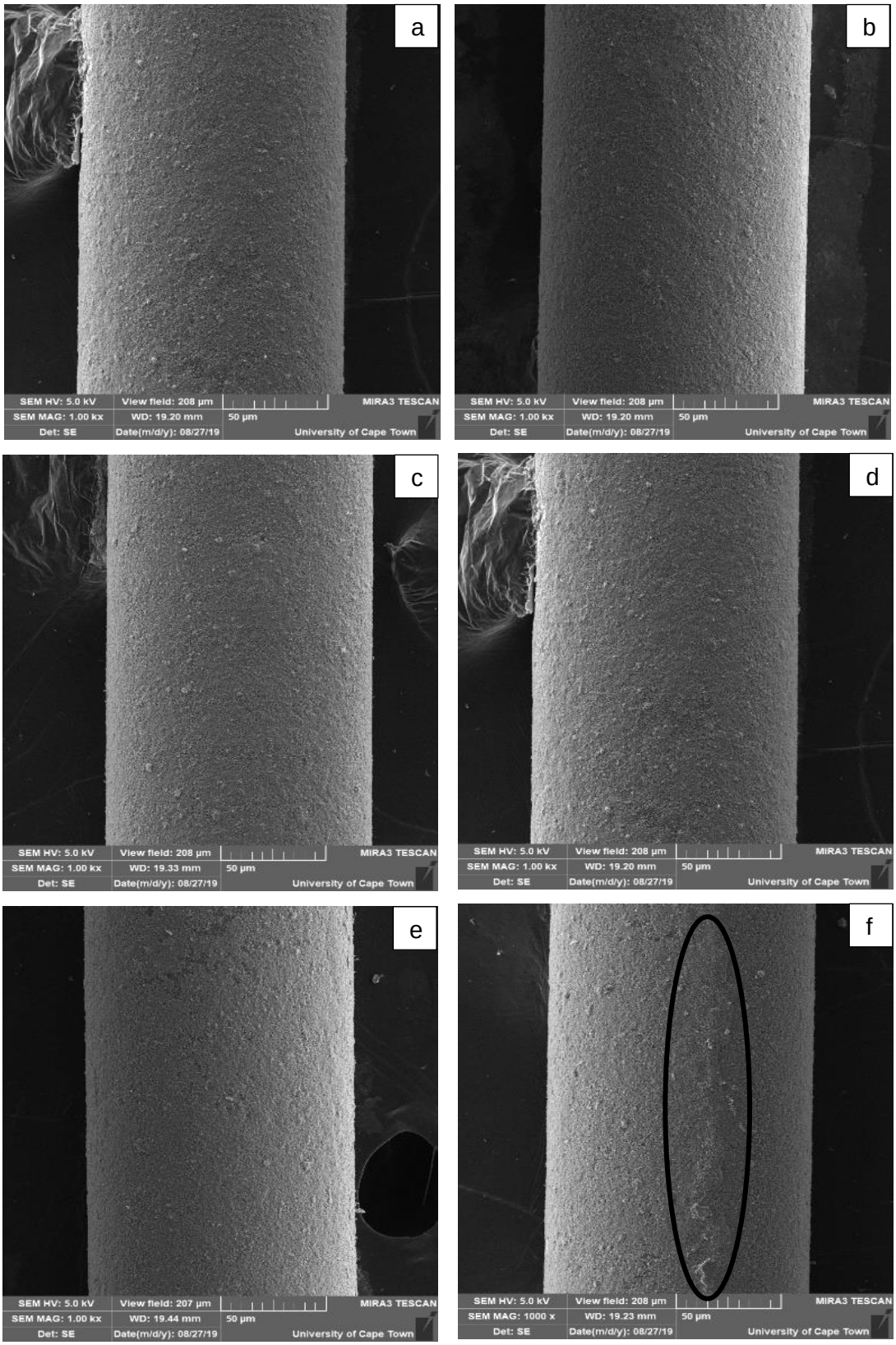

Figure 6-12: Surface morphology of the coated optical fibre by dip-coating in a slurry containing P25 using the AOFCCP at standard conditions (see Table 6.3), but various pulling speeds. (a) 0.12 mm·s^{-1}, (b) 0.58 mm·s^{-1}, (c) 1.73 mm·s^{-1}, (d) 2.30 mm·s^{-1}, (e) 2.88, (f) 3.46 mm·s^{-1}(drain line circled).

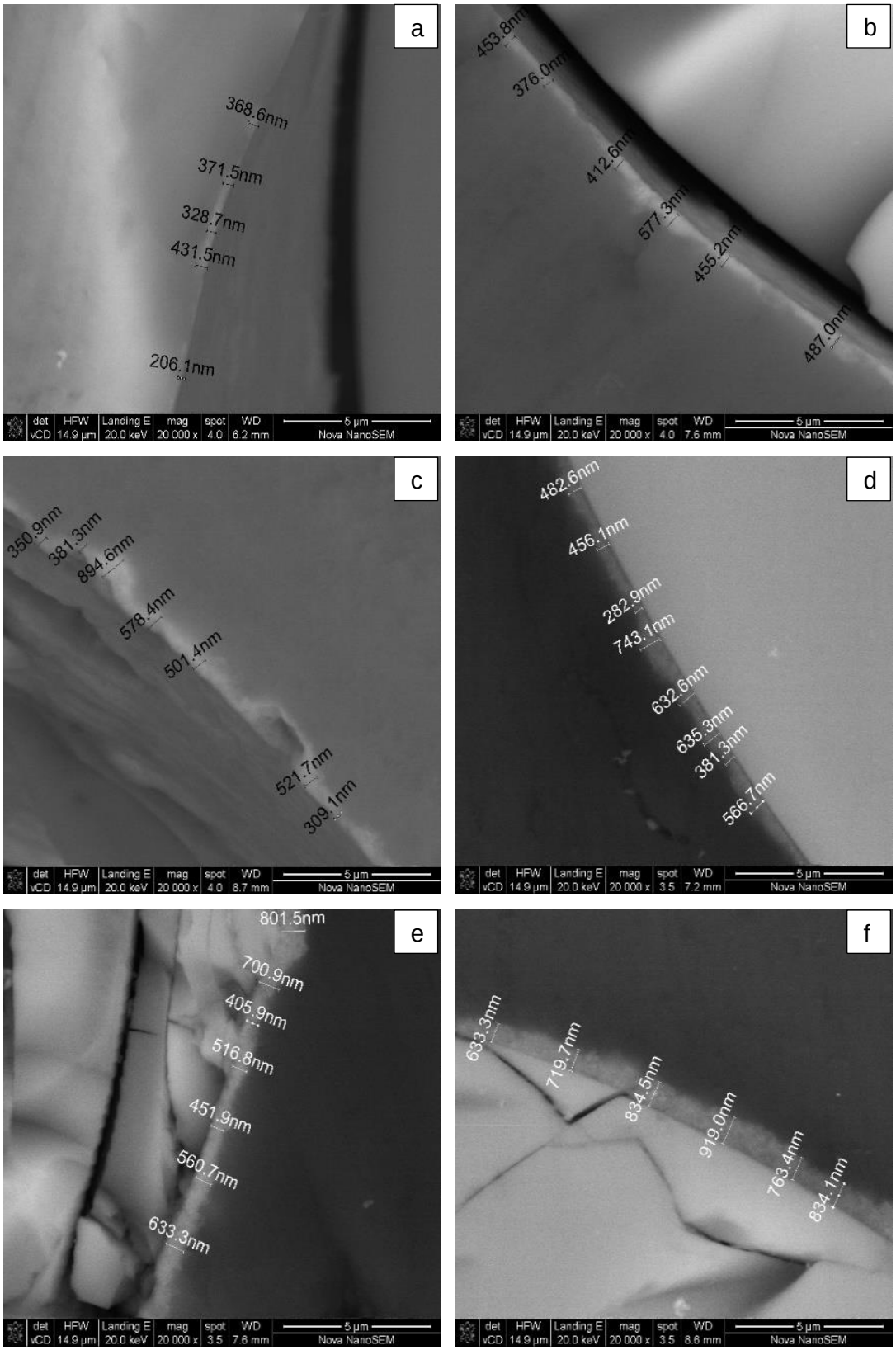

Figure 6-13: SEM coated optical fibre obtained by dip-coating from a slurry containin P25 at standard conditions (see Table 6.3) but various pulling speeds. (a) 0.12 mm.s^{-1}, (b) 0.58 mm.s^{-1}, (c) 1.73 mm.s^{-1}, (d) 2.30 mm.s^{-1}, (e) 2.30 mm.s^{-1}, (f) 3.46 mm.s^{-1}.

6.4.2.2.2. Sol-gel coating

The coverage of the film that was deposited was also studied as a function of the pulling speed (withdrawal speed). SEM was used to view the coverage of the coating. Figure 6-15 shows some of the SEM images taken for each of the used withdrawal speeds. The obtained coating was smooth and skin-like. Moreover, the homogeneity of the coating along the length of the optical fibre length. There were no cracks or defects observed on the coating obtained with a low pulling speed between 0.12 $mm{\cdot}s^{-1}$ - 1.15 $mm{\cdot}s^{-1}$. However, at a speed of 1.73 $mm{\cdot}s^{-1}$ coating deformation, in the form of cracking, was observed. The minimum thickness at which cracking is observed is known as the critical cracking thickness and was determined to be 0.52 µm. For withdrawal speeds of 1.73 $mm{\cdot}s^{-1}$- 3.46 $mm{\cdot}s^{-1}$, the coating was susceptible to cracking. The extent of the cracking worsened with the increase in pulling speed. This agreed with the results obtained from the work of Taherniya and Raoufi. [68] who showed that the films produced using the fastest withdrawal speeds resulted in the highest concentrations of cracking and inhomogeneity. Cracking can be prevented by controlling the annealing temperature and speed [72]. Figure 6-16 shows images of sol-gel coated samples which had the most severe cracking. It should be noted that the deformation was not uniform along the length of the optical fibre.

Figure 6-14 below illustrates the relationship between the thickness of the coating on the optical fibre and the pulling speed (withdrawal speed) for the optical fibre coating by the sol-gel method. Figure 6-17 illustrates some of the SEM images taken of the cross-section of the coated optical fibre for each pulling speed. There is an increase in the thickness of film with an increase in withdrawal speed for reasons previously described. According to Grosso . (2011), the speed range of 0.1 – 3 was in the intermediate viscous drag regime and agreed with trends obtained using the AOFCCP.

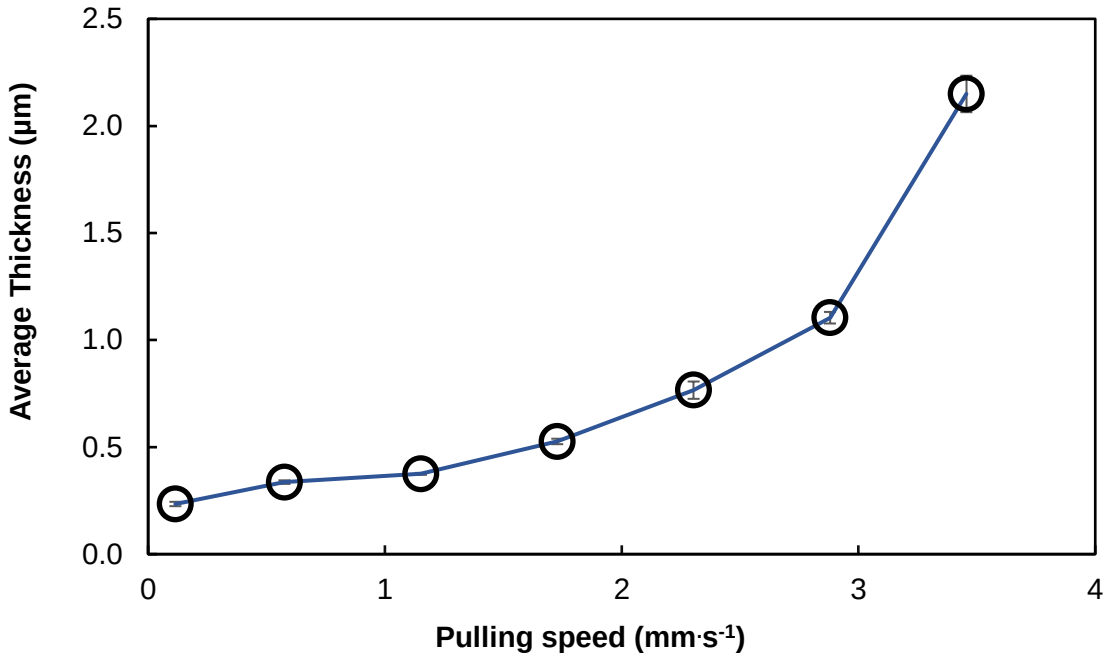

Figure 6-14: Effect of the pulling speed on the average coating achieved using the AOFCCP under standard process condition of 500 °C for sol-gel coating method.

Experiments performed by Gugliemli *et al*. [78], was done using a sol-gel method with the same chemicals used in this project. Various TiO_2 concentrations were synthesised of between 10 – 75 $g.l^{-1}$. The substrates were dip-coated with an automated dip-coater and calcined at 500 °C for 72 h. The results showed that with sol-gel dip-coating within a withdrawal speed range of 0.5 - 12.5 $mm.s^{-1}$, film thickness increased with increasing withdrawal speed. However, the obtained film thicknesses ranged between 15 - 300 nm with a maximum standard deviation of 5.6 %. This deviation is below 10% and therefore according to the assumptions set out in section **Error! Reference source not found.**, these coating layers can be regarded as uniform. These results were significantly lower than the results obtained using the AOFCCP shown in Figure 6-14 The discrepancies in the thicknesses may be due to the differences in the sol concentrations used, as well as the angle of immersion and emergence. Furthermore, factors such as humidity and heat treatment conditions used, as well as the atmosphere for evaporation were different from the standard process conditions used in this project. These factors have been reported to affect the deposited film thickness [71, 73]. it is important to note that the drying methods used were very different as those preparations were done by hand whereas the results obtained in this process was done using the automated process. Miki *et al.* [55] investigated the effect of the withdrawal speed on the film thickness for a speed range of 0.1 - 0.5 $mm{\cdot}s^{-1}$, obtained similar resulted, despite the inclusion of trehalose in the gel. There is only a 6% difference between the reported thickness obtained with a pulling speed of 0.1 $mm{\cdot}s^{-1}$ by Miki *et al.* [55] and the one obtained here.

However, the discrepancy becomes larger at a pulling speed of 0.5 $mm{\cdot}s^{-1}$ where the study by Miki *et al.* [55] yielded a thickness of ca. 0.41 µm greater than that achieved in this project .These differences are possibly due to the addition of the trehalose, which causes an increase in viscosity which is presumed to result in an increase in coating thickness, moreover, other process conditions such as heat treatment and sol concentration could also have attributed to the variations [57].

The precision in the results obtained for at least 1 run for the sol-gel, pulling speed experiments of sub-set 2.9 $mm.s^{-1}$ and 3.5 $mm.s^{-1}$ had a standard deviation of below 30%. This indicates that, based on the chosen assumptions, sol-gel experiments at these fast pulling speeds unreliable results and ununiform coating thicknesses.

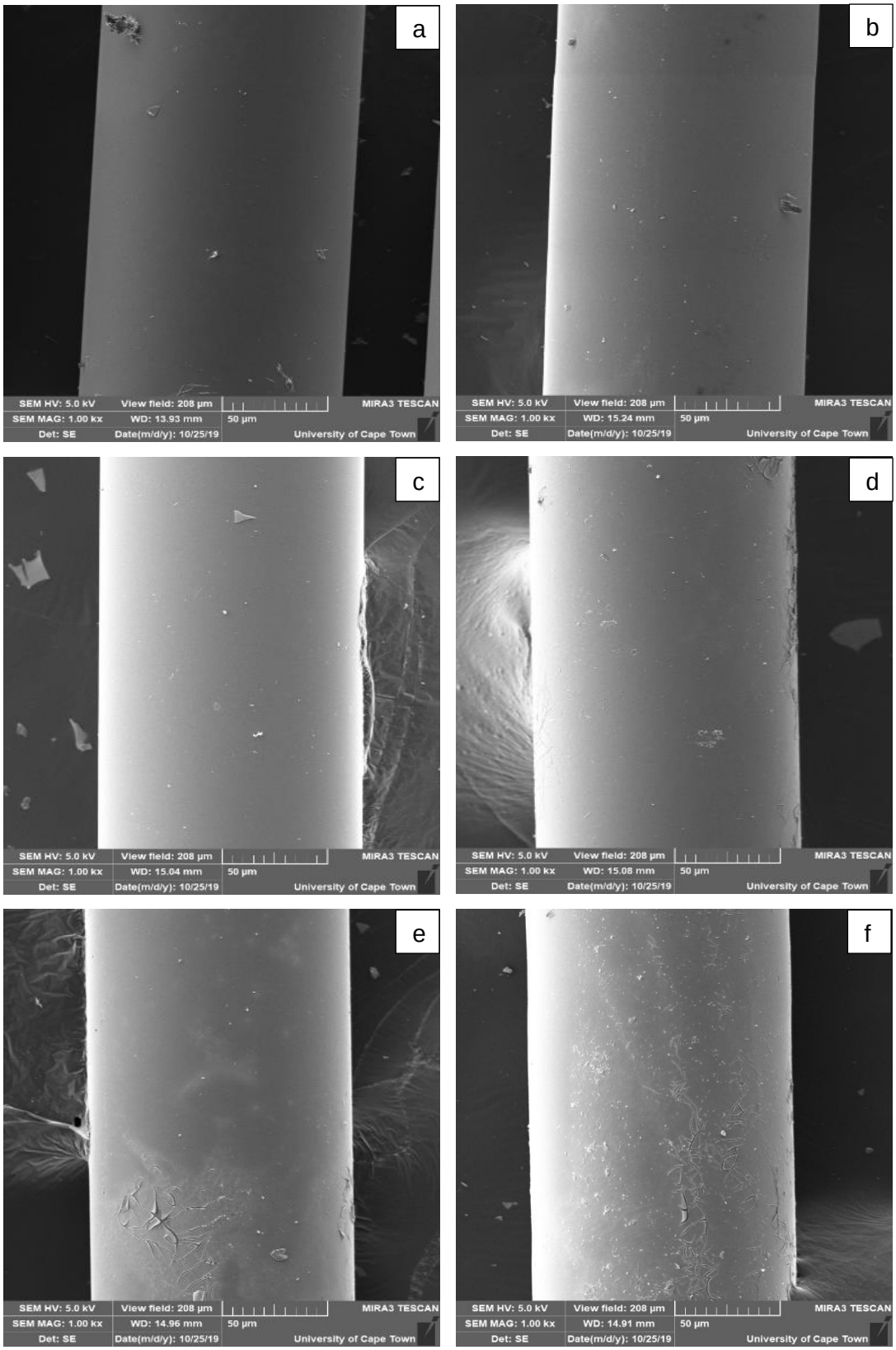

Figure 6-15: Surface morphology of coated optical fibre formed by dip-coating in gel (calcination 500 °C)for various pulling speeds (mm.s^{-1}) that were investigated. (a) 0.12 mm.s^{-1}, (b) 0.58 mm.s^{-1}, (c) 1.73 mm.s^{-1}, (d) 2.30 mm.s^{-1}, (e) 2.88 mm.s^{-1}, (f) 3.46 mm.s^{-1} .

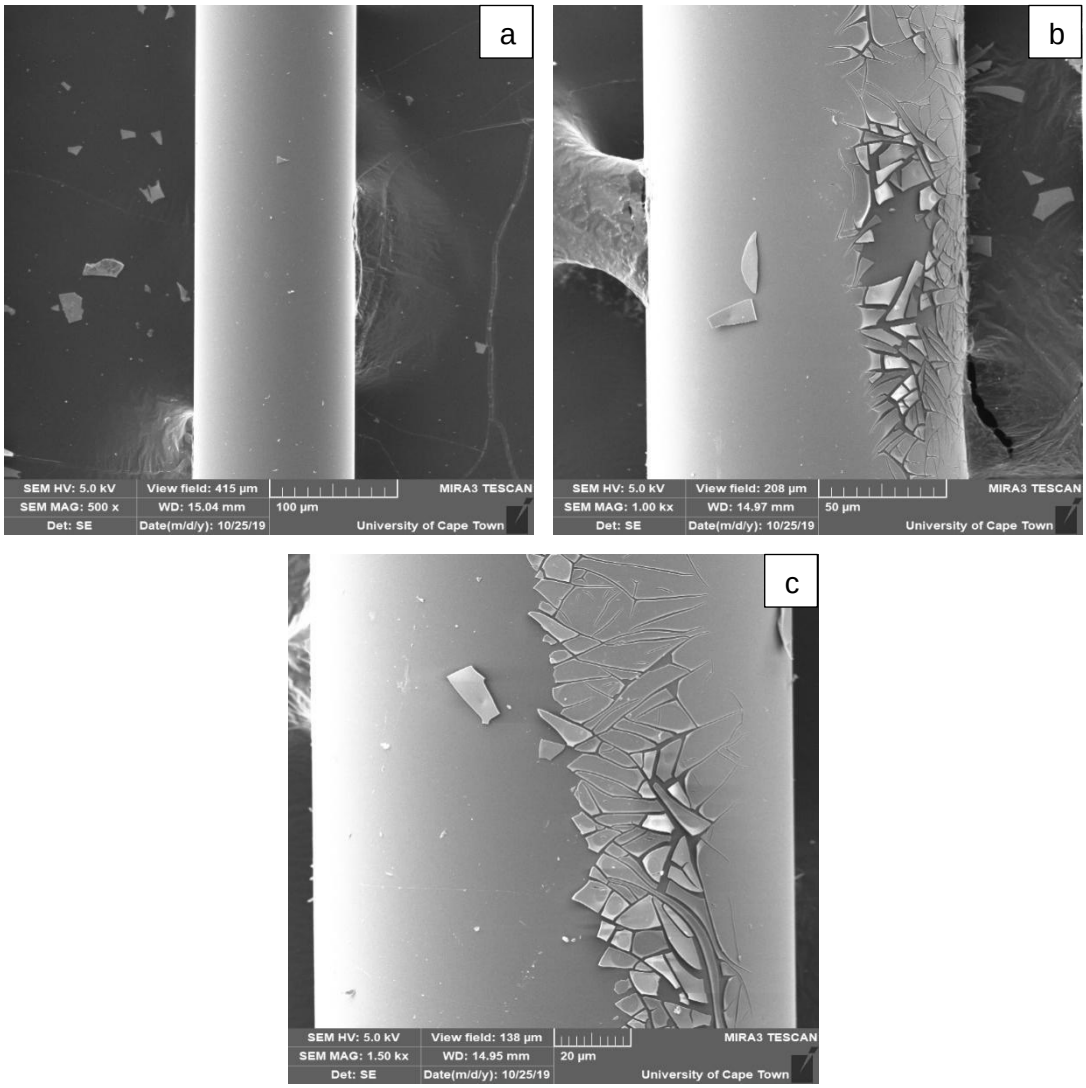

Figure 6-16: inconsistent deformations along the fibre length on coated optical fibre obtained by dip-coating using gel at a pulling speed of 3.46 mm·s^{-1} and calcination temperature of 500 °C (a) Smooth high coverage coating, (b) Cracking in a localised area of the coating and (c) More than half of the coating damaged.

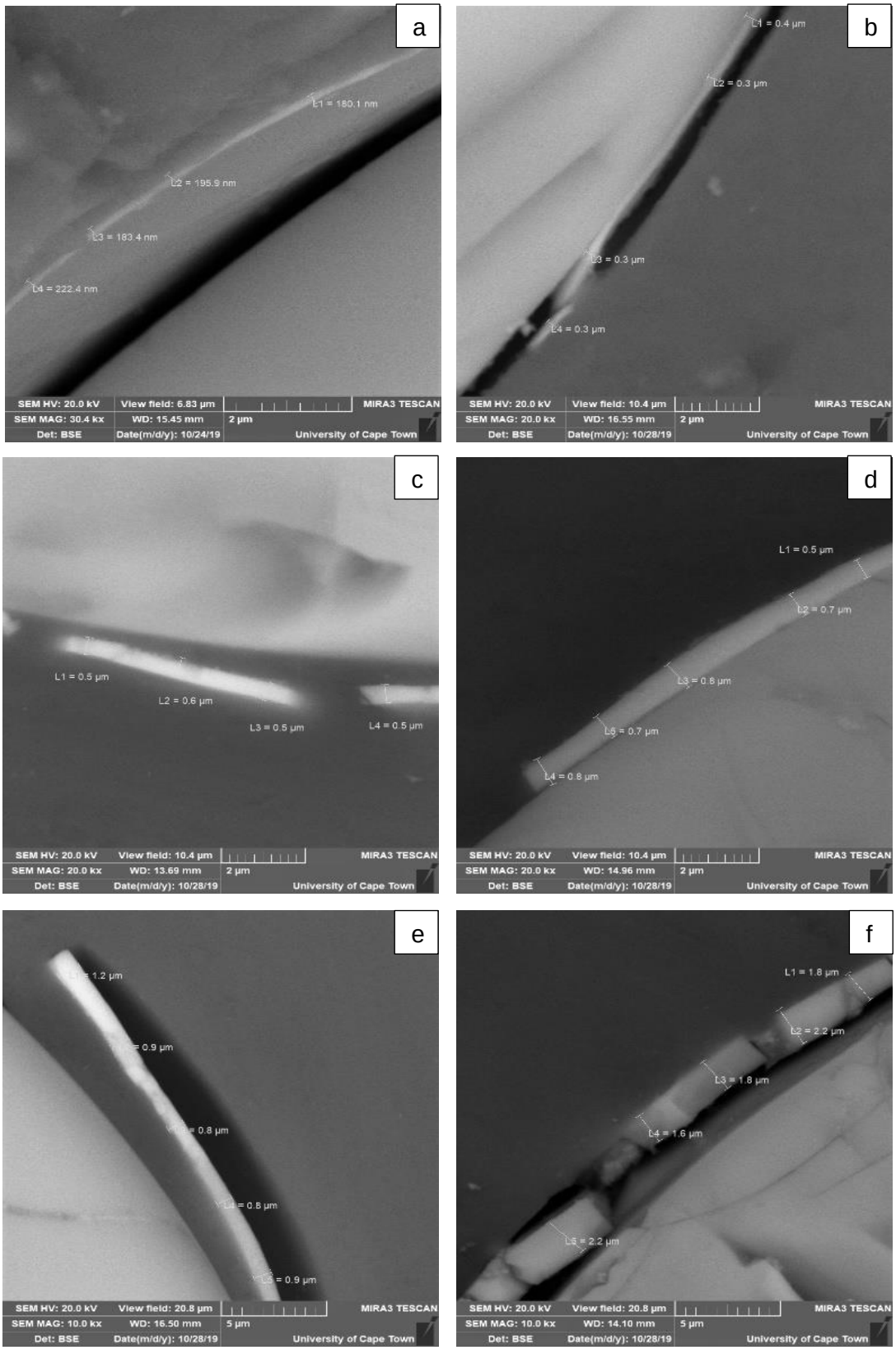

Figure 6-17:SEM of the coated optical fibre obtained from dip-coating a gel (Calacination: 500 ºC) that were investigated. (a) 0.12 mm·s^{-1}, (b) 0.58 mm·s^{-1}, (c) 1.73 mm·s^{-1}, (d) 2.30 mm·s^{-1}, (e) 2.88 mm·s^{-1}, (f) 3.46 mm·s^{-1}.

6.4.2.3. Effect of Drying Temperature on coating morphology and thickness

The second process variable that was tested was the operating temperature of Unit 5, the oven. The principle behind increasing the temperature of the oven is that it may increase the rate at which evaporation occurs, which has been reported to be an important parameter for the synthesis of immobilised photocatalyst thin films [66, 67]. The effect of the temperature on the coating layer is very different for the coating methods investigated. The operating temperature ranges which were investigated were different for the respective coating methods. These were chosen in conjunction with the appropriate preparation method in order to achieve the desired product. The results obtained from the experiments performed to determine the effect of the temperature on the optical fibre coating film thickness and coverage will be outlined below.

6.4.2.3.1. P25 Coating method

The effect of the drying temperature on the coating was investigated for the optical fibre coated by dip-coating in a slurry containing P25 using the AOFCCP. Since P25 is a mixture of anatase and rutile, the heat treatment step is used purely for the adhesion of the TiO_2 particles on to the optical fibre by the evaporation of the solvent. The solution consists of mainly deionised water and a buffer solution – made up of acetic acid and ammonium acetate – which have boiling points of below 150 °C.

The experiments were carried out using the AOFCCP with the standard conditions of pH 4.65, slurry concentration of 5 wt.-% and a pulling speed of 1.15 $mm \cdot s^{-1}$. The effect of the drying temperature on the coating thickness can be seen in Figure 6-18. The average thickness of photocatalyst film seems to increase with an increase in drying temperature. Since the temperatures that were tested were well above the boiling points of the solvent, the diffusion limitations by the catalyst layer in the drying process can be ignored and thus the catalyst layer formed is governed by constant rate period drying. Thus, the thickness of the coating is mainly controlled by the initial saturated layer formed on the optical fibre. A slight increase in the thickness of the coated layer is possibly due to the higher evaporation rate caused by the increase in temperature. This will reduce the amount of time for gravitational drainage to occur along the length of the optical fibre resulting in the increased drying rate and hence a thicker film.

Figure 6-19, displays the SEM images taken of the optical fibre surface in order to determine the effect that the drying temperature has on the surface coverage and homogeneity. The change in the drying temperature had no effect on the surface coverage and homogeneity of the coating. The coating for all the experiments was found to be corrugated with minimal agglomerations and medium to high surface coverage

Figure 6-20 shows the SEM images that were taken of the cross-section of the coated optical fibre in order to determine the thickness of the coating for each experiment at the various temperatures.

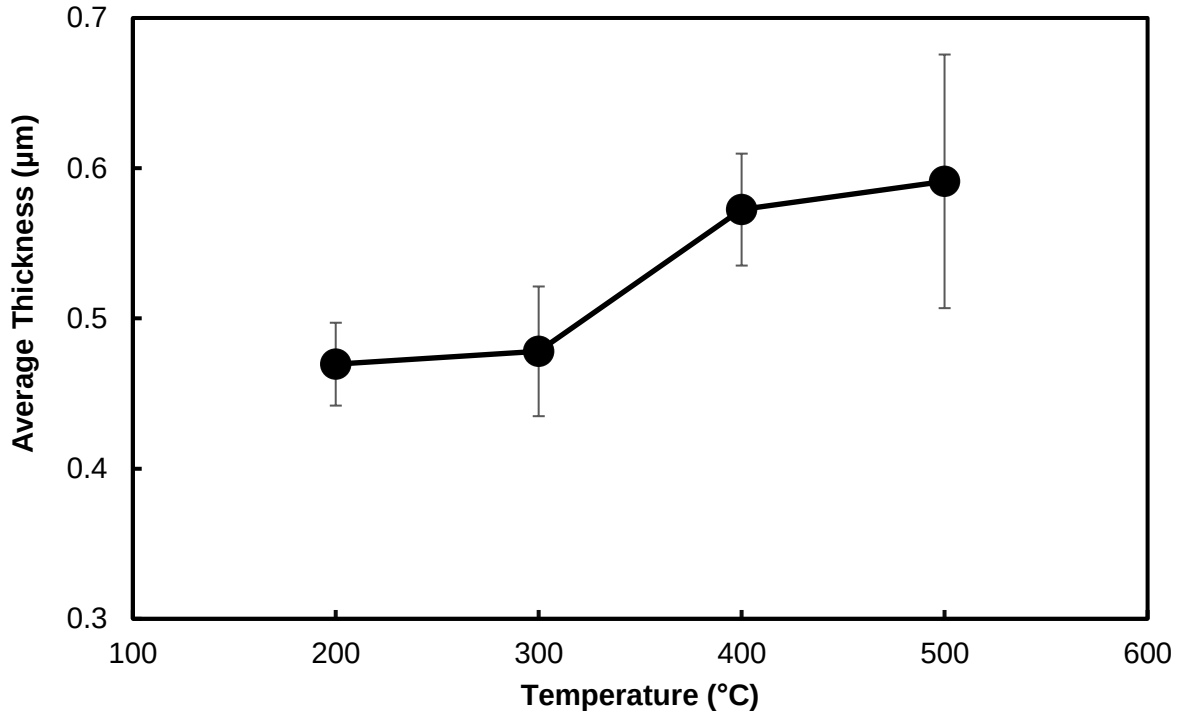

Figure 6-18: Effect of the drying temperature on the average coating thickness on the coated fibre obtained by dip-coating a slurry containing P25 and using the AOFCCP under standard process condition (see Table 6.3).

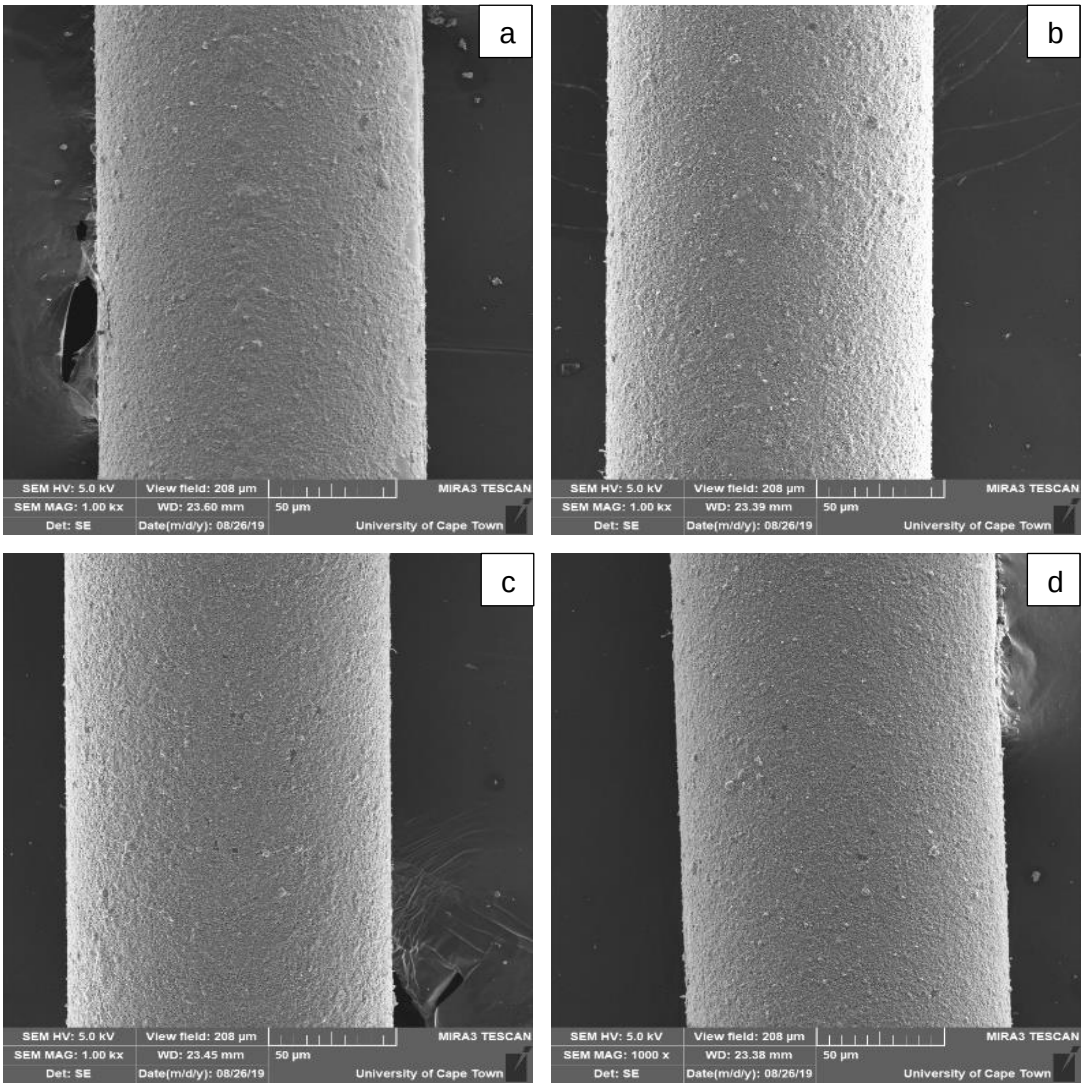

Figure 6-19: Surface morphology of the coated optical fibre by dip-coating in a slurry containing P25 slurry using AOFCCP at standard conditions (see Table 6.3), but varying calcination temperatures. (a) 200 °C, (b) 300 °C, (c) 400 °C, (d) 500 °C.

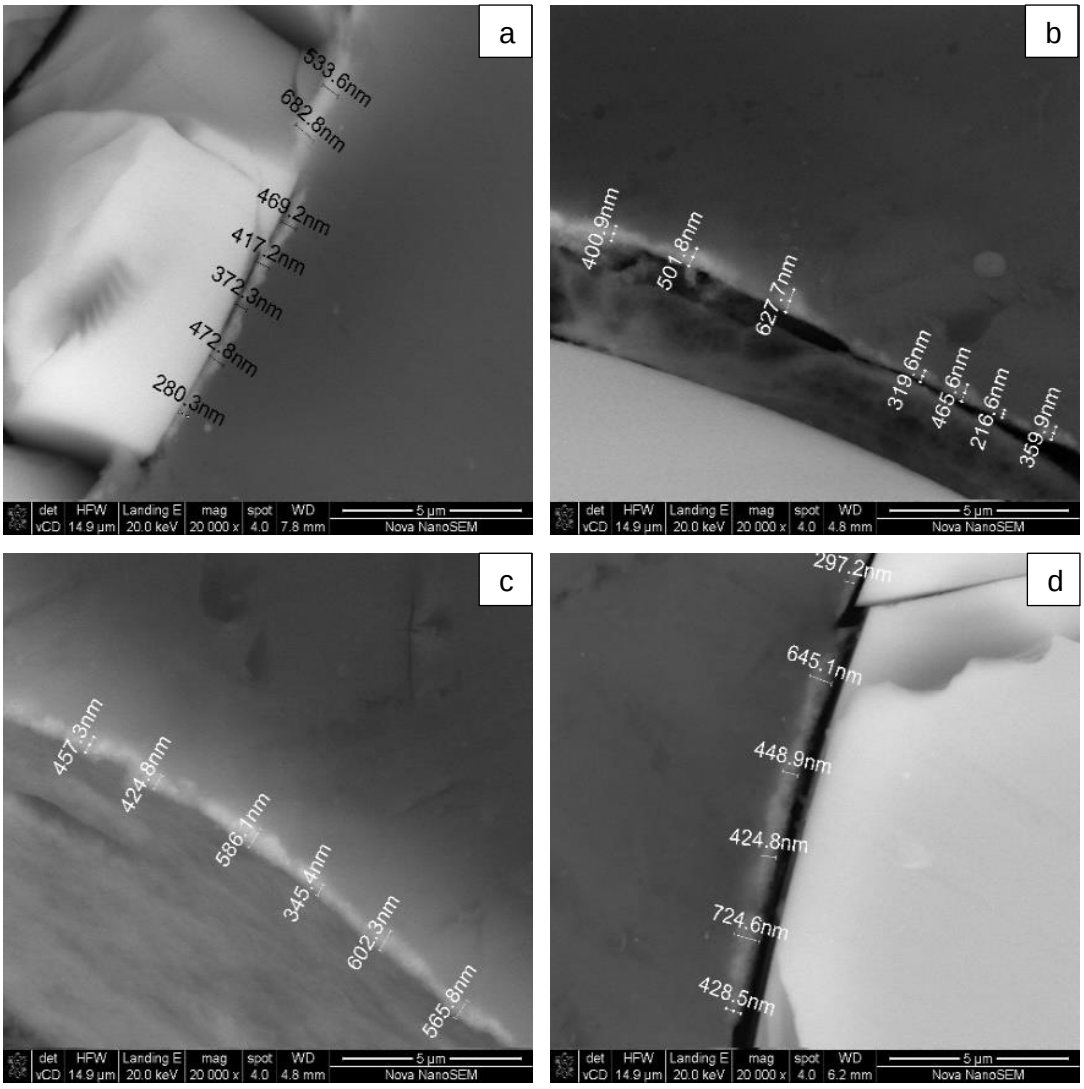

Figure 6-20: SEM image of the coated optical fibre by dip-coating in a slurry containing P25 at standard conditions (see Table 6.3), but varying calcination temperature. (a) 200 °C, (b) 300 °C, (c) 400 °C, (d) 500 °C.

6.4.2.3.1. Sol-gel coating

Calcination temperature is an important parameter in the sol-gel method and plays a role in the photoactivity and mechanical stability of the deposited film as it affects both the optical and structural properties of the TiO_2 film [79]. As discussed above, the calcination temperature used plays a role in determining the crystal phase of TiO_2 that is formed.

The results obtained from the study of the effect of calcination temperature on the surface morphology is shown in Figure 6-21. The surface coverage and homogeneity were good for the calcination temperatures of 400 °C and 500 °C, since smooth, homogeneous surfaces were observed with no coating deformations such as cracks. However, at 600 °C, crack formations were observed. The type of cracking is not consistent on the coated optical fibre calcined at 600 °C (see Figure 6-22).These cracks compromise the surface coverage and

homogeneity. This phenomenon might be due to the increased tension in the film due to the densification of the coating layer, which can cause random cracks on the surface of the coated optical fibre. Furthermore, the increase in furnace temperature may have resulted in a higher rate of evaporation resulting in a rapid change of mass on the surface of the optical fibre which may also contribute to the crack formations. Another possible cause for the cracking may be due to sudden exposure to a cooling environment since the thin films are susceptible to cracking if the thermal expansion coefficient exceeds that of the optical fibre [80]. The critical cracking temperature is thus determined to be 600 °C for the chosen process conditions.

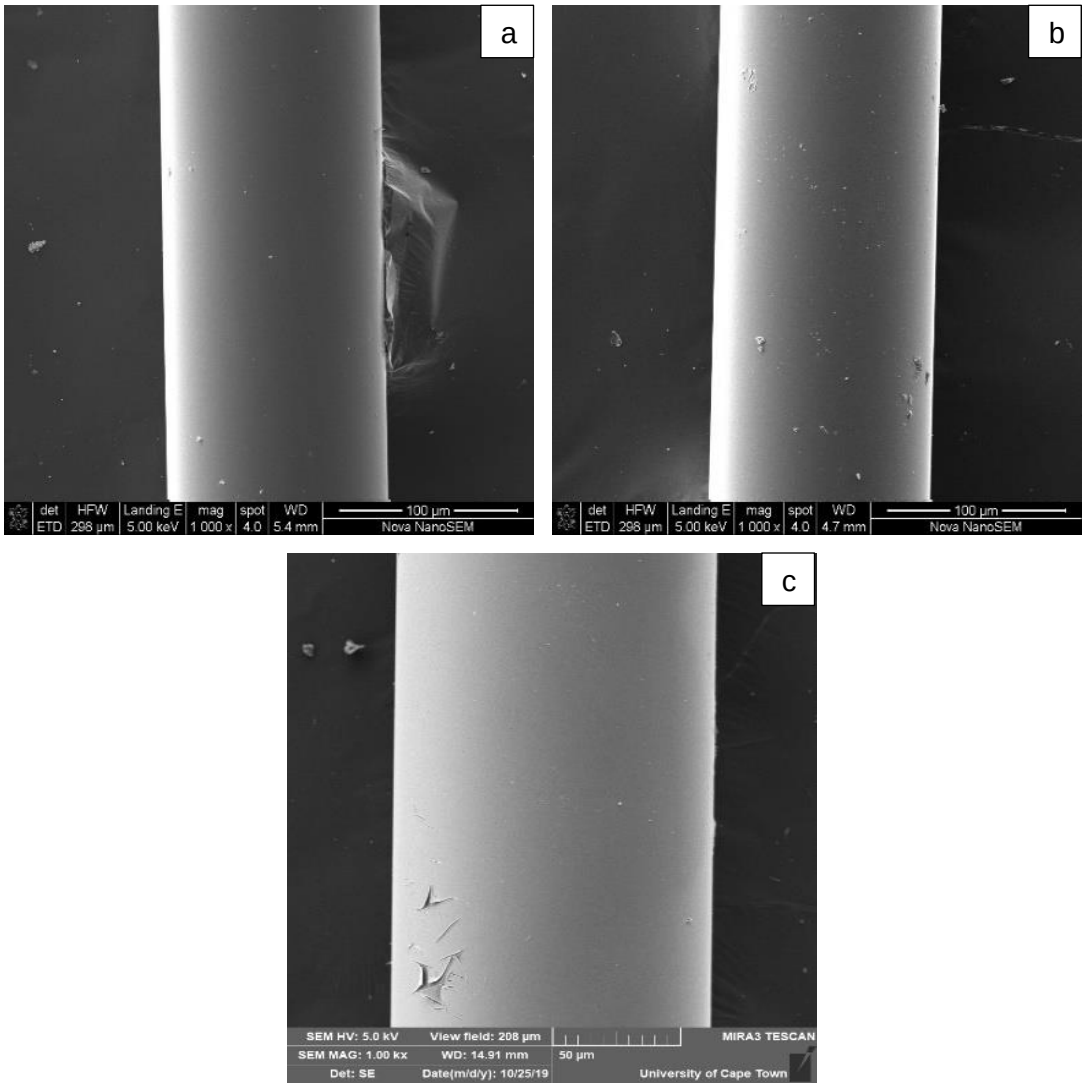

Figure 6-21: Surface morphology of the coated optical fibre by dip-coating of gel using AOFCCP at standard conditions (see Table 6.3) but varying calcination temperatures. (a) 400 °C, (b) 500 °C, (c) 600°C.

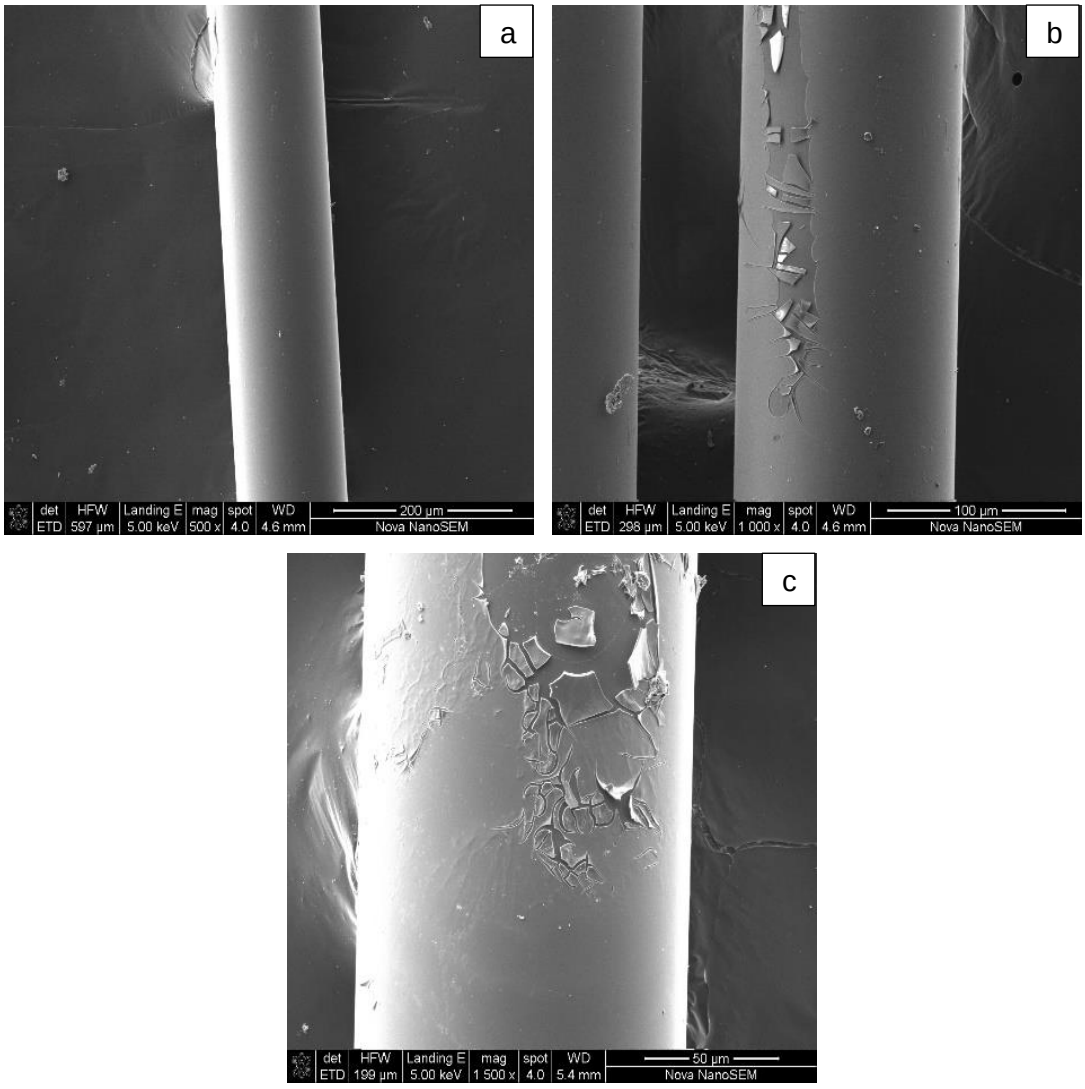

Figure 6-22: Surface morphology along the fibre length of coated optical fibre by dip-coating of gel using AOFCCP at a pulling speed of 1.15 mm·s^{-1} and a calcination temperature of 600 ºC . (a) Smooth high coverage coating, (b) Long scrape crack and (c) Cracking in a localised area of the coating.

Since the desired crystal phase is anatase, a temperature range of between 400 - 600 °C was chosen. The experiments were carried out using the AOFCCP at the standard pulling speed of 1.15 mm·s^{-1} with only the calcination temperature being varied. The results obtained are shown below in Figure 6-23.

The average film thickness decreased with an increase in calcination temperature. The highest average thickness (0.47 µm) was obtained at 400 °C. Both Chen and Dionysiou. [79], and Jin *et al*. [70] reported a decrease in porosity of TiO_2 films with an increase in calcination temperature which is caused by the shrinkage and the densification of the catalyst films. Therefore, it might be suggested that the average film thickness of the TiO_2 film on the optical fibre decreased with an increase in calcination temperature due to the densification of the layer [70]. Moreover, the calcination temperature was shown to influence the crystallite size

[66,67]. An increase in the crystallite size with increasing calcination temperature results in a decrease of the specific surface area which in turn reduces the photoactivity. Thus, high calcination temperatures should be avoided from that perspective. Figure 6-24, below, shows the SEM images that were taken of the cross-section area measuring the thickness of the catalyst layer for each experiment.

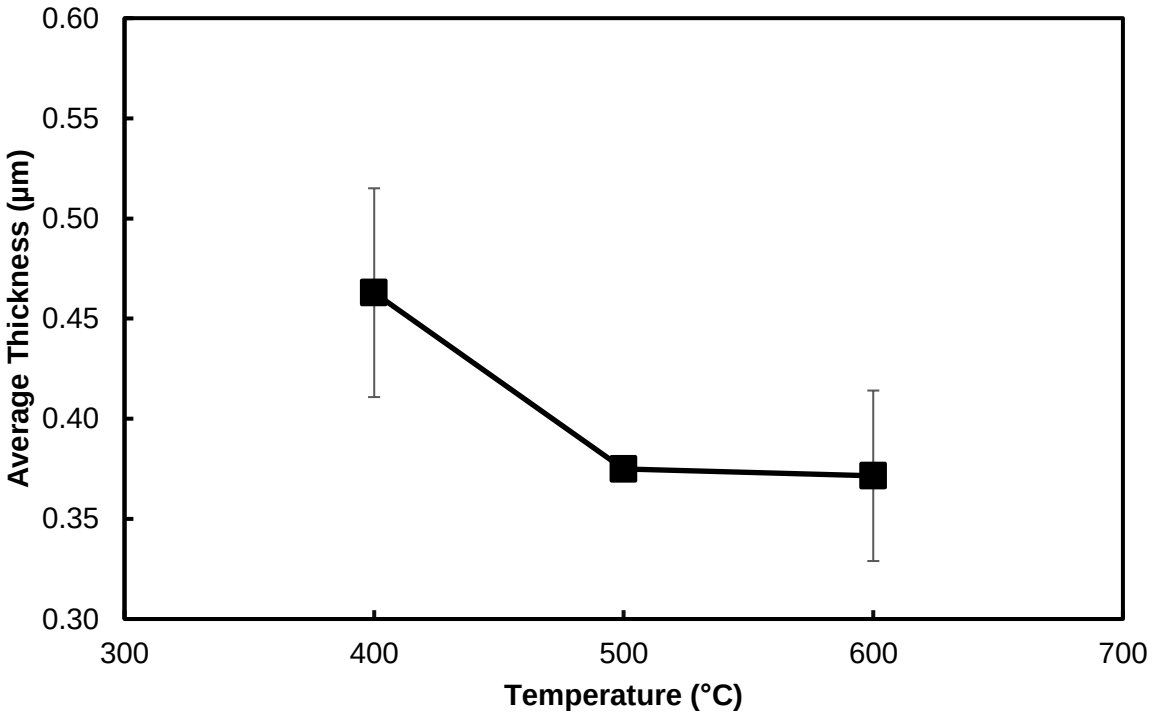

Figure 6-23: Effect of the calcination temperature on the average coating thickness achieved dip-coating in a gel using the AOFCCP under standard process condition (see Table 6.3).

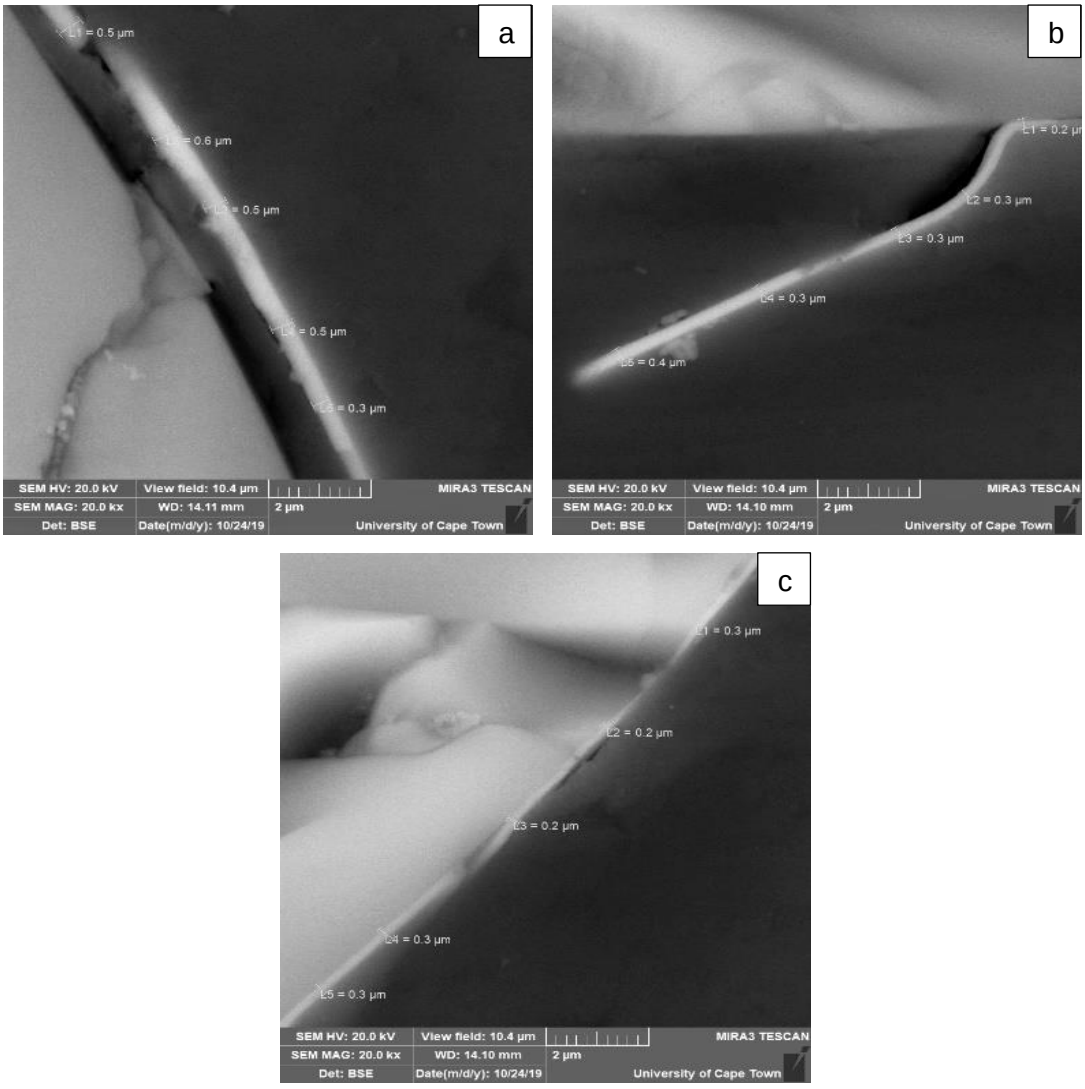

Figure 6-24: SEM of coated optical fibre obtained by dip-coating of gel using AOFCCP at standard process conditions (see Table 6.3), but varying calcination temperature. (a) 400 °C, (b) 500 °C, (c) 600 °C.

6.4.2.4. Effect of solid content in the slurry on coating morphology and thickness

The automated optical fibre catalyst coating process (AOFCCP) was used to determine how the concentration of the slurry containing P25 used in the dip-coating Unit 4, affects the homogeneity and thickness of the deposited TiO_2 layer.

The surface morphology was investigated using SEM in Figure 6-27. The surface coverage and homogeneity were evaluated for each slurry concentration investigated. The surface coverage and homogeneity for the experiments done using a solid content of 1 wt.-% is very poor (a). However, this improves significantly upon increasing the solid content to 10 wt.-% (b) and 15 wt.-% (c). The surfaces of these samples have high coverage and are homogenous in terms of particle sizes. There are minimal agglomerations on the surface. The improvement in surface coverage is possibly due to the TiO_2 particles being more tightly packed with an

increase in slurry concentration [81]. Sample (d), which was obtained using a slurry with a solid content of 20 wt.-%, showed poor to medium surface coverage and poor homogeneity, this can be seen by the variations in grey on the optical fibre surface – the brighter particles are the P25. The brighter the area, the thicker the coating. The darker areas represent the fused silica optical fibre surface. Therefore, despite the increase in thickness from 15 wt.-% to 20 wt.-%, the coverage and homogeneity were poor.

The highest achieved thickness was 0.89 µm, however, in order to achieve the best product with the highest catalyst layer thickness under the chosen standard process conditions, a solid content of 15 wt.-% is suggested as it achieves a thickness of 0.75 µm with high coverage and homogeneity by dip-coating in a slurry containing P25.

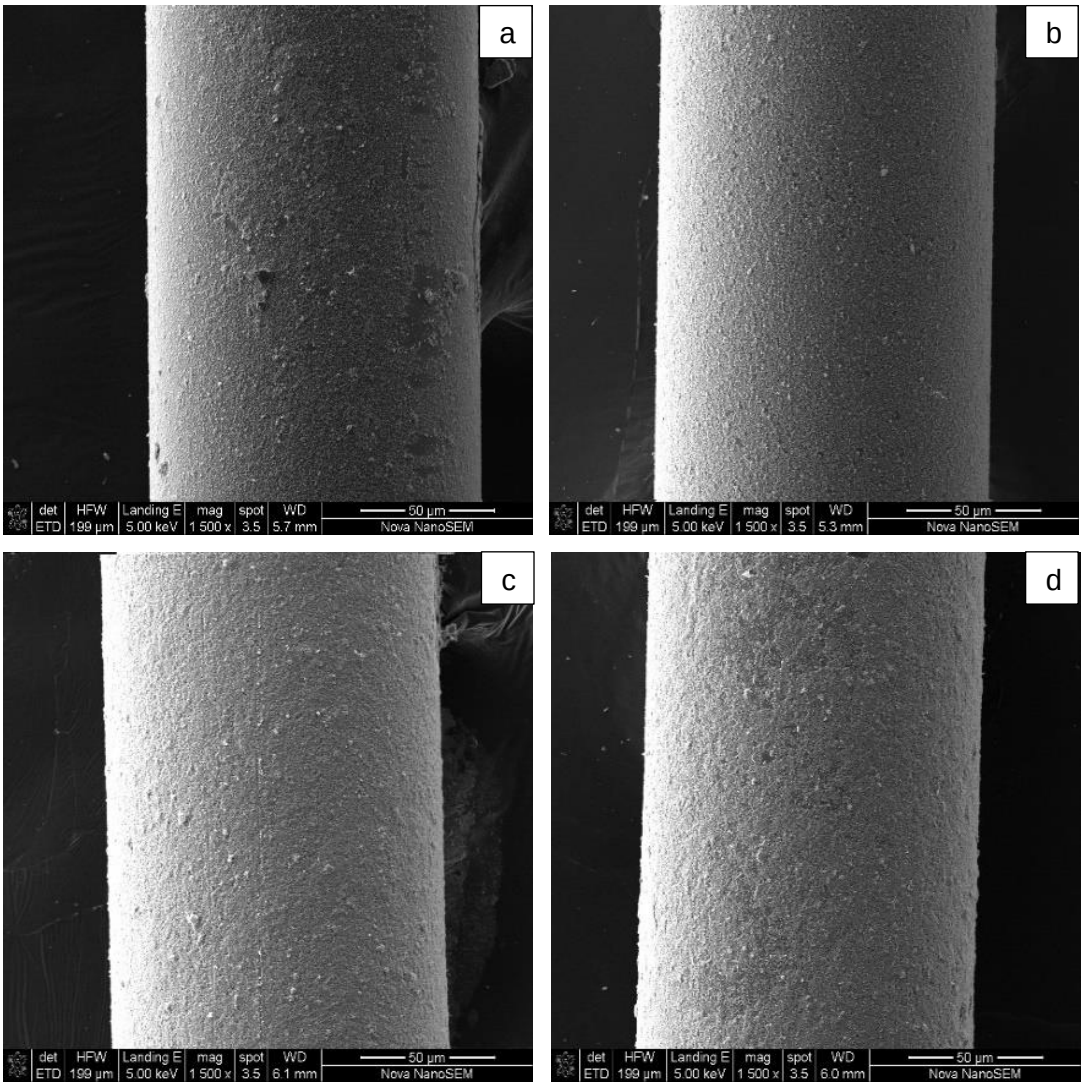

Figure 6-25:Coating morphology of the coated optical fibre by dip-coating in a slurry containing P25 at standard conditions (see Table 6.3) but varying solid contents. (a) 1 wt.-%, (b) 10 wt.-%, (c) 15 wt.-%, (d) 20 wt.-%

Figure 6-26 shows that the average thickness of the catalyst layer increases linearly with the solid content for a solid content of 5 wt.-% and higher with an R^2 value of 0.986. The trend obtained agreed with the work done by Peill and Hoffmann [15], which showed an increase in catalyst layer thickness with an increase in slurry concentration, however, there were differences in the catalyst layer thicknesses that were achieved in this experiment. For slurry concentrations of between 0.1 wt.-% - 10 wt.-% Peill and Hoffmann [15], achieved a catalyst coating thickness of less than 2.5 µm whereas in this project, as seen in Figure 6-26, the maximum thickness achieved at 10.wt-% was 0.62 µm. The average coating thicknesses achieved using the AOFCCP were higher than that achieved in literature [15]. This may be due to the differences in the preparation methods as well as the heat treatment method. The

linear increase in the thickness of the catalyst coating with an increase in the solid content of the dip-coating slurry is a consequence of the thicker initial saturated layer which is formed on the optical fibre [15]. Figure 6-27 illustrates the cross-sectional SEM images taken in order to measure the catalyst thickness for the various slurry concentrations that were investigated. Note that the images for the results obtained from the 5 wt.-% experiment were shown in the *standard process results* above in Figure 6-9. There is a deviation from the linear trend for low slurry concentrations, this is possibly due to measurements taken on samples with low coverage at 1 wt.-%. which is then completely covered at 5 wt.-%. Solid content at 5 wt.-% is sufficient for complete coverage of the surface with the same thickness. It is assumed the catalyst coating layer will increase in thickness only once the bare optical fibre surface is completely covered.

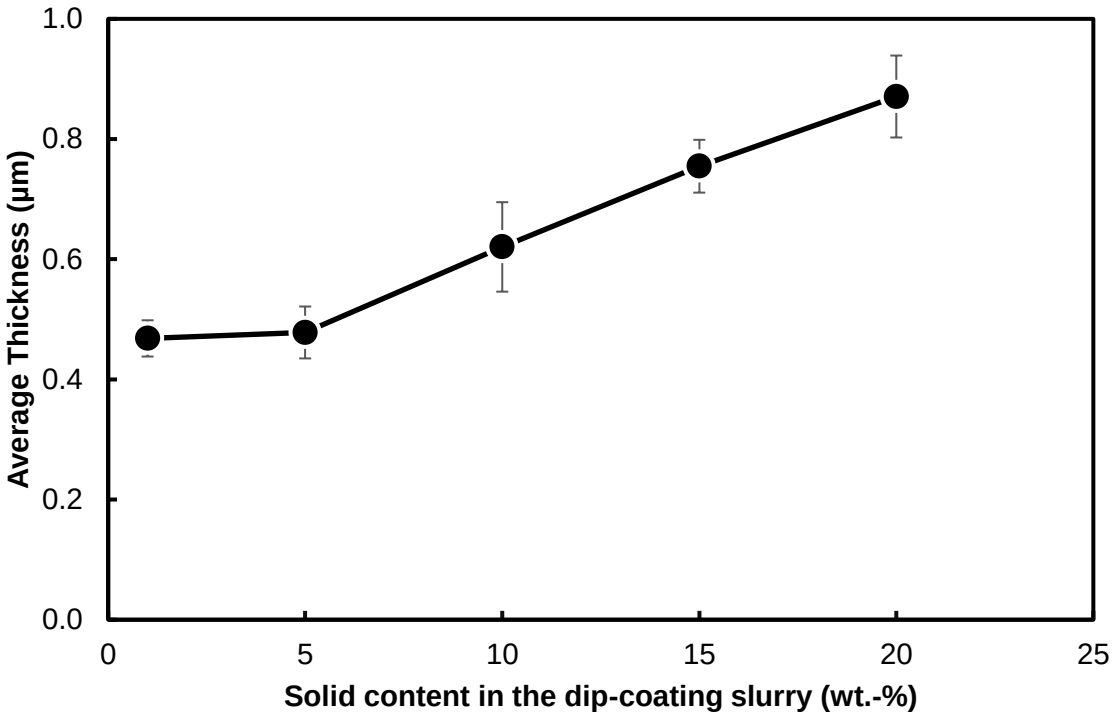

Figure 6-26: Effect of the solid content in the P25 slurry on the average coating thickness achieved using the AOFCCP under standard process condition (see Table 6.3).

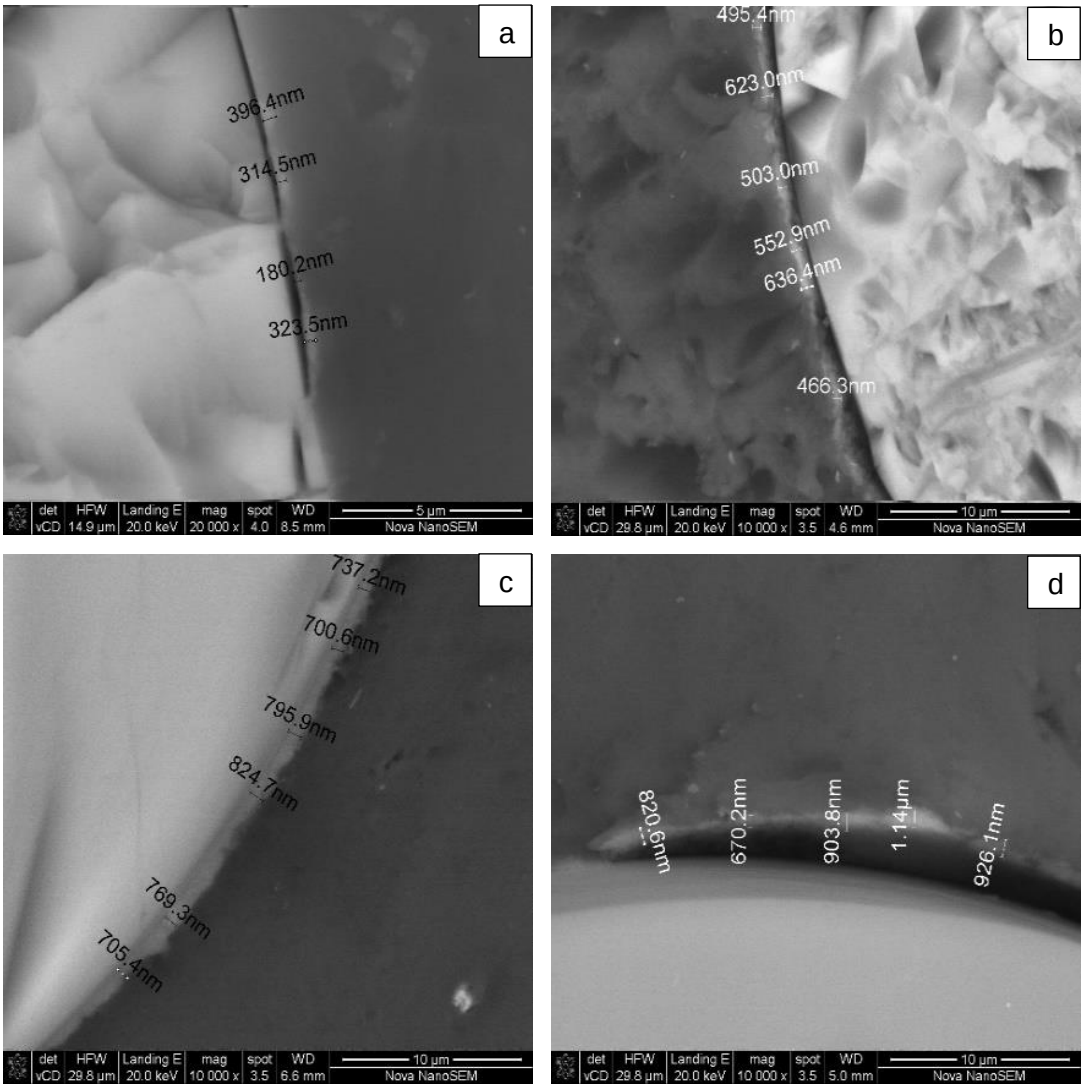

Figure 6-27: Coating thickness of the coated optical fibre by dip-coating in a slurry containing P25 at standard conditions (see Table 6.30) but varying solid content in the slurry. (a) 1 wt.-%, (b) 10 wt.-%, (c) 15 wt.-%, (d) 20 wt.-%.

6.4.2.5. Effect of slurry pH on coating morphology and thickness

The pH of the slurry was investigated as a process variable in the AOFCCP since coating using the slurry method dip-coating is governed by electrostatic interaction between the TiO_2 particles in solution and the fused silica optical fibre. It has been reported that the pH_{iep} for glass is 2 and the pH_{iep} for P25 is approximately 7.2, which makes the ideal pH operating range between 2-6 [55]. This range was investigated in order to determine if there is an optimal pH value within the operating range.

Figure 6-28, below, illustrates the SEM images taken of the surface of the coated optical fibre in order to evaluate the surface coating and homogeneity. It can be seen that the coverage for all 3 pH values that were investigated was moderate to high. Moreover, it can be seen that the homogeneity between the 3 samples was the same – the surfaces of the coating are corrugated, as expected, and there are minimal agglomerations. There were no significant differences between the samples with respect to surface coverage and homogeneity. Therefore, it can be concluded that the pH had no significant effect on the coating of the catalyst in the chosen operating range.

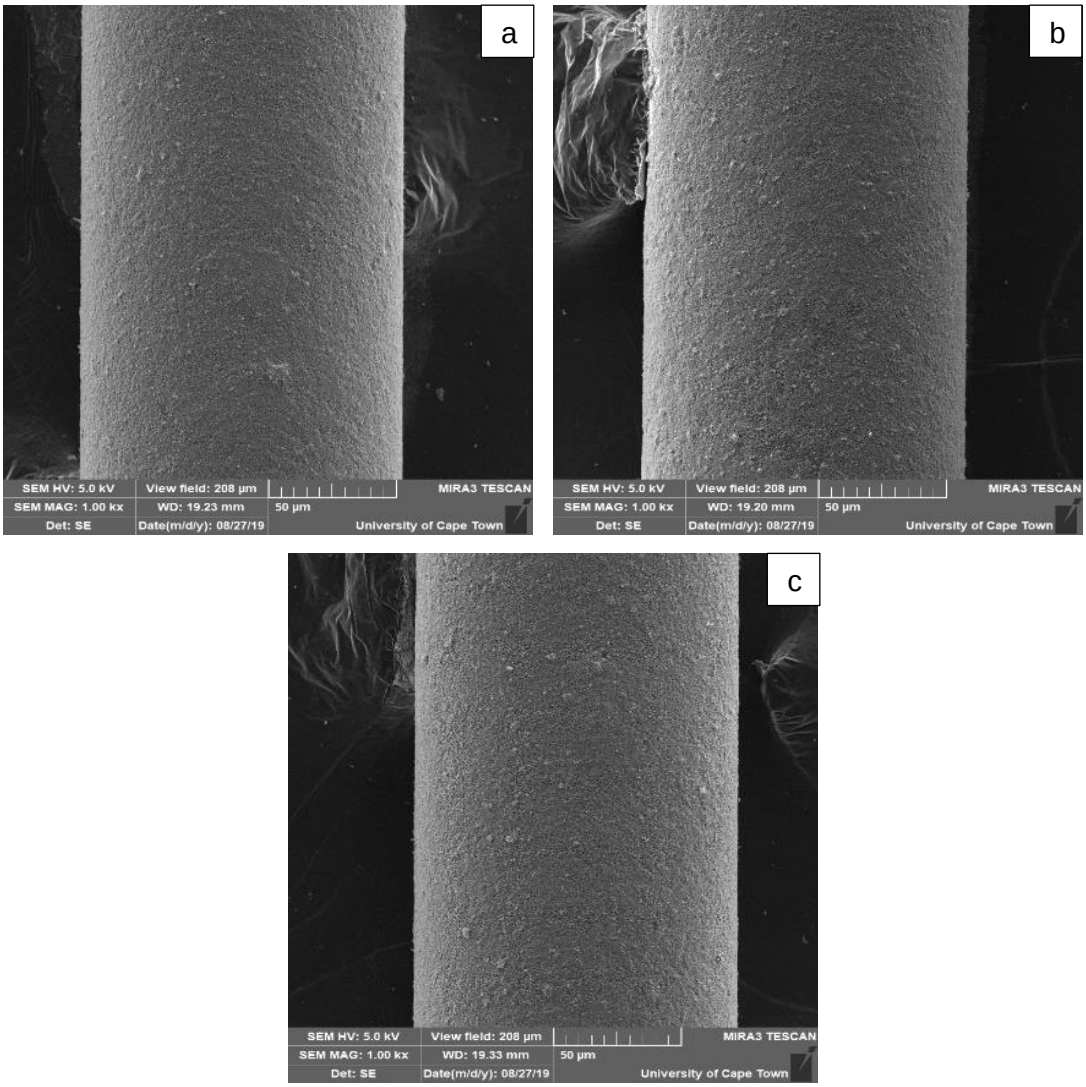

Figure 6-28: SEM of the coating morphology of the P25 slurry coated optical fibre for various slurry pH values that were investigated. (a) 2.65, (b) 3.65, (c) 5.65 under standard process condition of 1.15 mm.s^{-1}, 200°C and 5 wt.-%.

Figure 6-29 displays the relationship between the coating thickness and the pH. Therefore, despite the slight decrease in coating thickness the gradient of the line is approximately zero, reinforcing the fact that there is no relationship between pH and coating thickness, thus indicating that the change in pH had no significant effect on the coating thickness. Figure 6-30 shows the SEM images taken for the coating thickness measurements on the cross-section of the optical fibre.

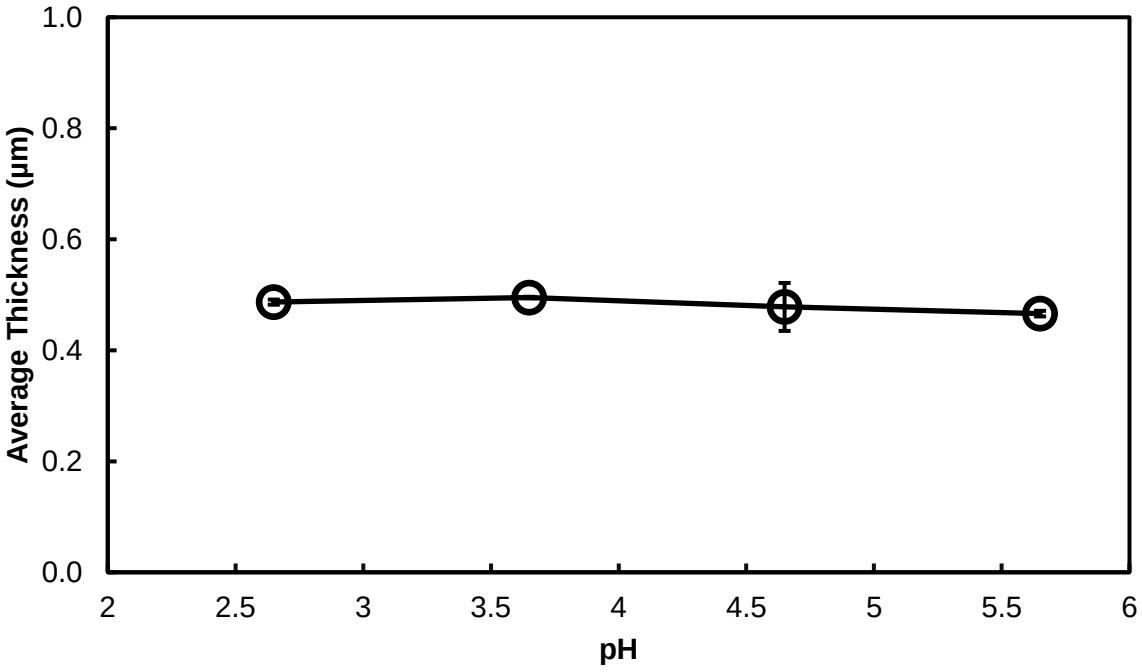

Figure 6-29: Effect of the pH of the slurry containing P25 on the average coating thickness achieved using the AOFCCP under standard process conditions (see Table 6.3).

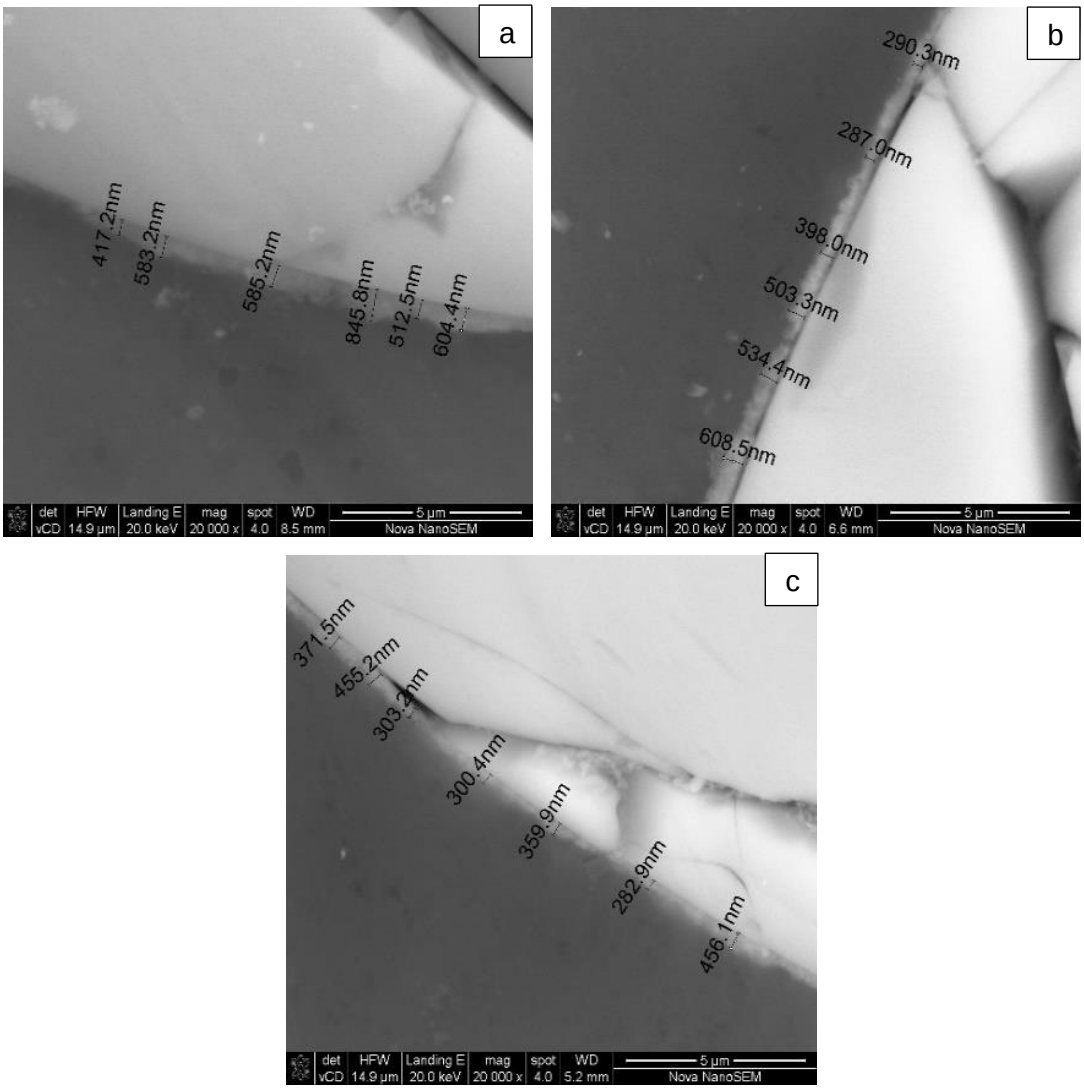

Figure 6-30: SEM of the coating thickness of the P25 slurry coated optical fibre for various slurry pH values that were investigated. (a) 2.65, (b) 3.65, (c) 5.65 under standard process condition of 1.15 mm.s^{-1}, 200°C and 5 wt.-%.

7. Discussion

7.1. Effect of pulling speed on coating thickness and surface morphology for sol-gel and P25 methods

The pulling speed ranges that were investigated for both the sol-gel and the P25 coating methods were the same: 1.15 to 3.45 $mm{\cdot}s^{-1}$. The change in pulling speed alters the withdrawal speed of the optical fibre from the catalyst bath and the residence time of the optical fibre in the oven. The principal of the coating formation for the dip-coating process is the same for both the dip-coating in a slurry containing P25 and dip-coating a gel [77], [79]. The factors that affect the formation of the coating on the optical fibre discussed previously are the entraining and draining forces as well as the drying rates. The entraining forces allow the liquid to be entrained onto the substrate as it is withdrawn from the coating medium whereas the draining force is gravitational draining. Therefore, an increase in withdrawal speed decreases the time in which gravitational draining can occur thus a thicker catalyst coating is formed [51].Furthermore, the increase in pulling speeds decreases the residence drying times which results in the drying to be dominated by constant rate drying. The thickness of the catalyst coating layer will, therefore, be dependent on the initial thickness entrained on the optical fibre as it is withdrawn from the coating medium. The reverse is expected for slow pulling speeds, as the coating formation is governed by gravitational draining resulting in a decrease in catalyst coating thickness. Due to the increased residence drying time, the falling film drying period is dominated which allows for improved evaporation which results in a decrease in catalyst coating thickness.

The thicknesses that were achieved in the automated optical fibre catalyst coating process (AOFCCP) can be compared for the same range of pulling speeds. Lower coating thickness was obtained by dip-coating the gel (0.23 µm – 0.37 µm) than by dip-coating a slurry containing P25 (0.41 µm – 0.47 µm) at a pulling speed of 0.11 $mm{\cdot}s^{-1}$ or 0.15 $mm{\cdot}s^{-1}$ showed. For both coating methods, an operating speed of 1.72 $mm.s^{-1}$ achieved an average coating thickness of approximately 0.52 µm. The average coating thicknesses obtained by dip-coating the P25 slurry showed a gradual increase upon further increasing the pulling speed whereas the average thickness by dip-coating the gel showed a rapid increase. However, based on the statistical analysis done to determine the extent of the uniformity and precision in the results, it was concluded that at least 1 of the triplicate experiments that was run was unreliable with a standard deviation of greater than 30%. Therefore, the results obtained for the sol-gel method at these high speeds of 2.88 $mm{\cdot}s^{-1}$ and 3.46 $mm{\cdot}s^{-1}$ should not be considered. The high uncertainty in these measurements is possibly due coating deformations such as cracking

of the coating layers which cause large deviation in the measured thicknesses across the coated optical fibre. Both methods showed an increase in thickness with pulling speed [77]. The differences in the thickness are a result of the differences in the formation of the coating during the dip-coating process discussed in the results section above.

The coating morphology for both P25 showed high surface coverage and homogeneity for 3.45 $mm.s^{-1}$. The surface of the coating appeared to be rough and corrugated with minor agglomerations. The sol-gel coating morphology showed high surface coverages and homogeneity for speeds up to 1.72 $mm.s^{-1}$ Withdrawal speeds between 1.73 $mm{\cdot}s^{-1}$- 3.46 $mm{\cdot}s^{-1}$ produce coatings which were susceptible to cracking.

7.2. Effect of drying temperature on coating thickness and surface morphology for sol-gel and P25 methods

The temperature range of the final heat treatment of the coating that was investigated for both coating methods differed as they played a different role in the coating formation process. The heat treatment after dip-coating the slurry containing P25 was used entirely for drying the TiO_2 on the optical fibre. The heat treatment after dip-coating the gel was used primarily for the calcination of the gel layer into an anatase layer. Unlike the pulling speed, the temperature had a different effect on the two different coating methods. The thickness of the coating increased with drying temperature between 200 °C and 500 °C when dip-coating a slurry containing P25. This may be due to a higher evaporation rate causing faster drying and less gravitational drainage of the slurry. This is in contrast to the effect that temperature had when dip-coating a gel. Here the thickness of the coating decreased with an increase in temperature, which was thought to be related to the densification of the film causing a decrease in porosity in the film.

The form of drying differed between the coating methods. The heat treatment following dip-coating of the slurry containing P25 was dominated by the constant rate drying period since drying due to diffusion was negligible due to the fast evaporate of water at the temperatures investigated (200 °C and 500 °C) The constant rate drying period and falling rate drying period played an important role heat treatment after dip-coating a gel. It controls the thickness of the layer, and if exceeding ca. 700 ºC even the crystal phase of TiO_2 that was formed.

The coating morphology remained constant for the P25 slurry method, which produced coated optical fibre with high surface coverages and homogeneity and achieved thickness in the 0.47 µm - 0.59 µm range. Whereas, the quality of the coating was compromised for the sol-gel method at a temperature of 600 °C due to deformations in the form of cracking. Between

400 °C and 500 °C, the coating appeared to have high coverage and homogeneity. For the temperature range investigated, the average coating thickness ranged between 0.45 µm to 0.37 µm from 400 °C to 500 °C, respectively.

7.3. Overall operational function

The overall operational function of the system for both coating methods were assessed by the ability to meet design requirement: "*Ability to achieve controllable catalyst coating thickness of 0.4 µm – 1.1 µm on the optical fibre*". Based on the experiments performed, it has been determined that the sol-gel method is a possible method to achieve this design requirement. The system is limited to speeds less than 2.8 $mm \cdot s^{-1}$ due to the inconsistency in the uniformity of the coating layer. Further investigations are required for confirmation. Average coating thicknesses of below 0.4 µm can also be achieved using the sol-gel method. It was confirmed that it is possible to control the coating thickness by the manipulation of the process conditions of both the temperature and pulling speed.

It was observed that adjusting the temperature is only ideal for achieving small changes in the coating thickness, whereas slurry concentration can be used to obtain larger changes in the coating thickness. Results of the slurry concentration relationship showed a larger increase in thickness with an increase in slurry concentration in comparison to the increase in thickness by an increase in temperature. The pH of the slurry showed no effect on the thickness and the surface coating morphology and therefore not a significant process variable. It should just be maintained and monitored in order to ensure electrostatic attraction between the optical fibre and the TiO_2 particles. According to the results obtained by the study of the average coating thickness and pulling speeds for both sol-gel and P25 slurry method, it is possible to achieve thickness below 0.4 µm or above 1 µm by further investigation of the pulling speeds below 0.12 $mm \cdot s^{-1}$ [77]. This is possible as the lowest achievable speed is 0.0015 $mm \cdot s^{-1}$. Based on the results obtained from the entire study on the effect of the various process variables having on the average coating thickness, it can be concluded that it is possible to achieve a wide variety of thickness by using various combinations of the process variables.

8. Conclusion

The automated optical fibre catalyst coating process (AOFCCP) that was proposed was designed constructed and commissioned to include the 4 optical fibre preparation steps in an automated process. This was done in order to coat optical fibre for a novel photoreactor which should consist of approximately 18 000 pieces of coated optical fibre (each of a length of 10 cm) allowing to have a catalyst loading of 1 g. Since the catalyst coating thickness has been reported to affect the light attenuation and distribution in the optical fibre and therefore the photoreactor, it was vital that the process was able to produce controllable coating thicknesses on the optical fibre.

The AOFCCP was commissioned for two coating methods namely the dip-coating a titania containing gel (prepared using sol-gel technique) and dip-coating a slurry containing P25. This system produced controllable thicknesses of between 0.2 µm - 0.8 µm for the sol-gel method and 0.4 µm - 0.7 µm for the P25 method. Dip-coating a titania containing gel, results after the heat treatment in anatase on the surface of the optical fibre as confirmed using Raman. The required time for the heat treatment was between 1.45 minutes to 43.41 minutes, which is reduction in the calcination time, from that typically reported in literature for transforming the gel into anatase by 85.5 % - 99.5% [1,6].

Various process variables were investigated for their effect on the homogeneity and thickness of the coating, such as were temperature of heat treatment and pulling speeds for both dip-coating methods, and the pH and slurry concentration of the P25 slurry in the dip-coating of a slurry containing P25. However, the pH of the slurry showed to have no significant effect on either the thickness of the coating or the surface morphology.

From the commissioning process, it was shown that the pulling speed of the optical fibre through the system had a positive proportional relationship with the thickness of the coating on the optical fibre. For high withdrawal speeds of 2.30 $mm \cdot s^{-1}$ - 3.45 $mm \cdot s^{-1}$ coating was susceptible deformations.

The temperature of the final heat treatment had a different effect on the coating thickness for each of the methods. An increase in the temperature heat treatment after dip-coating the fibre in a slurry containing P25 showed an increase in thickness possibly due to higher evaporation rates and therefore reduced gravitational drainage. Dip-coating the fibre in a gel resulted in a decrease in film thickness with an increase in calcination temperature. This was ascribed to a decrease in porosity in the film. The critical cracking temperature was 600 °C for the chosen process conditions for sol-gel coating method and the temperature had no effect on the surface morphology of the P25 slurry coated optical fibre. The thickness of the catalyst layer

on the fibre was shown to increase with an increase in slurry concentration. Low coverage was reported for slurry concentration of 1 wt.-%. However, for slurry concentrations greater than 1% good surface morphology was observed.

Based on the results obtained during commissioning of the AOFCCP, it can be concluded that the thickness can be controlled within a ranges mentioned above which meets designed requirement 1.10 which states "*Ability to achieve controllable catalyst coating thickness of 0.4 µm – 1 µm on the optical fibre*" The established relationship between the process variables and the coating thickness and surface morphology can be adjusted using a combination of process variables in order to achieve thickness greater than or less than that obtained in the commissioning process.

9. Recommendations

The experiments performed using the AOFCCP showed good controllability and repeatability of the results, however sol-gel experiments performed at high speeds of 2.88 $mm \cdot s^{-1}$ and 3.46 $mm \cdot s^{-1}$ should be repeated in order to decrease the standard deviation and improve the precision and uniformity in the results obtained. The lower operating speed limit that was chosen in the project was 0.12 $mm \cdot s^{-1}$. Therefore, it is recommended that lower pulling speeds be tested in the system in order to determine the minimum achievable coating thickness. Ultra-slow speeds can be investigated since the design speed limit of the stepper motor in Unit 6 is 0.0012 $mm \cdot s^{-1}$.

The P25 slurry concentration had a significant effect on the thickness of the coating layer formed on the optical fibre, therefore since the dip-coating principles similar for both coatings investigated, it is recommended at the sol-concentration should also be investigated as a process variable in order to achieve improved controllability of the catalyst film formed. The highest repeatable achievable average thickness was 0.77 µm for the sol-gel method using a pulling speed of 2.30 $mm \cdot s^{-1}$ and 500 °C. Therefore, in order to achieve higher thicknesses closer to the design requirement of 1.1 µm, it is recommended that a combination of process variables together with the addition of thickeners be used to increase thickness of the coating on the optical fibre. Moreover, process variables operating range can be increased to determine it's extent on the coating thickness and surface morphology.

To improve the surface morphology, both coverage and homogeneity, it is recommended that surfactants such as Polyethylene Glycol (PEG) and trehalose be used to reduce coating deformations by producing thicker and more sturdier coating layers on the optical fibre. Furthermore, roller diameters can be increased in order to decrease the bending angle which may reduce coating deformations such as breakings and cracking. Lastly, determining the effect of the coating thickness on the light attenuation and distribution in the coated optical fibre should be pursued further in combination with reactor testing in order to determine the optimum coating thickness on the optical fibre.

10. References

[1] T. V. Nguyen and J. C. S. Wu, “Photoreduction of CO_2 in an optical-fiber photoreactor: effects of metals addition and catalyst carrier”, *Appl. Catal. A General*, **335**, 112–120, 2008.

[2] M. I. Litter, “Heterogeneous photocatalysis: transition metal ions in photocatalytic systems”, *Appl. Catal. B Environmental*, **23**, 89–114, 1999.

[3] H. C. Aran, D. Salamon, T. Rijnaarts, G. Mul, M. Wessling, and R. G. H. Lammertink, “Porous photocatalytic membrane microreactor (P2M2): a new reactor concept for photochemistry”, *J. Photochem. Photobiol. A Chem.*, **225**, 36–41, 2011.

[4] K. Hofstadler, R. Bauer, S. Novallc, and G. Heisler, “New reactor design for photocatalytic wastewater treatment with TiO_2 immobilized on fused-silica glass fibers: photomineralization of 4-chlorophenol”, *Environ. Sci. Technol.*, **28**, 670–674, 1994.

[5] W. Choi, J. Y. Ko, H. Park, and J. S. Chung, “Investigation on TiO_2-coated optical fibers for gas-phase photocatalytic oxidation of acetone”, *Appl. Catal. B Environmental*, **31**, 209–220, 2001.

[6] H. Lin and K. T. Valsaraj, “An optical fiber monolith reactor for photocatalytic wastewater treatment”, *J. Appl. Electrochem.*, **32**, 699–708, 2005.

[7] J. C. S. Wu, H. M. Lin, and C. L. Lai, “Photo reduction of CO_2 to methanol using optical-fiber photoreactor”, *Appl. Catal. A General*, **296**, 194–200, 2005.

[8] BP, “Statistical review of world energy”, 2019. [Online]. Available: https://www.bp.com/en/global/corporate/energy-economics/statistical-review-of-world-energy.html. [Accessed: 19-Jun-2019].

[9] J. G. J. Olivier and J. A. H. . Peter, “Trends in global CO_2 and total greenhouse gas emissions: 2018 report”, 2018.

[10] “Climate change indicators in the united states”, 2016.

[11] L. M. Pastrana-Martínez, A. M. T. Silva, N. N. C. Fonseca, J. R. Vaz, J. L. Figueiredo, and J. L. Faria, “Photocatalytic reduction of CO_2 with water into methanol and ethanol using graphene derivative–TiO_2 composites: effect of pH and copper(i) oxide”, *Top. Catal.*, **59**, 1279–1291, 2016.

[12] M. Efe, D. Kilinc, E. Onater-isberk, and T. Yelkenci, “Estimating the political , economic and environmental factors’ impact on the installed wind capacity development : a

system approach", *Renew. Energy*, **96**, 636–644, 2016.

[13] V. Nguyen and C. S. J. Wu, "Recent developments in the design of photoreactors for solar energy conversion from water splitting and CO_2 reduction", *Appl. Catal. A General*, **550**, 122–141, 2018.

[14] F. Galli, M. Compagnoni, D. Vitali, C. Pirola, C. L. Bianchi, A. Villa, L. Prati, I. Rossetti, "CO_2 photoreduction at high pressure to both gas and liquid products over titanium dioxide", *Appl. Catal. B Environmental*, **200**, 386–391, 2017.

[15] N. J. Peill and M. R. Hoffmann, "Development and optimization of a TiO_2-coated fiber-optic cable reactor: photocatalytic degradation of 4-chlorophenol", *Environ. Sci. Technol.*, **29**, 2974–2981, 1995.

[16] A. Mills and S. Le Hunte, "An overview of semiconductor photocatalysis", *J. Photochem. Photobiol. A Chem.*, **108**, 1–35, 1997.

[17] T. Van Gerven, G. Mul, J. Moulijn, and A. Stankiewicz, "A review of intensification of photocatalytic processes", *Chem. Eng. Process.*, **46**, 781–789, 2007.

[18] Y. N. Kavil, Y. A. Shaban, R. K. Al Farawati, M. I. Orif, M. Zobidi, and S. U. M. Khan, "Photocatalytic conversion of CO_2 into methanol over Cu-C TiO_2 nanoparticles under uv light and natural sunlight", *J. Photochem. Photobiol. A Chem.*, **347**, 244–253, 2017.

[19] S. N. Habisreutinger, L. Schmidt-mende, and J. K. Stolarczyk, "Photocatalytic reduction of co2 on TiO_2 and other semiconductors", *Angew. Chemie Int. Ed.*, **52**, 7372–7408, 2013.

[20] J. C. S. Wu, T. H. Wu, T. Chu, H. Huang, and D. Tsai, "Application of optical-fiber photoreactor for CO_2 photocatalytic reduction", *Top. Catal.*, **47**, 131–136, 2008.

[21] A. L. Linsebigler, G. Lu, and J. T. Yates, "Photocatalysis on TiO_2 surfaces: principles, mechanisms, and selected results", *Chem. Rev.*, **95**, 735–758, 1995.

[22] K. Rajeshwar, "Photoelectrochemistry and the environment", *J. Appl. Electrochem.*, **25**, 1067–1082, 1995.

[23] A. Sharma and B. K. Lee, "Photocatalytic reduction of carbon dioxide to methanol using nickel-loaded TiO_2 supported on activated carbon fiber", *Catal. Today*, **298**, 158–167, 2017.

[24] J. Low, B. Cheng, and J. Yu, "Surface modification and enhanced photocatalytic CO_2 reduction performance of tio2: a review", *Appl. Surf. Sci.*, **392**, 658–686, 2017.

[25] L. Yuan and Y. J. Xu, “Photocatalytic conversion of CO_2 into value-added and renewable fuels”, *Appl. Surf. Sci.*, **342**, 154–167, 2015.

[26] L. Liu and Y. Li, “Understanding the reaction mechanism of photocatalytic reduction of CO_2 with H_2O on TiO_2 -based photocatalysts : a review”, *Aerosol Air Qual. Res.*, **14**, 453–469, 2014.

[27] A. Olivo, E. Ghedini, M. Signoretto, M. Compagnoni, and I. Rossetti, “Liquid vs. gas phase CO_2photoreduction process: which is the effect of the reaction medium?”, *Energies*, 1–14, 2017.

[28] M. Anpo, H. Yamashita, Y. Ichihashi, and S. Ehara, “Photocatalytic reduction of CO_2 with H_2O on various titanium oxide catalysts”, *J. Electroanal. Chem.*, **396**, 21–26, 1995.

[29] M. E. Leblebici, G. D. Stefanidis, and T. Van Gerven, “Comparison of photocatalytic space-time yields of 12 reactor designs for wastewater treatment”, *Chem. Eng. Process.*, **97**, 106–111, 2015.

[30] A. Salinaro and N. Serpone, “Terminology, relative photonic efficiencies and quantum yields in heterogeneous photocatalysis. part i: suggested protocol”, *Pure Appl. Chem.*, **71**, 303–320, 1999.

[31] M. Qureshi and K. Takanabe, “Insights on measuring and reporting heterogeneous photocatalysis: efficiency definitions and setup examples”, *Chem. Mater.*, **29**, 158–167, 2017.

[32] O. Ola, M. Maroto-Valer, D. Liu, S. MacKintosh, C. W. Lee, and J. C. S. Wu, “Performance comparison of CO_2 conversion in slurry and monolith photoreactors using Pd and Rh- TiO_2 catalyst under ultraviolet irradiation”, *Appl. Catal. B Environmental*, **126**, 172–179, 2012.

[33] A. K. Ray, “Development of a new photocatalytic reactor for water purification”, *Catal. Today*, **40**, 73–83, 1998.

[34] M. Lazar, S. Varghese, and S. Nair, “Photocatalytic water treatment by titanium dioxide: recent updates”, *Catalysts*, **2**, 572–601, 2012.

[35] I. Rossetti, A. Villa, C. Pirola, L. Prati, and G. Ramis, “A novel high-pressure photoreactor for CO_2 photoconversion to fuels”, *R. Soc. Chem.*, **4**, 28883–28885, 2014.

[36] A. Lais, M. A. Gondal, M. A. Dastageer, and F. F. Al-Adel, “Experimental parameters affecting the photocatalytic reduction performance of CO_2 to methanol: a review”, *Int. J. Energy Res.*, **42**, 2031–2049, 2018.

[37] N. J. Peill and M. R. Hoffmann, “Chemical and physical characterization of a TiO_2-coated fiber optic cable reactor”, *Environ. Sci. Technol.*, **30**, 2806–2812, 1996.

[38] A. Danion, J. Disdier, C. Guillard, F. Abdelmalek, and N. Jaffrezic-Renault, “Characterization and study of a single- TiO_2-coated optical fiber reactor”, *Appl. Catal. B Environmental*, **52**, 213–223, 2004.

[39] H. O’Neal Tugaoen, S. Garcia-Segura, K. Hristovski, and P. Westerhoff, “Compact light-emitting diode optical fiber immobilized TiO_2 reactor for photocatalytic water treatment”, *Sci. Total Environ.*, **613–614**, 1331–1338, 2018.

[40] R. E. Marinangeli and D. F. Ollls, “Photoassisted heterogeneous catalysis with optical fibers”, *AIChE J.*, **23**, 415–426, 1977.

[41] W. Wang and Y. Ku, “The light transmission and distribution in an optical fiber coated with TiO_2 particles”, *Chemosphere*, **50**, 999–1006, 2003.

[42] P. C. P. Bouten, “Lifetime of pristine of optical fibres”, *PhD thesis, Tech. Univ. Eindhoven,* 1987.

[43] N. Gougeon, R. El Abdi, and M. Poulain, “Mechanical reliability of silica optical fibers”, **316**, 125–130, 2003.

[44] M. J. Matthewson, C. R. Kurkjian, and J. R. Hamblin, “Acid stripping of fused silica optical fibers without strength degradation”, *J. Light. Technol.*, **15**, 490–497, 1997.

[45] A. T. Taylort, M. J. Matthewson, and C. R. Kurkjian, “Strength degradation of silica fibers by acetone immersion”, *Proc SPIE*, **3848**, 108–114, 1999.

[46] A. Taylor and M. Matthewson, “Effect of ph on the strength and fatigue of fused silica optical fiber”, *Proc. 47th Int. Wire ∧ Cable Symp. Brussels, Belgium*, 874+880, 1998.

[47] S. R. Schmid and A. F. Toussaint, “Optical fiber coatings”, in *Specialty optical fibers handbook*, **30**, 2007, 95–118.

[48] C. Euvananont, C. Junin, K. Inpor, P. Limthongkul, and C. Thanachayanont, “TiO_2 optical coating layers for self-cleaning applications”, *Ceram. Int.*, **34**, 1067–1071, 2008.

[49] J. M. Peralta and E. Meza, “Mathematical modeling of a dip-coating process using concentrated dispersions”, 2016.

[50] A. Peltola, “Up-scaling plan for TiO_2 coating process”, *Bachelor’s thesis, Turku Univ. Appl. Sci.*, 2009.

[51] C. J. Brinker, “Dip coating”, in *Chemical Solution Deposition of Functional Oxide Thin Films (T. Schneider, R. Waser, M. Kosec, D. Payne, Eds)*, 2013, 233–261.

[52] X. Tang and X. Yan, “Dip-coating for fibrous materials : mechanism , methods and applications”, *J. Sol-Gel Sci. Technol.*, 378–404, 2017.

[53] S. R. Oh, T. C. Wong, C. Y. Tan, and K. Yao, “Fabrication of piezoelectric polymer multilayers on flexible substrates for energy harvesting”, *Smart Mater. Struct.*, **23**, 2014.

[54] L. Landau and B. Levich, “Dragging of a liquid by a moving plate”, *Acta Physicochem. U.R.S.S*, **17**, 1942–1955, 1942.

[55] Y. Gu and D. Li, “The ζ-potential of glass surface in contact with aqueous solutions”, *J. Colloid Interface Sci.*, **226**, 328–339, 2000.

[56] D. L. Liao, G. S. Wu, and B. Q. Liao, “Zeta potential of shape-controlled TiO_2 nanoparticles with surfactants”, *Colloids Surfaces A Physicochem. Eng. Asp.*, **348**, 270–275, 2009.

[57] T. Miki, K. Nishizawa, K. Suzuki, and K. Kato, “Preparation of nanoporous TiO_2 film with large surface area using aqueous sol with trehalose”, *Matter. Lett.*, **58**, 2751–2753, 2004.

[58] N. Negishi, K. Takeuchi, and T. Ibusuki, “Preparation of the TiO_2 thin film photocatalyst by the dip-coating process”, *J. Sol-Gel Sci. Technol*, **13**, 691–694, 1998.

[59] M. M. Renfrew and E. E. Lewis, “Polytetrafluoroethylene. heat resistant, chemically inert plastic”, *Ind. Eng. Chem.*, **38**, 870–877, 1946.

[60] J. R. Lee, D. Dhital, and D. J. Yoon, “Investigation of cladding and coating stripping methods for specialty optical fibers”, *Opt. Lasers Eng.*, **49**, 324–330, 2011.

[61] V. Rondinella and M. Matthewson, “Effect of chemical stripping on the strength and surface morphology of fused silica optical fiber”, *Proc. SPIE*, **2074**, 52–58, 1994.

[62] A. Š. Vuk, R. Ješe, B. Orel, and G. Draži˘, “The effect of surface hydroxyl groups on the adsorption properties of nanocrystalline TiO_2 films”, *Intern. J. Photoenergy*, **7**, 2005.

[63] K. G. U. Y. Vibulyaseak, W. Chiou, and M. Ogawa, “Preferential immobilisation of size-controlled anatase nanoparticles in mesopores”, *Chem. Commun*, **15**, 8442–8445, 2019.

[64] U. G. Akpan and B. H. Hameed, “The advancements in sol – gel method of doped- TiO_2 photocatalysts”, *Appl. Catal. A General*, **375**, 1–11, 2010.

[65] C. A. Lekelefac, J. Hild, P. Czermak, and M. Herrenbauer, “Photocatalytic active coatings for lignin degradation in a continuous packed bed reactor”, **2014**, 2014.

[66] N. Negishi and K. Takeuchi, “Preparation of TiO_2 thin film photocatalysts by dip coating”, 23–31, 2001.

[67] E. Molina, L. Rocha, C. B.L, K. Ciuffi, P. Calefi, and E. Nassar, “Preparation and study of the titanium oxide thin films doped with Tb^{3+} and Ce^{3+} ions”, *Rev. Mater.*, **17**, 931–938, 2012.

[68] G. Li, L. Li, J. Boerio-goates, and B. F. Woodfield, “High purity anatase TiO_2 nanocrystals : near room-temperature synthesis , grain growth kinetics , and surface hydration chemistry”, *J. Am. Chem. Soc*, **4127**, 8659–8666, 2005.

[69] D. Rafieian, W. Ogieglo, T. Savenije, and R. G. H. Lammertink, “Controlled formation of anatase and rutile TiO_2 thin films by reactive magnetron sputtering”, **097168**, 2017.

[70] D. Jin, S. Hong, S. Hoon, and E. Jung, “Influence of calcination temperature on structural and optical properties of TiO_2 thin films prepared by sol – gel dip coating”, *Mater. Lett.*, **57**, 355–360, 2002.

[71] M. Hamadanian and A. Majedi, “Preparation and characterization of s-doped TiO_2 nanoparticles , effect of calcination temperature and evaluation of photocatalytic activity”, *Mater. Chem. Phys.*, **116**, 376–382, 2009.

[72] A. Taherniya and D. Raoufi, “Crack-free TiO_2 thin film via sol-gel dip coating method : investigation on molarity effect”, *IOP Conf. Ser. Mater. Sci. Eng*, **340**, 012009, 2018.

[73] I. Strawbridge and P. F. James, “The thickness of sol-gel derived silica coatings prepared by dipping”, *J. Non-Crystalline Solids*, **86**, 381–393, 1985.

[74] D. Grosso and P. Marie, “How to exploit the full potential of the dip-coating process to better control film formation”, 17033–17038, 2011.

[75] E. Bindini *et al.*, “The critical role of the atmosphere in dip-coating process”, *J. Phys. Chem. C*, **121**, 14572–14580, 2017.

[76] M. Guglielmi and S. Zenezini, “The thickness of sol-gel slica coatings obtained by dipping”, *J. Non-Crystalline Solids*, **121**, 303–309, 1990.

[77] D. Grosso and P. Marie, “How to exploit the full potential of the dip-coating process to better control film formation”, *J. Mater. Chem.*, 17033–17038, 2011.

[78] M. Guglielmi, P. Clomb, F. Peron, L. Mancinelli, and D. Esposti, “Dependence of

thickness on the withdrawal speed for SiO_2 and TiO_2 coatings obtained by the dipping method", *J. Mater. Sci.*, **27**, 5052–5056, 1992.

[79] Y. Chen and D. D. Dionysiou, "Effect of calcination temperature on the photocatalytic activity and adhesion of TiO_2 films prepared by the p-25 powder-modified sol – gel method", *J. Mol. Catal. A Chem.*, **244**, 73–82, 2006.

[80] Z. C. Xia and J. W. Hutchinson, "Crack patterns in thin films", *J. Mech. Phys. Solids*, **48**, 1107–1131, 2000.

[81] K. Suttiponparnit, J. Jiang, M. Sahu, and S. Suvachittanont, "Role of surface area , primary particle size , and crystal phase on titanium dioxide nanoparticle dispersion properties", *Nanoscale Res. Lett*, **6**, 27, 2011.

11. Appendices

A.1. Appendix: Statistical analysis

Table 11-1: Standard deviation showing coating uniformity and precision per run as well as repeatability per set for the P25 slurry coating method investigating pulling speed

Coating Method :	P25 slurry dip-coating			
Process Variable:	Pulling Speed (mm.s^{-1})			
	Standard Deviation			
	Run 1	Run 2	Run 3	Per Set
0.12	10%	19%	8%	8%
0.58	11%	11%	19%	5%
1.15	11%	14%	13%	4%
1.73	9%	17%	11%	5%
2.30	15%	15%	10%	4%
2.88	15%	18%	16%	2%
3.46	13%	17%	11%	1%

Table 11-2: Standard deviation showing coating uniformity and precision per run as well as repeatability per set for the P25 slurry coating method investigating drying temperature

Coating Method :	P25 slurry dip-coating			
Process Variable:	Drying temperature (°C)			
	Standard Deviation			
	Run 1	Run 2	Run 3	Per Set
200	11%	14%	13%	3%
300	10%	13%	12%	4%
400	13%	12%	15%	4%
500	13%	11%	13%	8%

Table 11-3: Standard deviation showing coating uniformity and precision per run as well as repeatability per set for the P25 slurry coating method investigating slurry concentration.

Coating Method :	P25 slurry dip-coating			
Process Variable:	Slurry Concentration wt.-%			
	Standard Deviation			
	Run 1	Run 2	Run 3	Per Set
1	11%	14%	13%	3%
5	11%	14%	13%	4%
10	12%	13%	16%	7%
15	27%	14%	21%	4%
20	13%	29%	26%	7%

Table 11-4: Standard deviation showing coating uniformity and precision per run as well as repeatability per set for the P25 slurry coating method investigating pH of slurry

Coating Method :	P25 slurry dip-coating			
Process Variable:	**pH of Slurry**			
Standard Deviation				
	Run 1	Run 2	Run 3	Per Set
2.65	13%	15%	16%	0%
3.65	14%	16%	25%	0%
4.65	11%	14%	13%	4%
5.65	13%	12%	11%	1%

Table 11-5: Standard deviation showing coating uniformity and precision per run as well as repeatability per set for the sol-gel coating method investigating pulling speed.

Coating Method :	Sol-gel dip-coating			
Process Variable:	**Pulling Speed ($mm.s^{-1}$)**			
Standard Deviation				
	Run 1	Run 2	Run 3	Per Set
0.12	13%	12%	11%	1%
0.58	11%	10%	15%	1%
1.15	18%	10%	25%	0%
1.73	18%	14%	11%	1%
2.30	22%	15%	14%	4%
2.88	35%	26%	30%	3%
3.46	64%	77%	89%	9%

Table 11-6: Standard deviation showing coating uniformity and precision per run as well as repeatability per set for the sol-gel coating method investigating calcination temperature

Coating Method :	Sol-gel dip-coating			
Process Variable:	**Calcination temperature (°C)**			
	Standard Deviation			
	Run 1	Run 2	Run 3	Per Set
400	8%	12%	15%	5%
500	18%	10%	25%	0%
600	10%	13%	17%	4%

Table 11-7: Standard deviation showing significance of the process variable on the coating thickness.

P25 Slurry dip-coating	
Pulling Speed (mm.s-1)	12%
Drying temperature (°C)	6%
Slurry Concentration (wt.-%)	18%
pH of Slurry	1%
Sol-gel dip-coating	
Pulling Speed (mm.s-1)	67%
Calcination temperature (°C)	5%

B.1. Appendix: Raman mapping results

Effect of calcination temperature

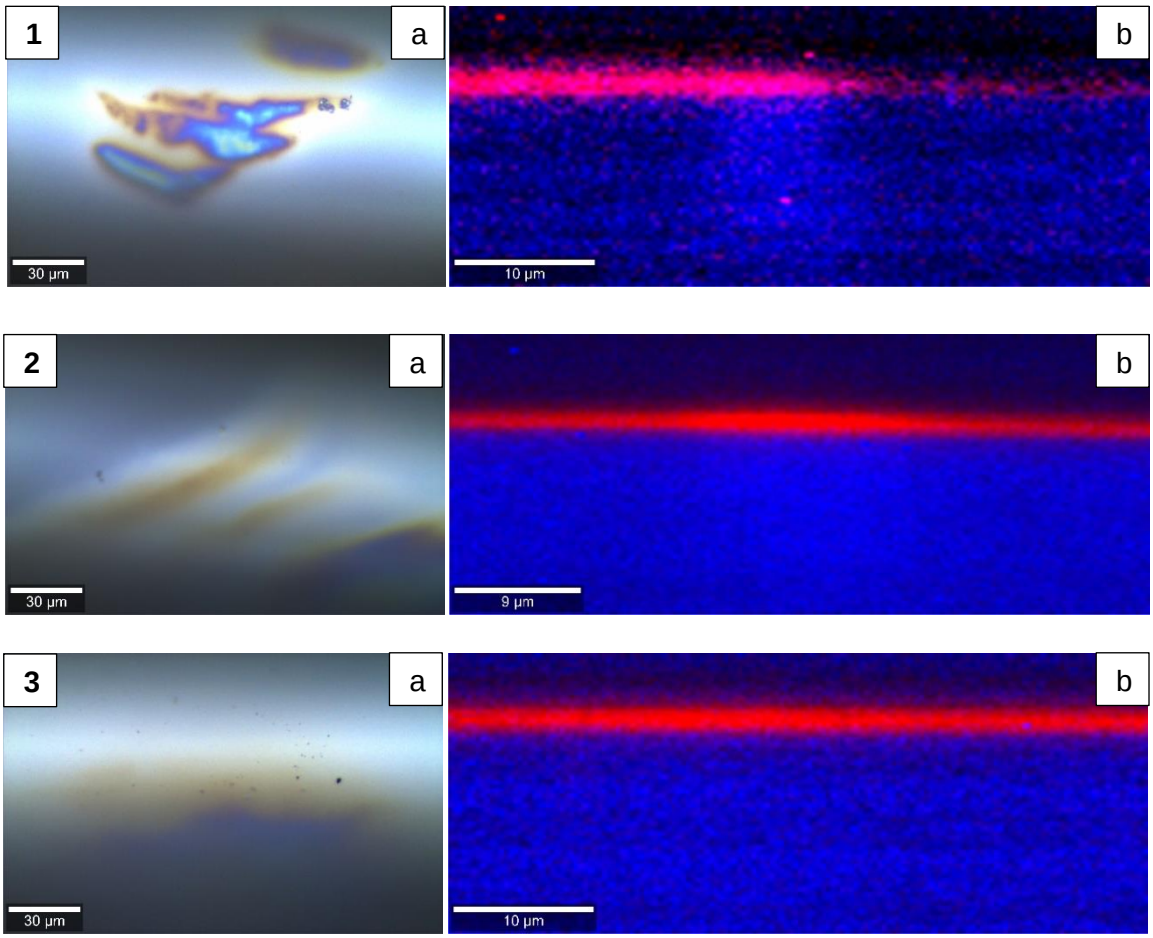

Figure 11-1: : (a) Sample maps, (b) Raman map of coated optical fibre surface showing anatase layer (red) on the fused silica optical fibre (blue). Sample collect at process conditions of 1.15 mm.s^{-1} and (1) 400°C, (2) 500°C and (3) 600°C .

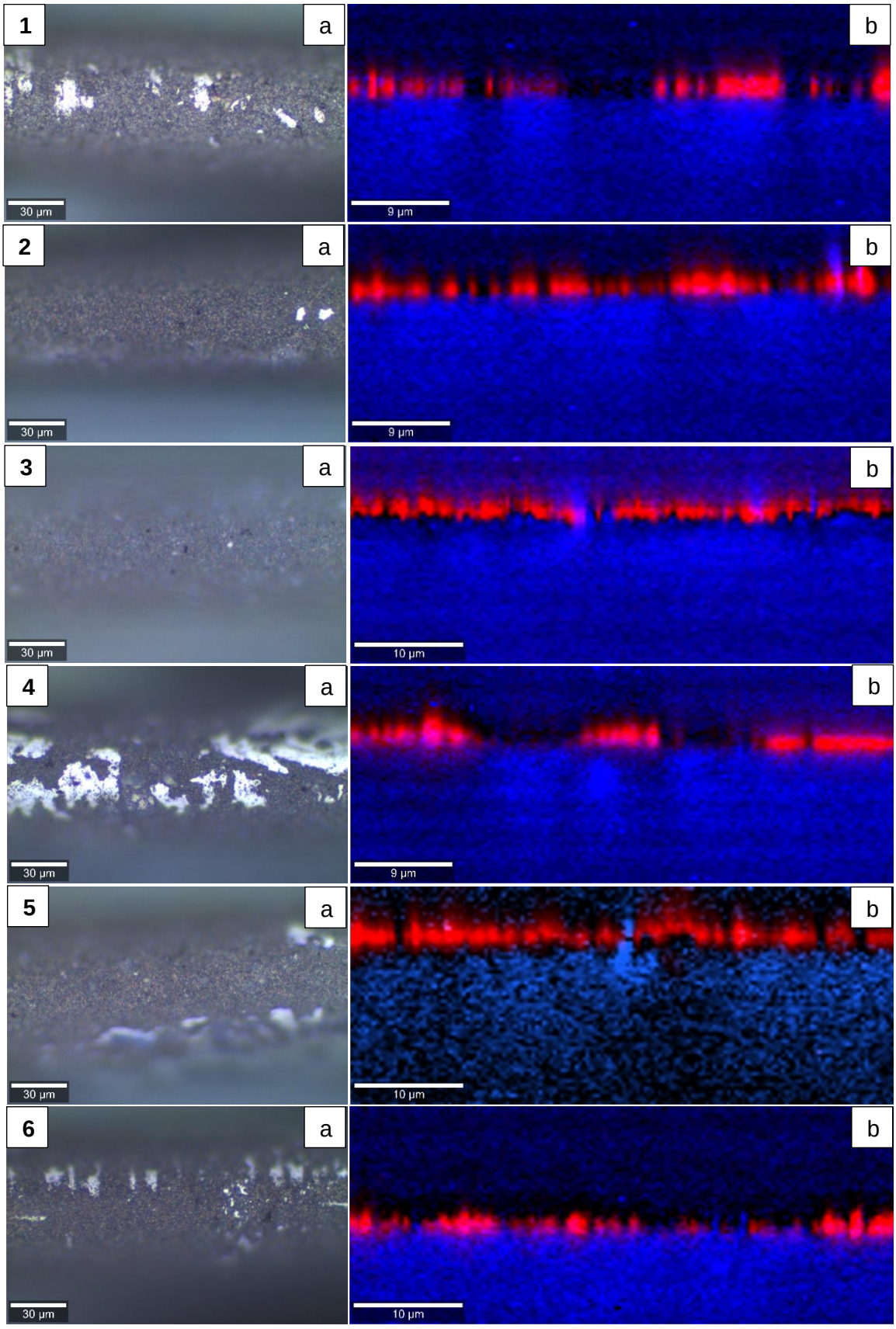

Figure 11-2: (a) Sample maps, (b) Raman map of coated optical fibre surface showing anatase layer (red) on the fused silica optical fibre (blue). Sample collect at process conditions of 500°C and (1) 0.12, (2) 0.58, (3) 1.73, (4) 2.30, (5) 2.88, (6) 3.46 mm.s^{-1}

C.1. Appendix: SEM images for coating thickness and morphology

Sol-gel coating method : Effect of calcination temperature

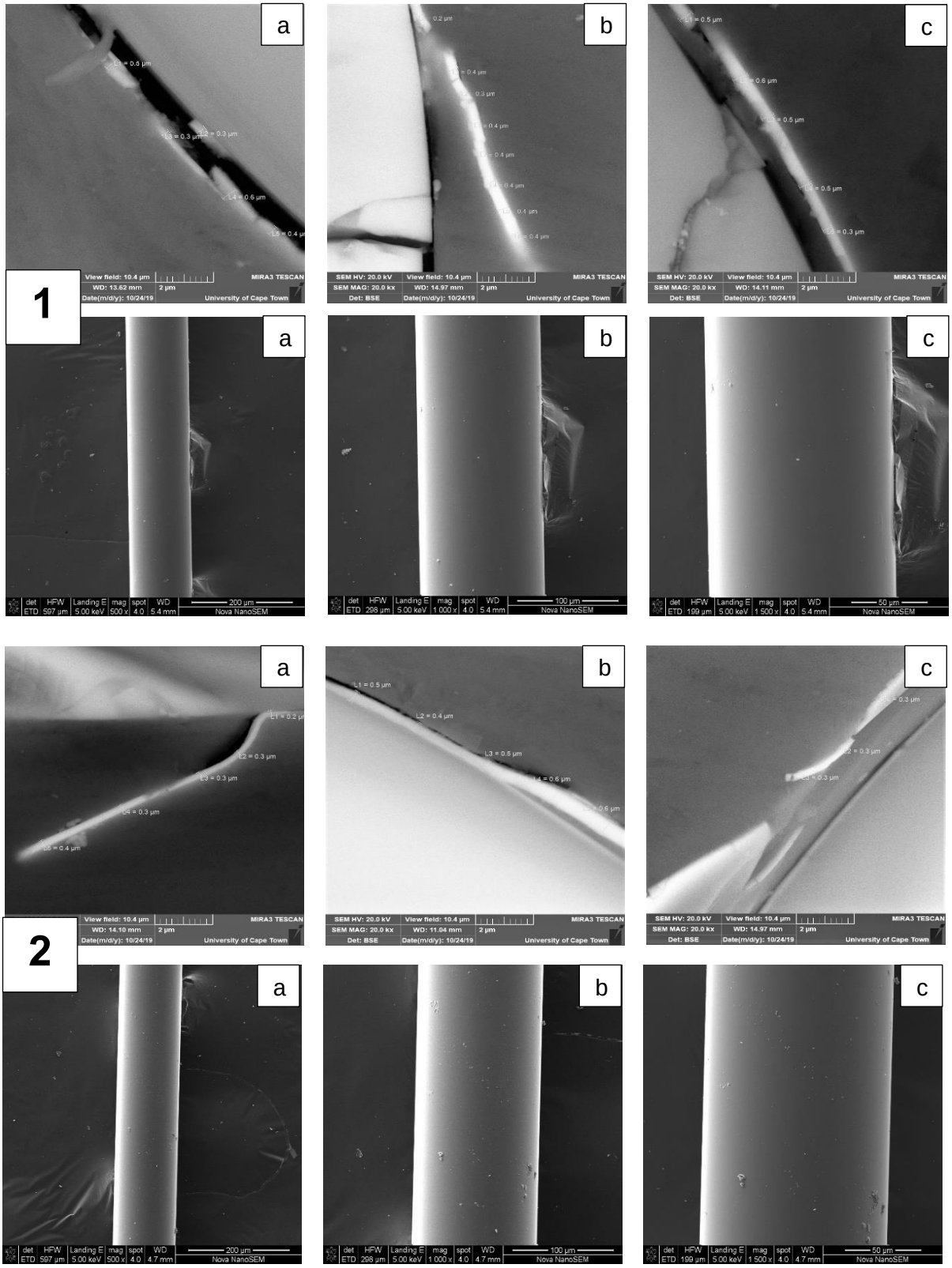

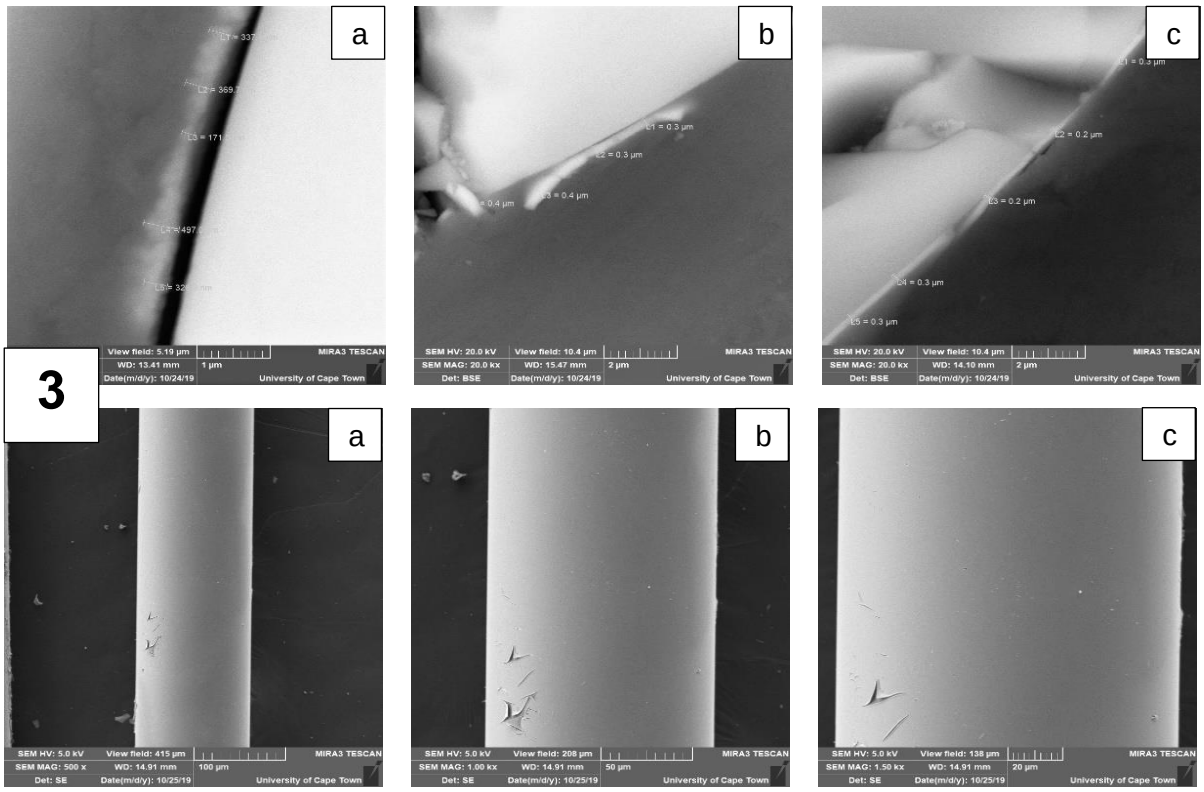

Figure 11-3: SEM images of coated optical fibre showing surface coating thickness measurements and surface morphology for each experiment performed in triplicate (a) Run 1, (b) Run 2 and (c) Run 3 for process conditions (1) 400°C, (2) 500°C and (3) 600°C at a constant speed of 1.15 mm.s^{-1}

Sol-gel coating method : Effect of pulling speed

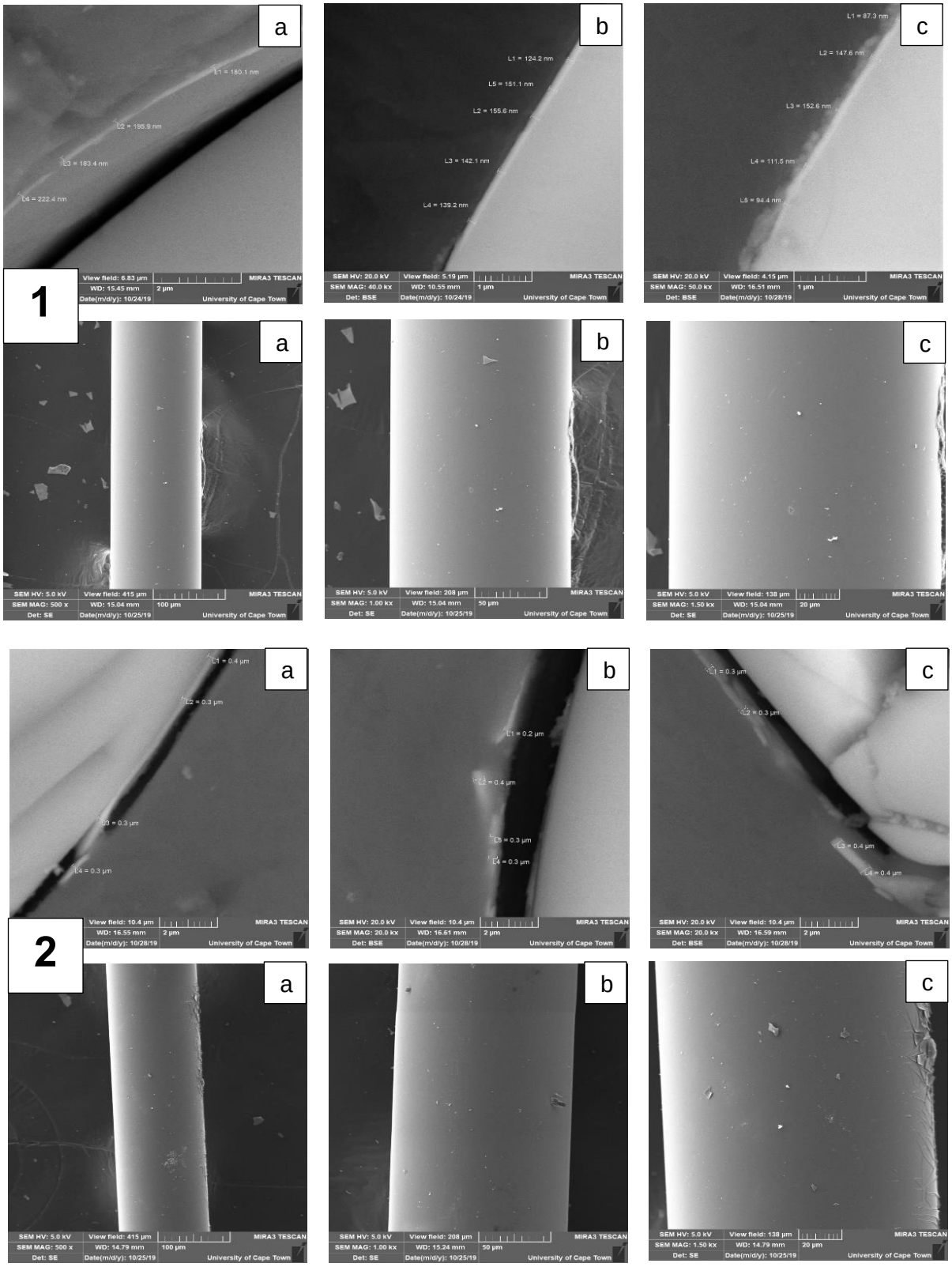

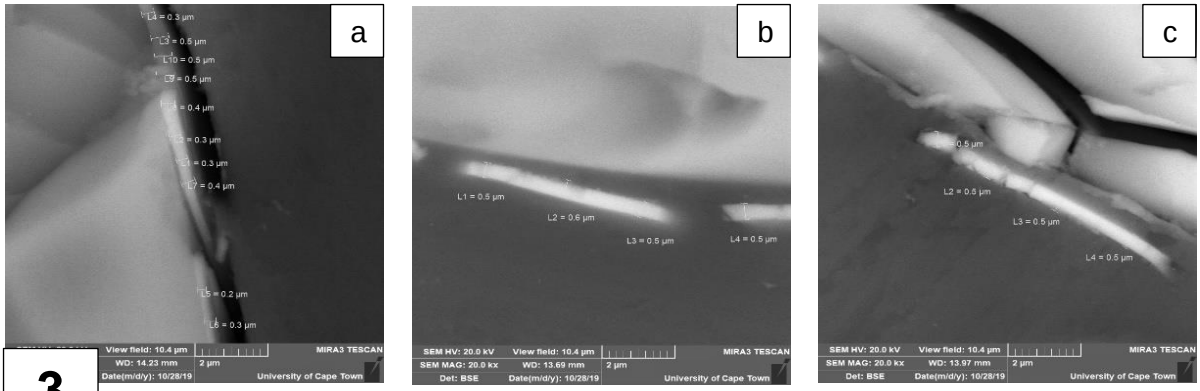
a
b
c
L1 = 0.5 µm
L2 = 0.6 µm
L3 = 0.5 µm
L4 = 0.5 µm
L5 = 0.2 µm
L6 = 0.3 µm
SEM HV: 20.0 kV
View field: 10.4 µm
MIRA3 TESCAN
University of Cape Town

3

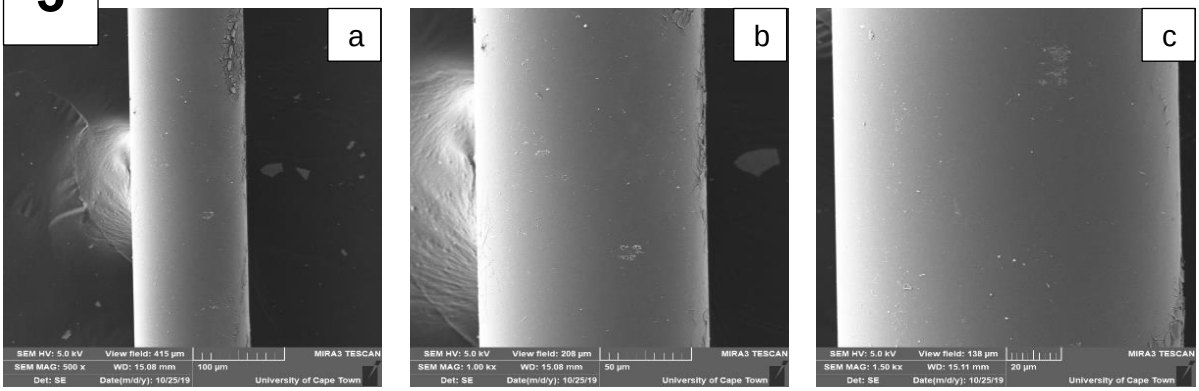
a
b
c
SEM HV: 5.0 kV
MIRA3 TESCAN
University of Cape Town

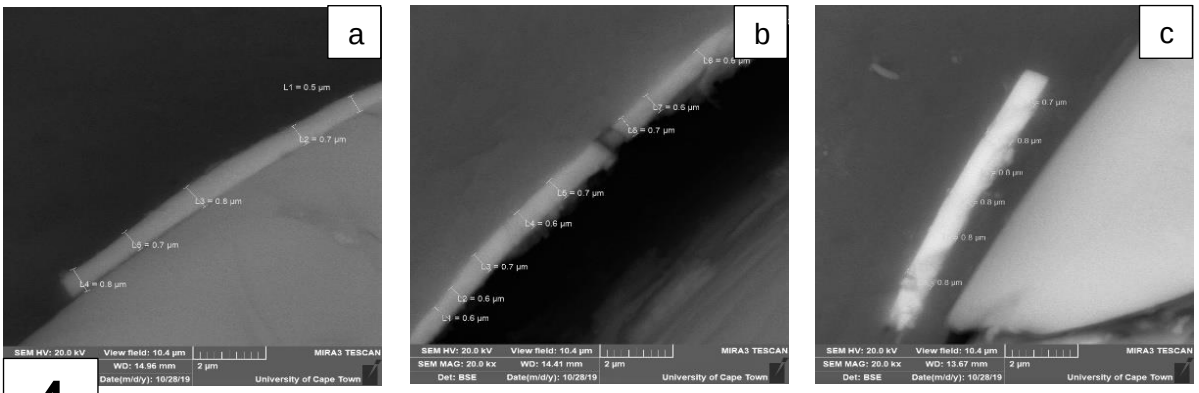
a
b
c
L1 = 0.5 µm
L2 = 0.7 µm
L3 = 0.8 µm
L4 = 0.6 µm
L5 = 0.7 µm
L6 = 0.7 µm
L7 = 0.6 µm
L8 = 0.7 µm
L9 = 0.8 µm
SEM HV: 20.0 kV
MIRA3 TESCAN
University of Cape Town

4

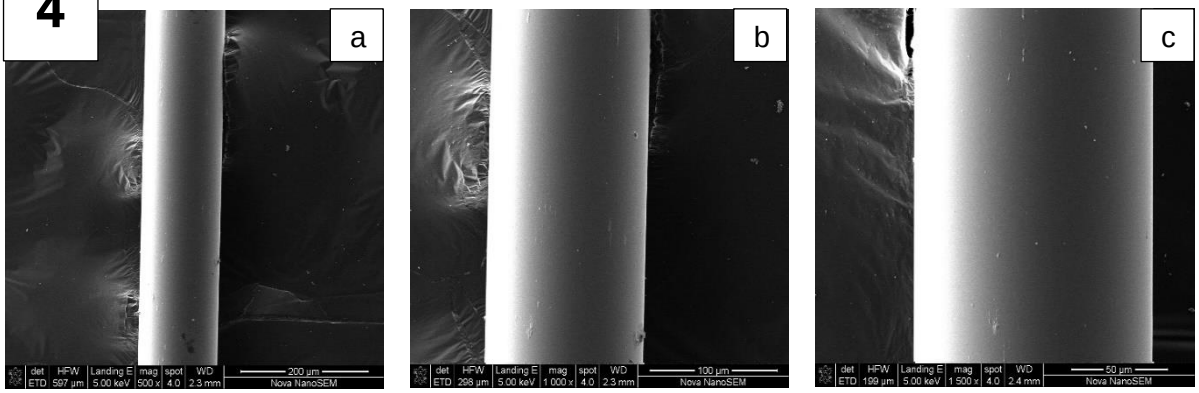
a
b
c
Nova NanoSEM

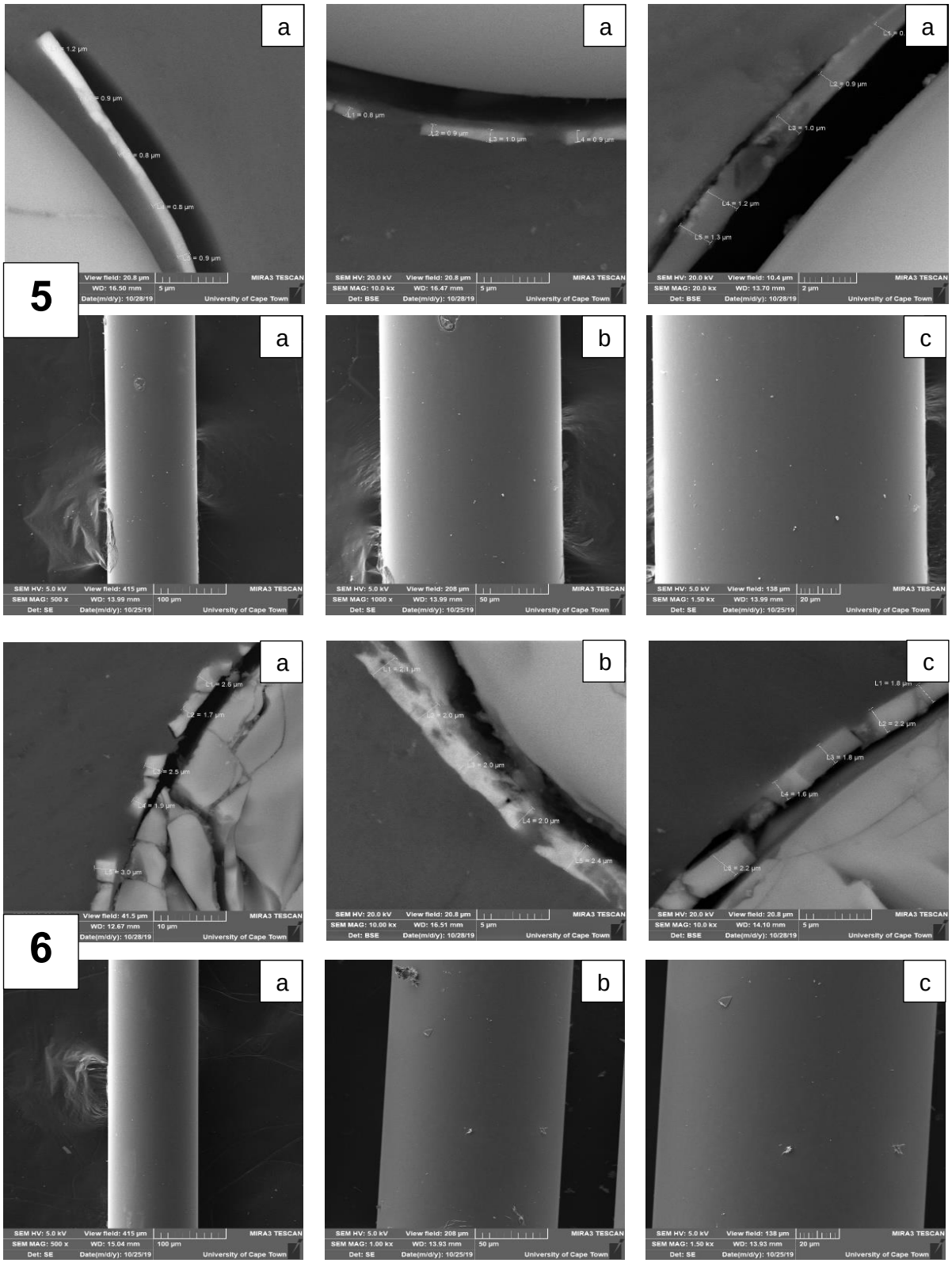

Figure 11-4: SEM images of coated optical fibre showing surface coating thickness measurements and surface morphology for each experiment performed in triplicate (a) Run 1, (b) Run 2 and (c) Run 3 for process conditions (1) 0.12 mm.s^{-1} , (2) 0.58 mm.s^{-1} and (3) 1.73 mm.s^{-1} , (4) 2.30 mm.s^{-1} , (5) 2.88 mm.s^{-1} and (6) 3.46 mm.s^{-1} at a constant calcination temperature of 500°C

P25 slurry coating method : Effect of drying temperature

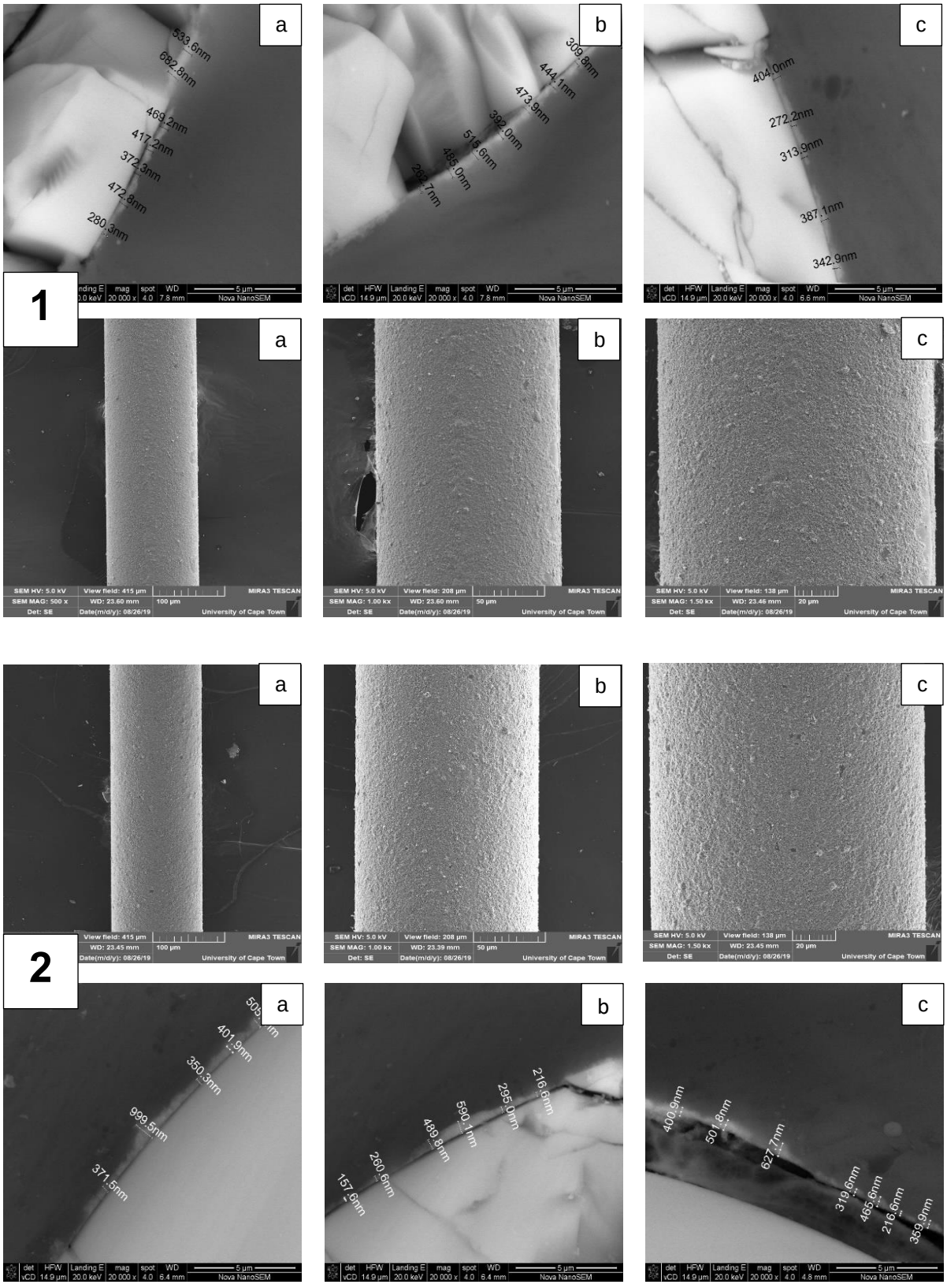

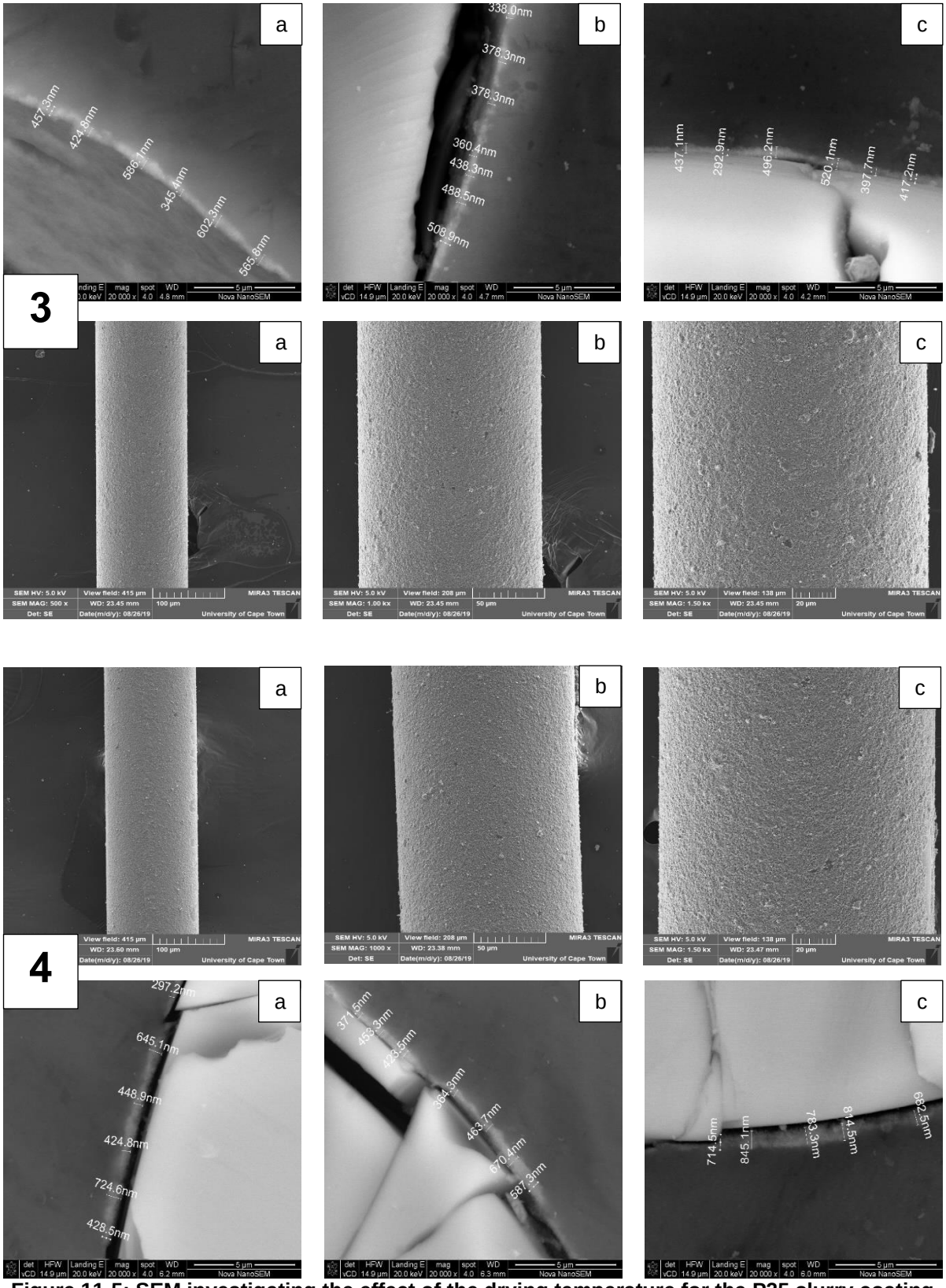

Figure 11-5: SEM investigating the effect of the drying temperature for the P25 slurry coating method. Images showing coating thickness and surface morphology for experiments performed in triplicate (a) run 1 , (b) run 2 and (c) run 3. The temperatures investigated were (1) 200°C, (2) 300°C, (3) 400°C and (4) 500°C at a standard process variable of 1.15 mm.s^{-1} , 5 wt.-% and pH of 4.65

P25 slurry coating method : Effect of pulling speed

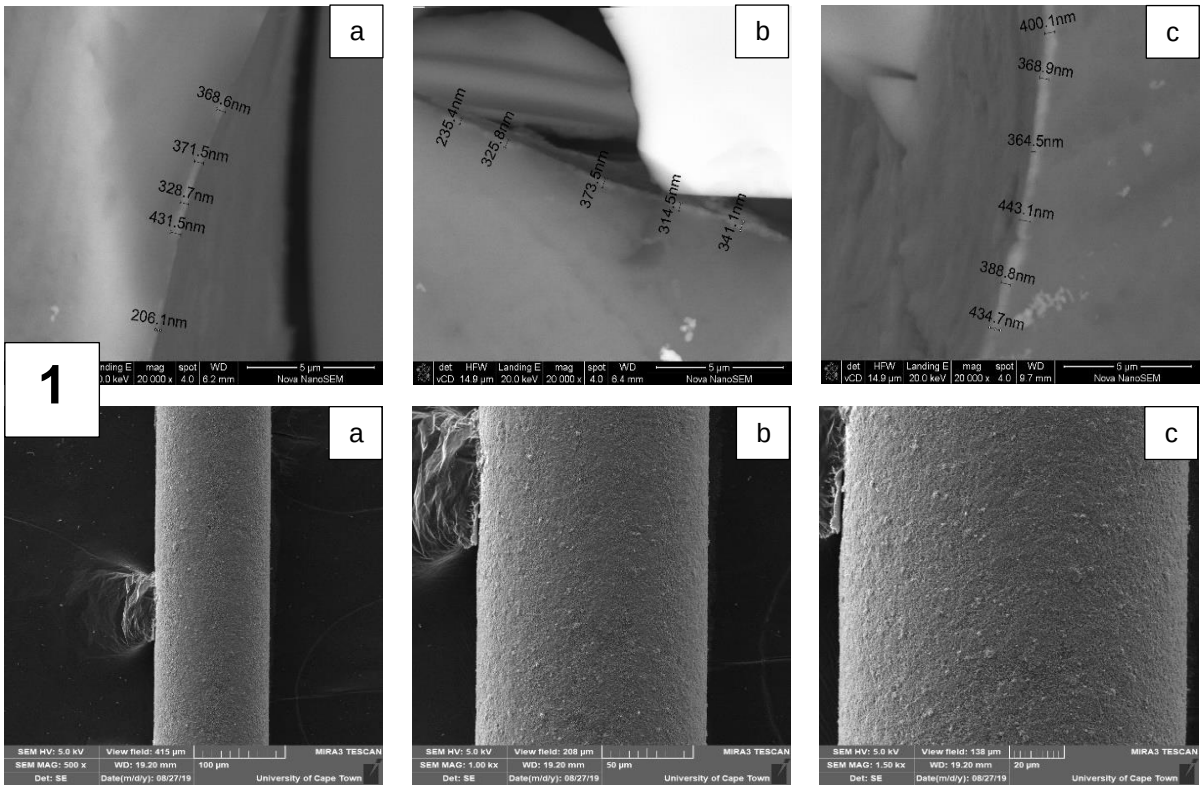

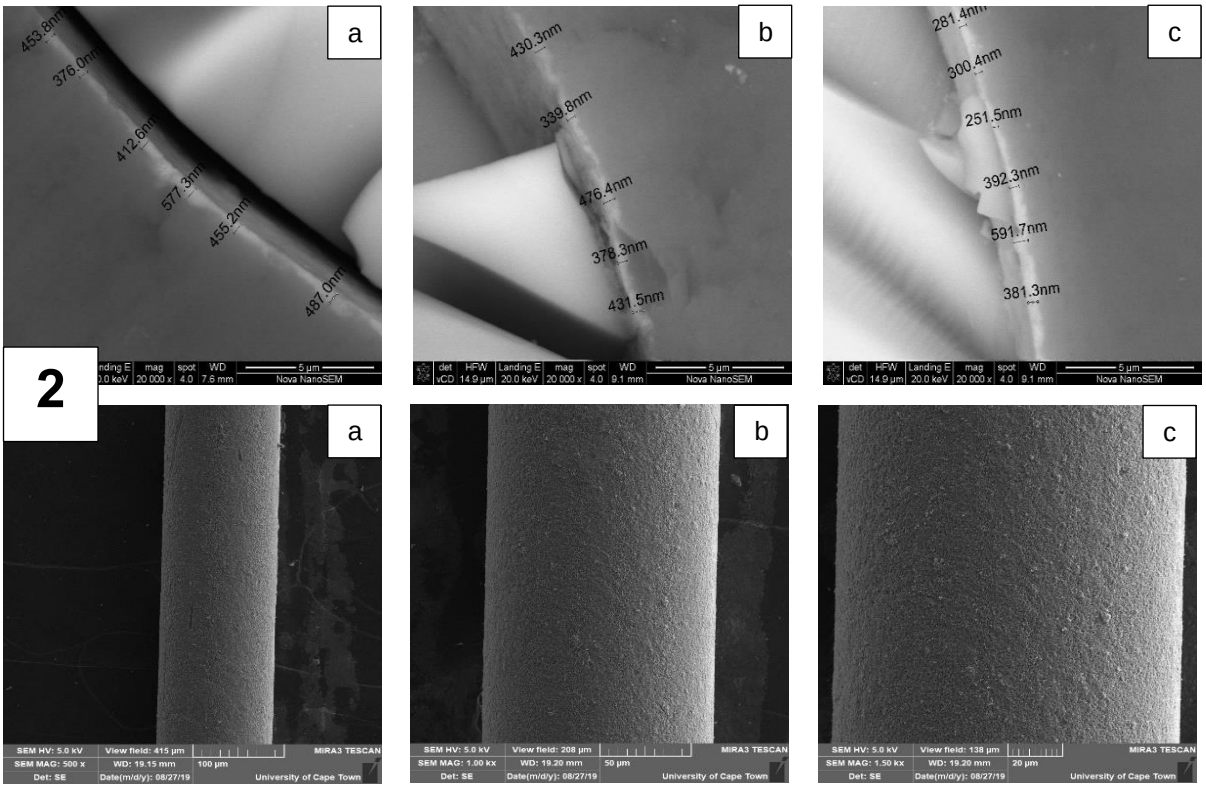
2
a
453.8nm
376.0nm
412.6nm
577.3nm
455.2nm
487.0nm
b
430.3nm
339.8nm
476.4nm
378.3nm
431.5nm
c
281.4nm
300.4nm
251.5nm
392.3nm
591.7nm
381.3nm
Nova NanoSEM
MIRA3 TESCAN
University of Cape Town

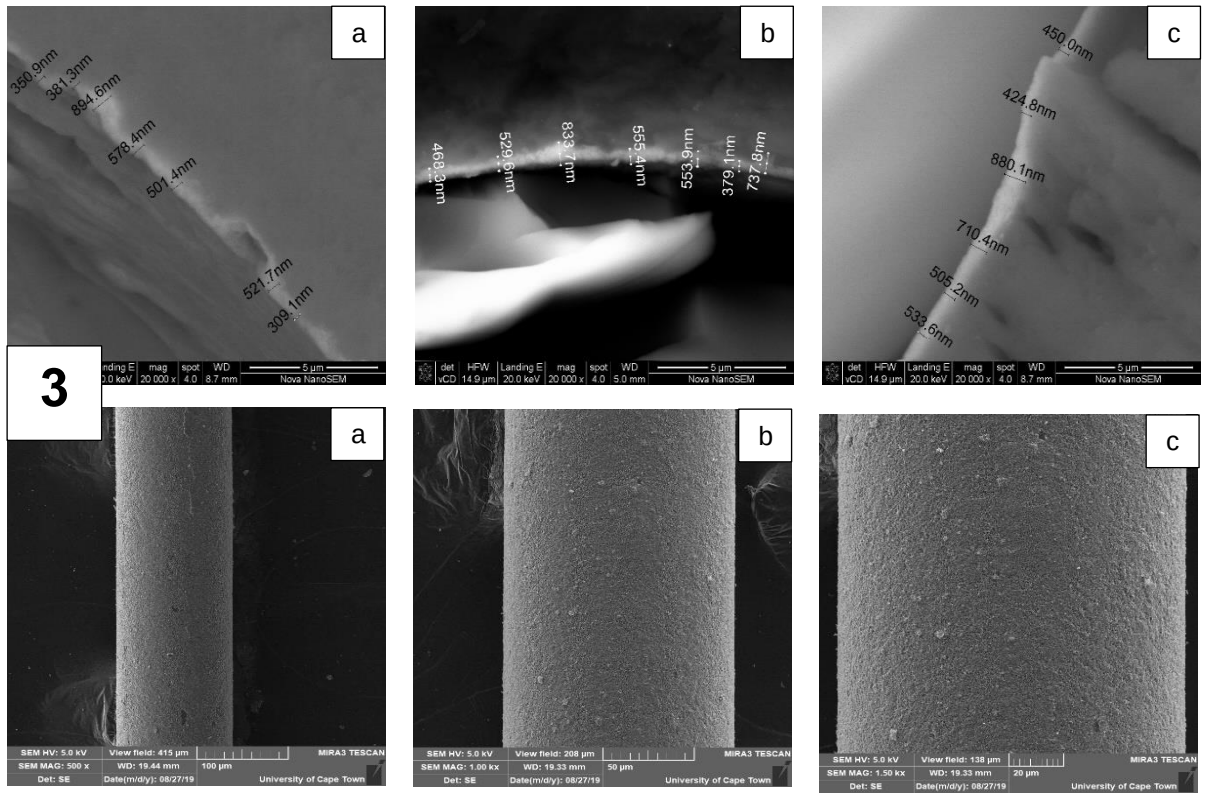
3
a
350.9nm
381.3nm
894.6nm
578.4nm
501.4nm
521.7nm
309.1nm
b
469.3nm
529.9nm
833.7nm
555.4nm
553.9nm
379.1nm
737.8nm
c
450.0nm
424.8nm
880.1nm
710.4nm
505.2nm
533.6nm
Nova NanoSEM
MIRA3 TESCAN
University of Cape Town

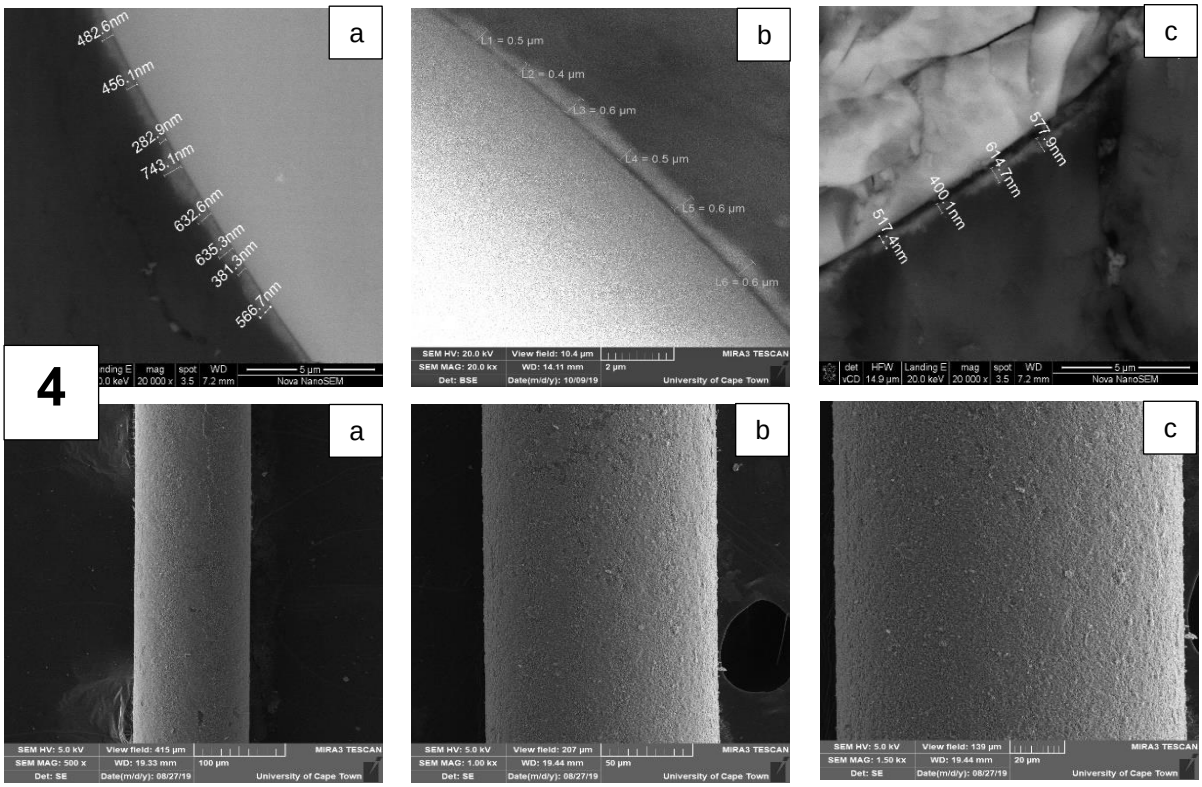
a
482.6nm
456.1nm
282.9nm
743.1nm
632.6nm
635.3nm
381.3nm
566.7nm
5 µm
Nova NanoSEM
b
L1 = 0.5 µm
L2 = 0.4 µm
L3 = 0.6 µm
L4 = 0.5 µm
L5 = 0.6 µm
L6 = 0.6 µm
SEM HV: 20.0 kV
View field: 10.4 µm
MIRA3 TESCAN
SEM MAG: 20.0 kx
WD: 14.11 mm
2 µm
Det: BSE
Date(m/d/y): 10/09/19
University of Cape Town
c
577.9nm
614.7nm
400.1nm
517.4nm
5 µm
Nova NanoSEM
4
a
SEM HV: 5.0 kV
View field: 415 µm
MIRA3 TESCAN
SEM MAG: 500 x
WD: 19.33 mm
100 µm
Det: SE
Date(m/d/y): 08/27/19
University of Cape Town
b
SEM HV: 5.0 kV
View field: 207 µm
MIRA3 TESCAN
SEM MAG: 1.00 kx
WD: 19.44 mm
50 µm
Det: SE
Date(m/d/y): 08/27/19
University of Cape Town
c
SEM HV: 5.0 kV
View field: 139 µm
MIRA3 TESCAN
SEM MAG: 1.50 kx
WD: 19.44 mm
20 µm
Det: SE
Date(m/d/y): 08/27/19
University of Cape Town

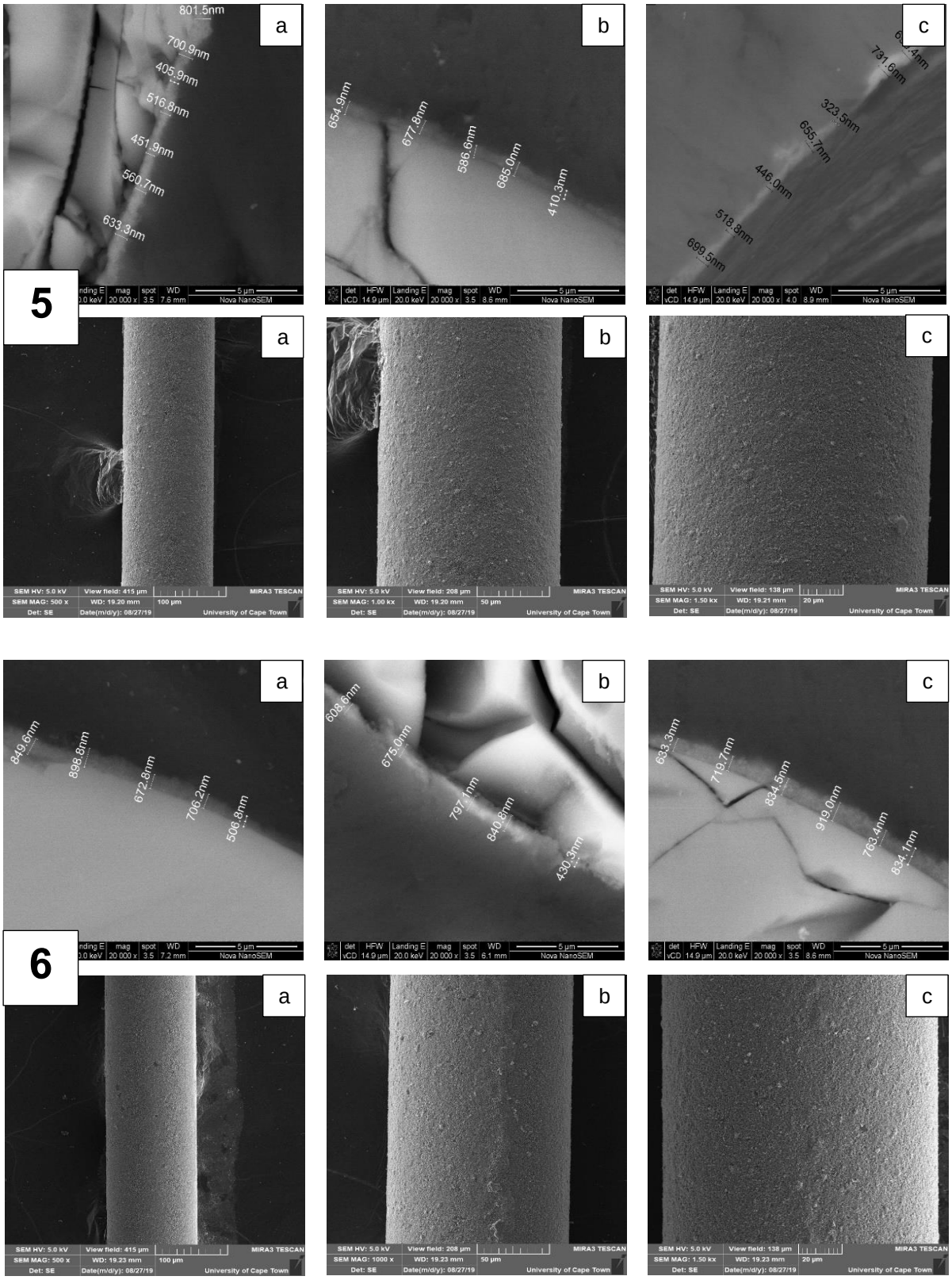

Figure 11-6: SEM investigating the effect of pulling speed for the P25 slurry coating method. Images showing coating thickness and surface morphology for experiments performed in triplicate (a) run 1 , (b) run 2 and (c) run 3. The pulling speeds that were investigated are; (1) 0.12 mm.s^{-1} , (2) 0.58 mm.s^{-1} and (3) 1.73 mm.s^{-1} , (4) 2.30 mm.s^{-1} , (5) 2.88 mm.s^{-1} and (6) 3.46 mm.s^{-1} at a standard process variable of 500°C , 5 wt.-% and pH of 4.65

P25 slurry coating method : Effect of P25 slurry concentration

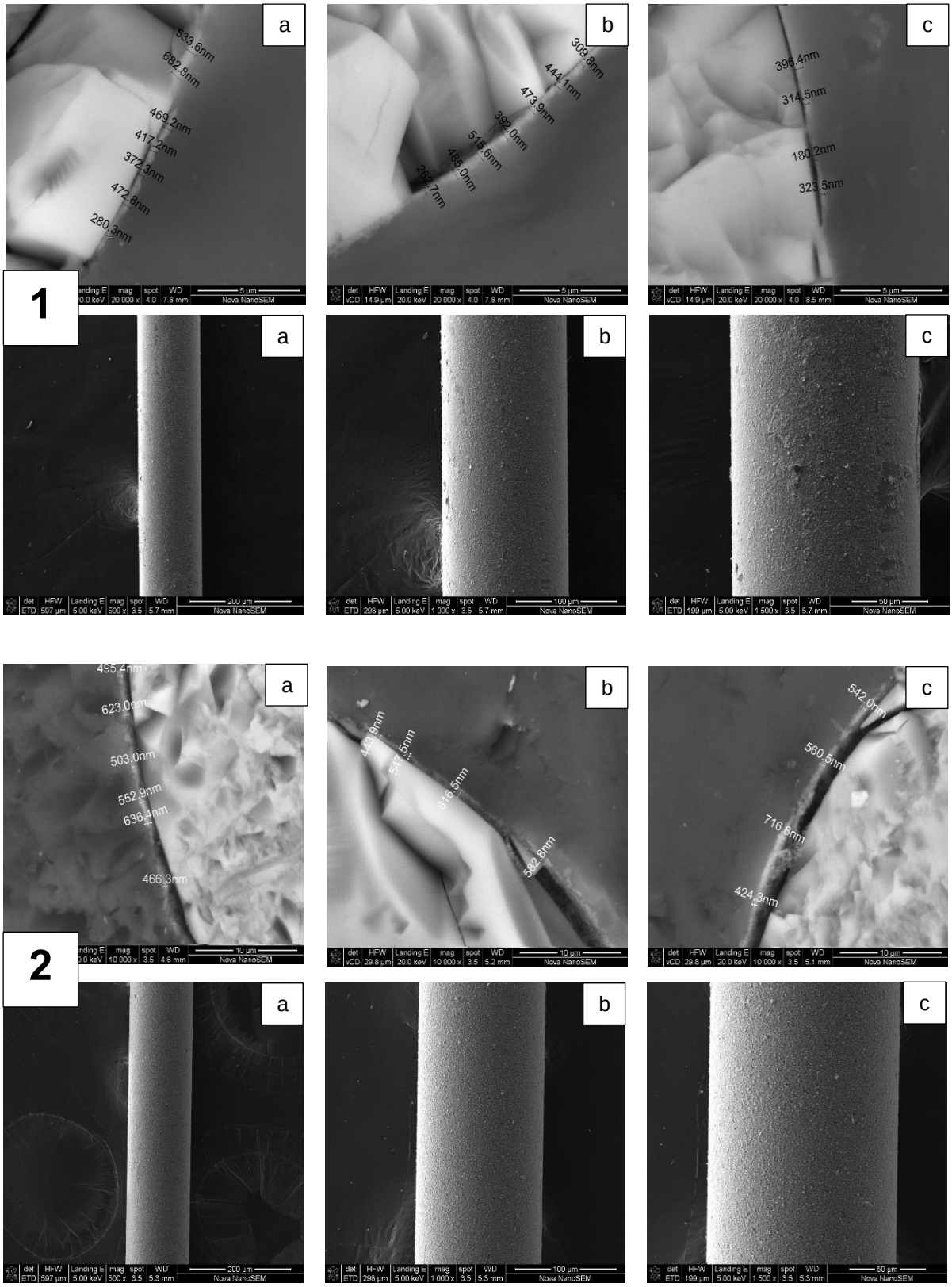

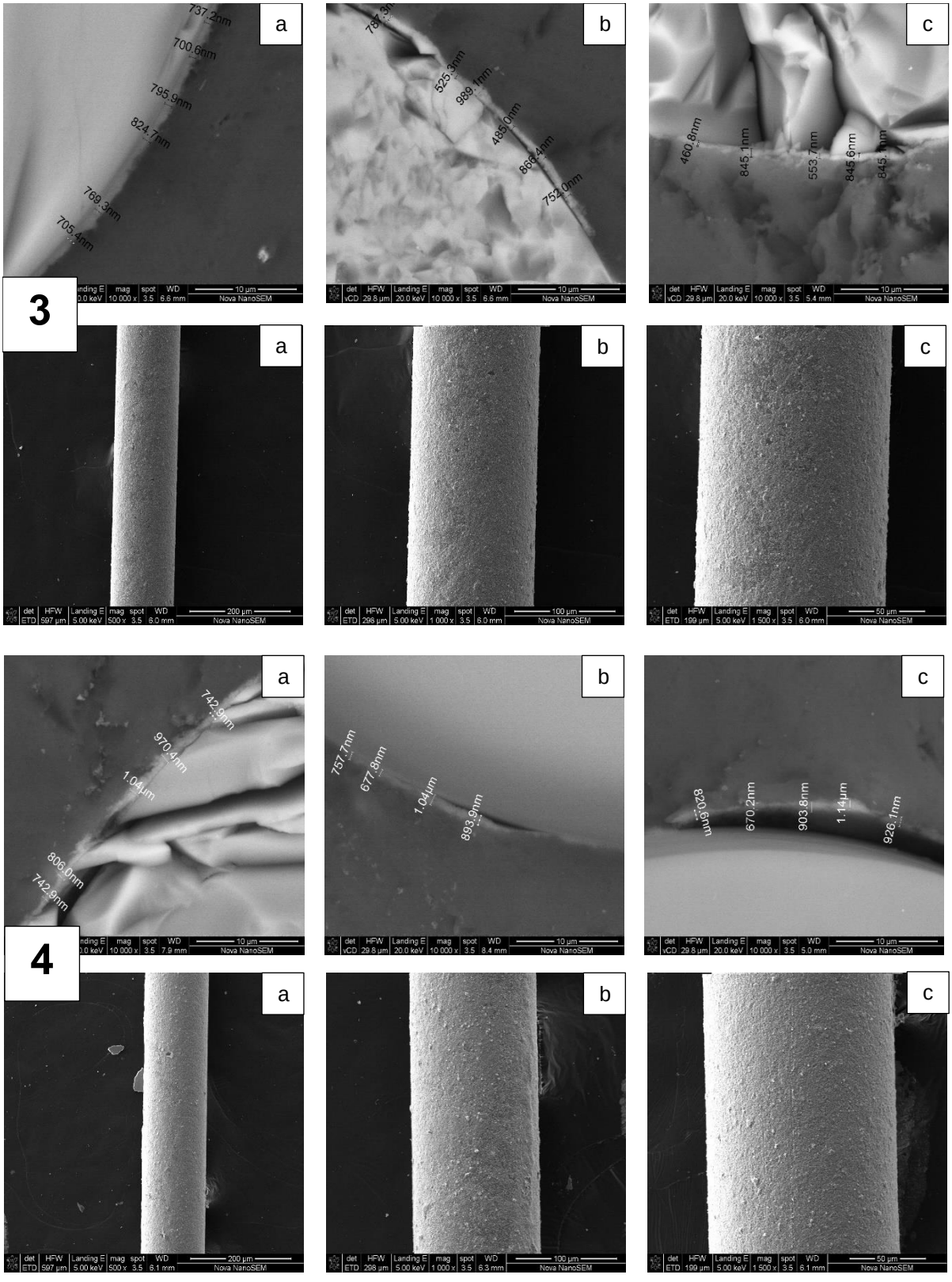

Figure 11-7: SEM investigating the effect of concentration for the P25 slurry coating method. Images showing coating thickness and surface morphology for experiments performed in triplicate (a) run 1 , (b) run 2 and (c) run 3. The concentrations that were investigated are; (1) 1 wt.-% , (2) 10 wt.-% and (3) 15 wt.-% , (4) 20 wt.-% at a standard process variable of 500°C , 1.15mm.s^{-1} and pH of 4.65

P25 slurry coating method : Effect of pulling speed

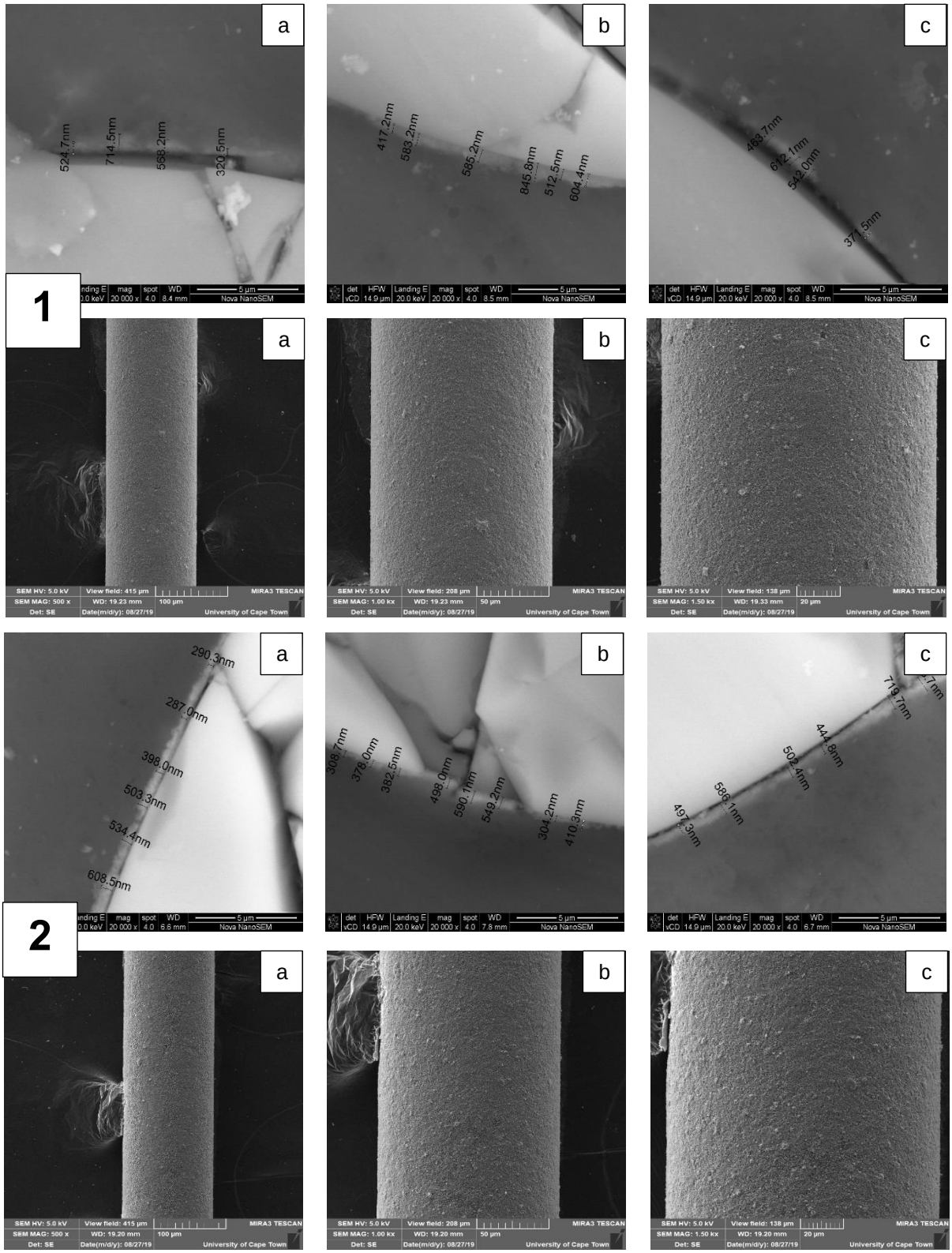

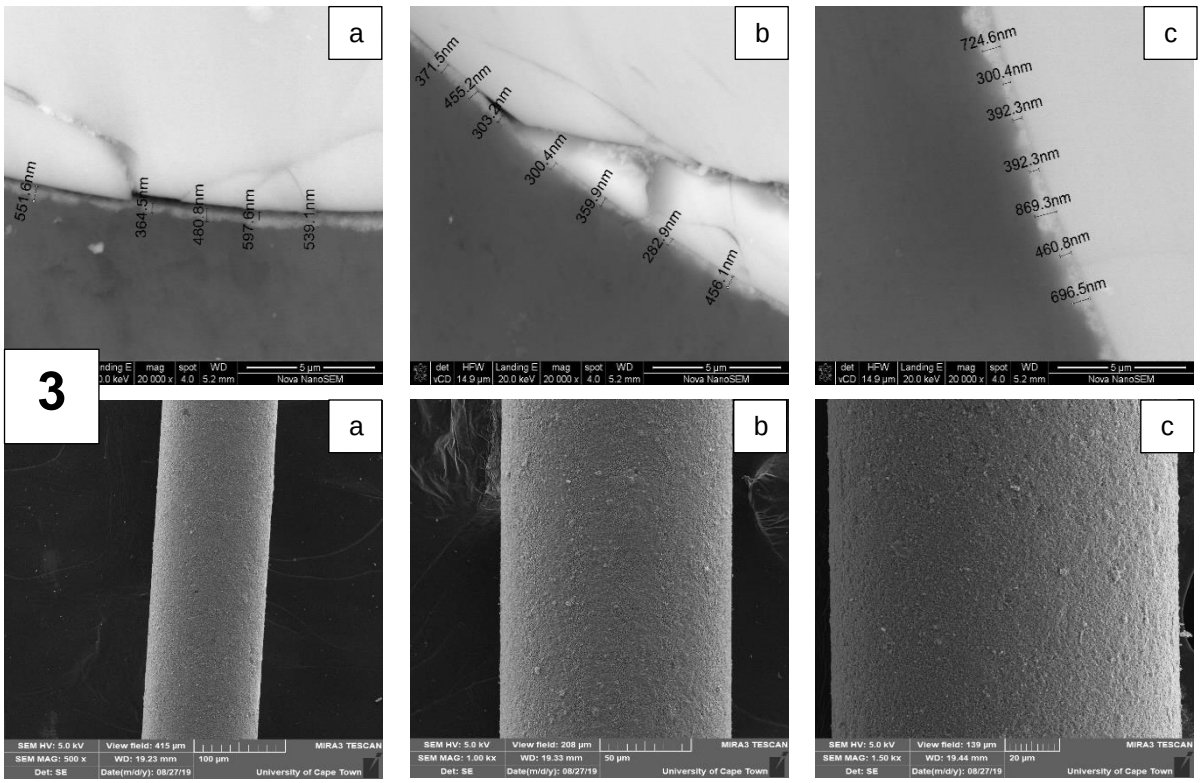

Figure 11-8: SEM investigating the effect of slurry pH for the P25 slurry coating method. Images showing coating thickness and surface morphology for experiments performed in triplicate (a) run 1 , (b) run 2 and (c) run 3. The results show; (1) 2.65 , (2) 3.65 and (3) 5.65 at a standard process variable of 500°C , 1.15mm.s^{-1} and 5 wt.-%

D.1. Appendix: Arduino speed control code

/* Written by Ameen Jakoet

* for Naomi Harrisankar

* MSc Chemical Engineering 2018

* Purpose: To send PWM signals to a Stepper Motor Controller DRV8825 to drive at desired speed

* This is run in conjunction with a Processing sketch which gives a GUI to control the speed, allow start and stop operations

* through Serial - Baud Rate: 9600, COM port: will change on different PCs (Currently COM3)

* Board & Processor: Arduino Mega2560

*/

```
double rpm= 2.0 ;
int onOrOff = 1 ; // ON = 1; OFF = 0



// ********************************
//   DO NOT CHANGE VALUES BELOW
// ********************************
int enab = 8;     // pin to ENABLE/DISABLE the motor controller
int drive = 9;    // pin to send PWM to drive motor
int direct = 10;  // pin to establish direction on DRV8825

int m1 = 2; // Mode pins 1-3
int m2 = 3; // These are used to establish Mostepping
int m3 = 4; // We're using 1,1,1 - 1/32 microsteps

double motorAngle = 1.8;     // degrees per step
double stepsPerRotation = (360.00 / motorAngle) /0.03125;
double mpr = 60.0000;        // minutes per rev in seconds
double dcr = 2;          // Duty Cycle Ratio

double stepTime    =mpr / (rpm * stepsPerRotation) * 1E6 / dcr;

// This conversion includes all the conversions "simplified":
// -rpm->Hz conversion for 200-steps stepper motor
// -conversion to microseconds for precise speed
// -inverted for period calculation (mpr)

void setup() {
  pinMode (enab, OUTPUT);
  pinMode (drive, OUTPUT);
  pinMode (direct, OUTPUT);
```

```
  pinMode (m1, OUTPUT);
  pinMode (m2, OUTPUT);
  pinMode (m3, OUTPUT);
  if (onOrOff == 1){
    digitalWrite (enab, LOW);       //Switch ON
  }
  else if (onOrOff == 0) {
    digitalWrite (enab, HIGH);      //Switch OFF
  }
  digitalWrite (m1, HIGH); //1,1,1 gives us 1/32 microsteps
  digitalWrite (m2, HIGH);
  digitalWrite (m3, HIGH);
}

void loop() {
  // Looking down the shaft this will cause:
     // digitalWrite (direct, HIGH); // CW rotation
      digitalWrite (direct, LOW); // CCW rotation

      // causes step at period 'stepTime' based on frequency from input rpm
      digitalWrite (drive, HIGH);
      delayMicroseconds (stepTime);
      digitalWrite (drive, LOW);
      delayMicroseconds (stepTime);
}
```

E.1. Appendix: Chemical Safety

Table 11-8: Summary of chemicals used in project and the hazards and MSDS links

Chemical Name	Hazards	URL
Acetone (99.9%)	• Highly flammable liquid and vapour • May cause drowsiness a dizziness	https://www.labchem.com/tools/msds/msds/LC10420.pdf
Sodium hydroxide (0.5M)	• Causes severe skin burns and eye damage	http://www.labchem.com/tools/msds/msds/LC24350.pdf
Titanium butoxide	• Corrosive, flammable liquid • Irritant	https://www.pfaltzandbauer.com/MSDS/T02315%20%20SDS%20%20031017.pdf
Acetic acid	• Flammable liquid and vapour • Causes severe skin burns and eye damage	http://www.labchem.com/tools/msds/msds/LC10100.pdf
Ammonium acetate	• Causes skin irritation • Causes serious eye irritation	http://www.labchem.com/tools/msds/msds/LC10960.pdf
P25 Titania	• May cause irritation upon inhalation	https://ehslegacy.unr.edu/msdsfiles/22541.pdf